Albedo Enhancement via Brightening of Stratocumulus Clouds as Climate Engineering Method

Zur Erlangung des akademischen Grades eines
DOKTORS DER NATURWISSENSCHAFTEN
von der Fakultät für Physik des
Karlsruher Instituts für Technologie (KIT)

genehmigte

DISSERTATION

von

Dipl.-Met. Tobias Schad
aus Ulm

Tag der mündlichen Prüfung:	07. Juli 2017
Referent:	Prof. Dr. Thomas Leisner
Korreferent:	Prof. Dr. Christoph Kottmeier

Abstract

Marine cloud brightening (MCB) is proposed among several climate engineering options to counteract or at least postpone global warming caused by anthropogenic activities. The idea of MCB is to release additional sea salt particles, which causes an increase in cloud droplet number concentration of marine low-level boundary clouds. As a consequence cloud albedo increases which is accompanied by a decreases in short-wave radiation. The interaction of aerosols and clouds is still one of the largest uncertainties in global climate models. As aerosol particles have an impact on cloud optical properties it is vital to describe this processes in a correct way. This includes subgrid scale clouds, because they influence radiation as well as grid scale clouds.

In this thesis, the online-coupled model system COSMO-ART is used to investigate the impacts due to MCB. Although COSMO-ART takes aerosol cloud interaction into account on grid scale, aerosol cloud interaction on subgrid scale is neglected prior to this work. Therefore COSMO-ART is extended to include aerosol-cloud-radiation interaction on subgrid scale.

The model results are compared to observations conducted during a field campaign in 2008 (VOCALS-REx). Cloud properties like effective radius of cloud droplets and cloud droplet number concentration are well captured by the model. Comparison to radiation measurements at surface show how import it is to include subgrid scale aerosol-cloud-radiation interaction, as the model result improves by taking it into account.

Climate engineering scenarios with different sized seeding particles reveal the importance of the right size of the seeding particles. Seeding with smaller particles increase cloud droplet number concentration while seeding with larger particles slightly decrease cloud droplet number concentration. The susceptibility of cloud droplet number concentration to seeding with sea salt particles reveal that the efficiency of MCB is decreased in presence of large amounts of

anthropogenic aerosols, as both compete in the formation to cloud droplets.

Furthermore the climate engineering simulations reveal that the direct effect of the sea salt particles becomes important if the mass of sea salt is increased drastically. This can be shown in case of the seeding scenario with larger seeding particles. Although short-wave radiation is decreased in case of seeding with larger particles long-wave downward radiation is on the other increased and therefore limiting the efficiency of MCB. Because of that the direct effect of the seeded sea salt particles should not be neglected.

Furthermore it is shown that by neglecting subgrid-scale aerosol-cloud-radiation interaction the impact on radiation by aerosols is underestimated. A climate engineering simulation without taking subgrid-scale aerosol-cloud-radiation interaction into account underestimates the impact of MCB by 20 %.

Contents

1 Introduction

Years ago at the Solfatara, which is a shallow volcanic crater and a part of the Campei Flegrei at Pozzuoli near Naples, the tourist guide showed the visitors a little experiment. He stood in front of a rock with a little opening, where along with volcanic gases water vapour was released. Wondering at first glance why the guide carried a newspaper with him he then ignited the newspaper and holding it in front of the opening. What was only vaguely visible before became now clearly visible. Small clouds evolved from the opening and it was not the smoke of the newspaper, but small water droplets forming clouds.

This striking effect in Pozzuoli seems to be a nice show for tourists, but the same effect becomes on global scale an idea to counteract or at least postpone global warming caused by anthropogenic activities. The counteraction is called climate engineering (also often named geo-engineering or geoengineering) and is defined as "the deliberate large-scale intervention in Earth's climate system, in order to moderate global warming" (Shepherd, 2009). This involves several techniques to intervene with the climate system, where some would take place in space while others would be conducted direct on Earth. It is distinguished between two major groups of techniques. First group is targeting the radiation budget of earth, therefore often called solar radiation management (SRM). The main goal is to enhance planetary albedo to reflect more incoming solar radiation. The approaches reach from mirrors in space, to stratospheric aerosols, brightening of clouds, brightening of housings, changing oceans albedo by white floating devices, or deploying reflectors in desert areas (Feichter and Leisner, 2009). The second approach targets to remove carbon dioxide (CO_2) from Earth's atmosphere or to prevent reaching it, why it is called carbon dioxide removal (CDR). This includes sequestration and storage of CO_2 (Herzog and Golomb, 2004). For example there could be methods on basis of biochar and biomass, where carbon is stored in plants itself or in the product of them. It is thought

about other methods like marine ones to enhance the ocean CO_2 sinks (Lampitt et al., 2008). Or to increase the weathering which naturally removes CO_2 from atmosphere (Schuiling and Krijgsman, 2006).

Within this work the technique of marine cloud brightening is investigated to enhance the planetary albedo. The idea is to utilize the influence of aerosols on clouds. It is known that clouds on Earth only form in the presence of aerosol particles which serve as cloud condensation nuclei (CCN) (Aitken, 1881; Pruppacher and Klett, 1997). Aerosols govern the microphysical evolution of clouds and therefore both are from interest because they impact the hydrological cycle. Aitken (1881) found that formation of cloud droplets not only depend on aerosols, but also on their chemical composition. Additionally he found that natural salts and particles from burning sulfur (like from fossil fuel) are very efficient CCN, and therefore hypothesized that cloud properties are influenced by anthropogenic activities. It was Köhler (1936a) who formulated the theoretical basis of cloud droplet formation (also called activation of aerosol particles) depending on the size and chemical composition of hygroscopic aerosols. Wegener (1911) hypothesized that solid particles, serving as ice nuclei due to their surface structures, are promoting the formation of ice crystals. Next Wegener (1911), Bergeron (1935), and Findeisen (1938) hypothesized that precipitation is produced in a cloud by the efficient growth of ice particles due to deposition at the expense of cloud droplets due to the difference of saturation water vapour pressure of ice and water. On this findings experiments where conducted with seeding clouds by artificial introduced ice nuclei (i.e. silver iodide) released from airplanes (Kraus and Squires, 1947). Although this cannot be related to climate engineering this is one of the first scientific documented experiments where cloud properties were deliberately changed.

As measured data showed great variance of cloud droplet number concentration in cumulus clouds, Twomey and Squires (1959) related this to the variance of available CCN population as cloud droplet number concentrations were higher over continent than over ocean. They concluded that over continent the cloud droplet concentration is higher because CCN are more abundant over land than over ocean. Additionally they found that the higher droplet concentration is accompanied by a smaller size of the cloud

droplets compared to maritime environments. They also followed that precipitation in ice-free clouds is therefore less efficient over continent and depending on the amount of available aerosols.

As the size of the available CCN is a vital property in cloud formation Squires (1958) formulated that the low amount of cloud droplet concentration in maritime environments is caused by giant sea salt particles. They inhibit the activation of smaller particles to cloud droplets by lowering the maximum water vapour pressure reached during cloud formation. Twomey (1959) formulated this competition of aerosol particles for water vapour and its impact on maximum water vapour reached during cloud formation for an isolated rising air parcel.

Due to the increase of anthropogenic activities for example by burning fossil fuels the amount of aerosols increased. As it was clear that aerosols and clouds are coupled tightly together it was again Twomey (1977) who linked aerosols to cloud optical properties. He pointed out that an increase in aerosol number concentrations would lead to an increase in cloud optical thickness, which means a higher cloud albedo. On large-scale this would lead to an increase of planetary albedo and therefore it would have a cooling effect on climate.

Aside from the change of cloud optical properties Albrecht (1989) postulated that an increase of aerosols would lead in ice-free low-level clouds over ocean to a change of precipitation processes and therefore it would also affect low-level cloudiness. The increase of aerosols would lead to a decrease in drizzle rates which would increase liquid water content of shallow clouds. Therefore an increase in aerosols would affect the lifetime of low-level clouds. On long-term this would have a cooling effect on climate.

With the findings of Twomey (1977) and Albrecht (1989) the idea of cloud seeding as a method of climate-engineering was born. Latham et al. (2008) postulated that it would be possible to counteract the warming due to a doubling of CO_2. But as cloud cover is changed also the terrestrial radiation budget is changed and therefore the net effect on climate is much more complicated to be estimated. However, as estimated by Charlson et al. (1992), there is a net cooling effect caused by the increased global aerosol concentration and its impact on cloud optical and microphysical properties. This cooling is assumed to be in the same order of the heating caused by greenhouse gases like CO_2.

It was found that an increase of global cloudiness by 4% (Randall and Coakley, 1984) or an increase of global cloud albedo by 0.06 (Latham et al., 2008) of marine stratocumulus clouds could offset global warming caused by a doubling of CO_2. Simulations with global circulation models (GCMs) showed that there are four major regions which are quite susceptible to changes in aerosol amount. All have persistent marine stratocumulus clouds in common. Although experiments to quantify the effect of marine cloud seeding are only written on paper (Latham et al., 2012) and large-scale deployment is technically not possible at the moment, numerical models can be used to evaluate the impact of seeding.

This deliberate seeding of low-level marine stratocumulus clouds is called marine cloud brightening (MCB). There are several studies of MCB (Jones et al., 2009; Korhonen et al., 2010; Alterskjær and Kristjánsson, 2013; Aswathy et al., 2014), but all of them are conducted with global climate models (GCMs). Due to the coarse resolution of GCMs several processes have to be parameterized including subgrid scale processes and aerosol cloud interactions. This is accompanied with several uncertainties. On the other hand large eddy simulations (LES) with a few meters of grid spacing can be conducted to investigate the effects of MCB (Maalick et al., 2014). But although they are capable of simulating all processes explicitly they are limited of their spatial domain. The simulated domain is only spanning few kilometres which includes only a single cloud or a cluster of clouds. Additionally LES studies often treat ideal case studies and do not consider real case scenarios.

To close the gap between GCM and LES the numerical regional model system COSMO-ART (Vogel et al., 2009) is used to investigate the effects of MCB. A regional model system gives the advantage to conduct simulations with higher resolution and a more explicit representation of processes which cannot be resolved by GCMs. Although regional model systems cannot resolve processes as explicit as an LES they have the advantage to simulate realistic scenarios.

Although grid resolution is higher in regional models compared to GCMs some processes are still not resolved and have to be parametrized. Of course this introduce some uncertainties, but neglecting those processes would lead to a major drawback and important interactions like aerosol cloud radiation interactions on subgrid scale would be missing. This is especially valid for

subgrid scale convective processes and subgrid scale cloud cover. The size of cloud structures could still be smaller than the grid size used in a regional model. Therefore it is necessary to parametrize the subgrid scale cloud processes, since they influence grid scale properties. As parametrizations are commonly only a simple approach to represent the subgrid scale processes it is accompanied by drawbacks. For example the convection scheme developed by Tiedtke (1989) contains only simple cloud microphysics and does not account for aerosol cloud interactions. Additionally the parametrization calculates a subgrid scale cloud cover, which impacts radiation balance of the model. Changes in subgrid scale cloud cover have an impact on the radiation budget. Alapaty et al. (2012) could show how important it is to take subgrid scale cloud cover from parametrized convective processes into account. Also non-convective and non-precipitating clouds may have to be parametrized in regional models, because grid size is still too large to resolve all cloud structures. Sundqvist et al. (1989) developed an approach for those types of clouds which is similarly used in COSMO.

Those schemes still neglect aerosol cloud interaction and therefore changes in aerosol concentrations have no influence on the subgrid scale parametrized clouds. This also impacts evaluation of marine cloud brightening since changes of optical properties due to seeding is not taken into account on the subgrid scale. This is a huge disadvantage and within this work a first approach is used to overcome this shortcoming.

Model results will be compared to measurements of a field experiment conducted in one of the most favourable regions for marine cloud brightening. This campaign (VOCALS-REx) took place in October and November 2008 (Wood et al., 2011) and the data was provided by NCAR/EOL under the sponsorship of the National Science Foundation [1].

Within this work the aim is to answer following questions:

- How are subgrid scale parametrizations affecting the result of investing aerosol cloud interaction (e.g. convection parametrization, non-precipitating subgrid scale clouds)?

[1] http://data.eol.ucar.edu/, VOCALS-Rex field catalogue: http://catalog.eol.ucar.edu/vocals/

- How large is the bias by excluding aerosol cloud interaction in subgrid scale cloudiness in case of comparison to observation and in case of climate-engineering?

- In which way are additional sea salt particles changing cloud properties?

- Is seeding efficiency lowered by anthropogenic aerosol or are there other limiting factors?

Chapter 2 gives a short introduction to the climate system, followed by chapter 3 and 4 where the basics of aerosols and aerosol cloud interaction are presented. Chapter 5 explains the technique of marine cloud brightening as a method of climate-engineering, while chapter 6 gives a summary of the model system COSMO-ART. The results of this work starts with chapter 7 where the deficits of the convection parametrization are summed up, followed by chapter 8 where model results are compared to observations from VOCALS-REx. Chapter 9 sums up the results of the climate-engineering simulations and chapter 10 gives the conclusion.

2 A Simple Conceptual Model of Ground Temperature

The amount of incoming solar radiation at the top of the atmosphere is about $S_0 = 1368$ Wm^{-2} (S_0 = solar constant). Due to the spherical shape of the earth, the temporal and spacial mean of solar radiation is about 342 Wm^{-2}. Solar radiation undergoes several processes as it passes through the atmosphere. Those processes influence the short-wave radiation which finally reaches earth surface. About 30 % of short-wave radiation is scattered and reflected back to space. The ratio of incoming $L\downarrow$ and outgoing short-wave radiation $L\uparrow$ is called planetary Albedo (A).

$$A = \frac{L\uparrow}{L\downarrow} \tag{2.1}$$

The remaining 70% of incoming short-wave radiation is absorbed by the earth-atmosphere-system where it is transformed to latent and sensible heat and eventually returned as long-wave radiation (equilibrium situation). Stratospheric Ozone (O_3) absorbs about two percent of short-wave radiation. Within troposphere 17 % are absorbed by aerosols and clouds and about 51 % of the radiation is absorbed by earth surface. The long-wave radiation flux directed from surface into the atmosphere is absorbed to a certain percentage α by water vapour and other greenhouse gases in the atmosphere. Those absorbers emit again long-wave radiation into space and back to the surface according to the law of Stefan-Boltzmann. In contrast to an atmosphere permeable to long-wave radiation this leads to an increased ground temperature - the natural greenhouse effect.

Applying a simple conceptual model it is possible to estimate earth surface temperature as a function of the solar constant S_0, the albedo A and the long-wave absorptivity α. By equating

the flux of incoming short-wave radiation both to the long-wave budget at the ground and at the top of the atmosphere, the temperature of the atmosphere T_A can be eliminated and the equilibrium ground temperature T_G can be calculated as (Feichter and Leisner, 2009):

$$T_G = \sqrt[4]{\frac{S_0\,(1-A)}{2\sigma\,(2-\alpha)}}. \tag{2.2}$$

where σ denotes the Stefan-Boltzmann constant.

Equation 2.2 shows that ground temperature is increasing as the solar constant or the long-wave absorptivity (for example an increase of green house gases) is increasing. Otherwise ground temperature decreases while the albedo is increasing. Obviously it is an oversimplified model and neglects important physical and dynamical properties of the atmosphere, like the vertical temperature gradient, the wavelength-dependency of α and the flux of latent heat by water vapour. Yet it gives a good estimate of the ground temperature for realistic values of $\alpha \approx 0.8$ (Feichter and Leisner, 2009) with $T_G \approx 288\,K$.

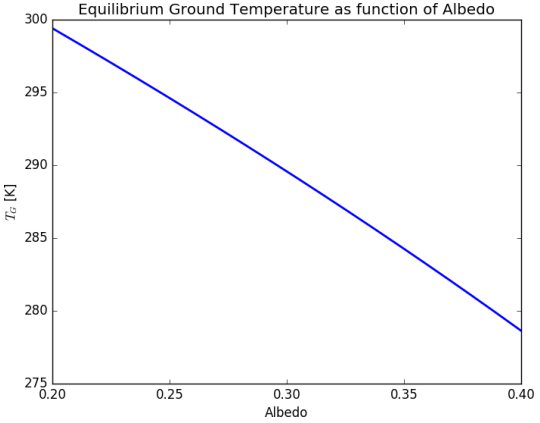

Figure 2.1: T_G as function of albedo, while absorptivity α is constant at 0.8.

This simple model demonstrates that changing one parameter could change T_G and this is the basic approach of climate engineer-

ing. The aim is to change one of those parameters to counteract the increase of T_G caused by anthropogenic induced climate change. At the end the target is to cancel or at least postpone ("Buy some time") the anthropogenic caused climate change.

This is exemplary shown in figure 2.1, where the absorptivity α is held constant at a value of 0.8, while the planetary Albedo A is varied. It is clear that only a minimal change of A would lead to a significant change in T_G. For example an increase of A by 0.02 from the current value would lead to a decrease of T_G by 2.0 K.

3 A Short Introduction to Aerosols

Aerosols are a mixture of solid or liquid particles dispersed in a gas, usually air. Although they are very small and can only be seen with bare eye in high concentrations, they have an important effect on radiation and clouds and therefore on earth's radiation budget.

Composition and distribution is depending on their source and atmospheric residual times. Depending on their size which range from few nanometeres to several micrometers aerosols have a different residual time in the atmosphere and chemical compositions. In general aerosols are divided into two groups: *primary* and *secondary aerosol*. Primary aerosols are emitted directly as particles. Secondary aerosols on the other hand are formed by gas-to-particle processes. To the first group belong particles like mineral dust and sea salt, which have a typical diameter of a few micrometers. Secondary particles consist of a mixture of sulfate, ammonium, nitrate and organic matter. Particles can be produced by nucleation and have a diameter of few nanometers. They grow by condensation of vapours and coagulation with other particles and reach diameters of several nanometers.

Table 3.1: Aerosol size ranges.

	Size range	typical components	dominant sink
Nucleation mode	$\leq$ 10 nm	sulfate	growth by coagulation and condensation
Aitken mode	10 nm $<$ d $\leq$ 100 nm	sulfate, soot	growth by coagulation and condensation
Accumulation mode	100 m $<$ d $\leq$ 1 μm	all	in-cloud scavenging
Coarse mode	1 μm$<$ d $\leq$ 10 μm	sea salt, dust	sedimentation
Supercoarse mode	10 μm$<$ d	sea salt, dust	sedimentation

Aerosols originate from different sources like formation due to nucleation from gaseous precursors (usually by photochemical processes), or released by anthropogenic activities, or released by natural processes at the surface. Mineral dust and sea salt are accounted to the latter process. They are primary aerosols, since they result from interactions of wind with bare soil or ocean surface. Although aerosols are always present in the atmosphere their concentration is highly variable over time and space. This is

related to the large heterogeneity of their sources and relatively short residence time in the troposphere. Properties of aerosols vary spatially and over time and some of these properties vary more or less systematically with the type of environment. Therefore they can be categorized into *urban aerosols, continental aerosols, desertic aerosols, marine aerosols, volcanic aerosols* or *stratospheric aerosols*. But this is only a first approximation, since aerosols can be advected over long distances. It is possible to find marine aerosol over continent or continental aerosol over ocean. Or even desertic aerosol far away from any desert, like saharan dust over Europe or even over the Amazon Basin (Pérez et al., 2006; Swap et al., 1992). The mentioned classification although is useful if local effects are dominating (Boucher, 2015). The number concentration of the particles is highly variable, as they can reach values of $10^6\,\mathrm{cm}^{-3}$ in urban environments, and $10^3\,\mathrm{cm}^{-3}$ in rural areas, and only up to $10^2\,\mathrm{cm}^{-3}$ in maritime environments.

As indicated before the aerosol can be classified by its origin, where natural sources are distinguished from anthropogenic sources. Natural sources are considered to be emissions from the ocean, soils, vegetation, fires, and volcanoes. On the other side anthropogenic sources are mainly dominated by emissions from the combustion of fuels (including fossil fuel, biofuel, and other fuels), or from vegetation fires caused by human activities. Further important anthropogenic sources of aerosols are industrial activities, transportation, heating or even domestic activities like cooking (Boucher, 2015).

Once emitted aerosols are transported by winds but they are also subject to removal processes, so called *atmospheric sinks*. Aerosols are removed out of the atmosphere by sedimentation, dry deposition at the surface and wet deposition by precipitation. In a range of $0.1\,\mu$m and $2.5\,\mu$m removal processes are very inefficient and therefore particles in this size range have the longest lifetime - the so called *accumulation mode* (see table 3.1). The smallest and largest particle have normally a residence time in the troposphere from hours to days, while in the intermediate size range residence times can increase to days or 1-2 weeks (Boucher, 2015).

Aerosols influence climate in a number of ways, as they interact with clouds and radiation which makes them to an important factor of the earth radiation budget (Boucher, 2015):

- They interact with solar (short-wave) radiation by scattering, which leads to a reduction of incoming solar radiation (cooling) and absorption of solar radiation (only warming in aerosol layer). Aerosols also scatter and absorb terrestrial (long-wave) radiation emitted by Earth's surface. These processes are been called *aerosol direct effect* or also in a newer term *aerosol-radiation interactions*.

- Aerosols modify vertical temperature profile by absorption of radiation, which impacts relative humidity, atmospheric stability and therefore cloud formation. This is traditionally called *aerosol semi-direct effect*, which can also be seen as *rapid adjustment* of the atmospheric state due aerosol-radiation interactions.

- As aerosols can act as cloud condensation nuclei they impact cloud properties. An increase of cloud condensation nuclei leads in general to an increase of cloud droplets. For a fixed value of liquid water content, this leads to a decrease in cloud droplet size, which increases the reflectivity of clouds. This traditionally called the aerosol *first indirect effect*. A more general term including this effect would be *aerosol-cloud interactions*.

- Modification of cloud droplets also change the microphyiscal properties of the cloud and therefore impact cloud evolution. In particular the ability of clouds to generate precipitation. This is traditionally called *second indirect effect*.

- They also impact mixed-phase clouds through their role as ice nuclei, which is often referred to a *glaciation effect*, but is also part of *aerosol-cloud interactions*.

- By sedimentation and deposition on snow or ice surfaces aerosols make the surfaces less reflective, which leads to a warming of the surface and therefore leading to a warming of the climate.

This shows the important coupling between aerosols, clouds and the impact on climate, as aerosols influence microphysical and optical properties of clouds due to their function as *cloud condensation nuclei* for liquid-phase clouds and their function as

ice nuclei for ice-phase clouds. This includes changes in properties of mixed-phase clouds. But aerosols are also influenced by clouds, as precipitation contributes to removal of aerosols from the atmosphere, and therefore clouds represent an important sink for atmospheric aerosol through wet deposition.

4 Aerosols and Clouds

4.1 Impacts of Clouds on Climate

Clouds are one of the most significant elements of the atmospheric system and therefore playing several important roles. They play a key role in the radiation budget of the Earth system by reflecting sunlight directly back into space or trapping infrared radiation emitted from the surface. Furthermore precipitation (e.g. rain or snow) contributes to the hydrological cycle. Clouds and precipitation scavenge gaseous and particulate matter out of the atmosphere and return them to the surface (wet deposition). They also provide a medium for wet-phase phase chemistry and production of secondary species.

As clouds scatter more solar radiation than they absorb this results in a significant reflection of solar radiation back to space, which leads to a cooling effect of the climate system. But clouds are also absorbing and emitting terrestrial long-wave radiation causing a greenhouse effect, which leads to a warming of the climate system. It is clear that without clouds the climate on earth would look totally different, but at the end the impact of clouds on earth climate is not just positive or negative. In the end the sign of warming depends on the cloud type. The effect of clouds can be separated into a (negative) short-wave and a (positive) long-wave component. While for low-level clouds the short-wave component is dominating over the long-wave component and therefore low-level clouds have a cooling effect on climate. In case of high-level clouds, which are not too thick, on the other hand the long-wave component is dominating and therefore high-level clouds have a warming effect on the climate (Arking, 1991; Boucher et al., 2013). Radiation is also an important factor for the evolution of clouds, since heating, by absorption, and cooling, by emission of long-wave radiation, modifies the vertical temperature profile in the cloud and therefore its stability. During the "'Earth Radiation Budget Experiment (ERBE)"' a net cooling was found by clouds

(Ramanathan et al., 1989), where the magnitude of the short-wave forcing, resulting from modifying planetary albedo, was larger then the long-wave forcing resulting from the greenhouse effect of clouds. Without clouds planetary albedo would be only half as large as it is now (Ramanathan et al., 1989) and as we could see from equation 2.2 planetary albedo has a large impact on surface temperature.

Because clouds play a major role in the climate system we have to understand how clouds are evolving and which role aerosols play in the formation of clouds. In the following section the basic idea of formation of clouds and the interaction with aerosols are introduced.

4.2 Aerosol Cloud Interaction

4.2.1 Aerosol as Cloud Condensation Nuclei (CCN)

In the atmosphere cloud droplets originate always from aerosol particles. Although it would be possible to form cloud droplets in a particle-free surrounding (homogeneous nucleation) it would need several hundred percent of supersaturation, which is not observed in the atmosphere. Normally values well below 10 % of supersaturation are reached (Pruppacher and Klett, 1997), which indicates that cloud droplets are formed due to *heterogeneous nucleation* involving aerosol particles. All of the aerosol particles which are able to initiate cloud droplet formation are called *cloud condensation nuclei* (CCN).

As already mentioned cloud droplet formation in the atmosphere originates always from heterogeneous nucleation, homogeneous nucleation will not further mentioned here. Furthermore, heterogeneous nucleation will not be discussed in detail here, only the effects of aerosols on cloud formation will be pointed out.

Equilibrium of an Aqueous Solution Drop

The water vapour pressure over a pure droplet is given by the Kelvin-equation (Pruppacher and Klett, 1997; Seinfeld and Pandis, 2006):

$$\frac{p_{wd}(D)}{p^0} = \exp \frac{4M_w\sigma_{v,w}}{RT\rho_w D} \tag{4.1}$$

where p_{wd} is the water vapour pressure over a droplet with diameter D, p^0 is the water vapour pressure over a flat surface at same temperature, M_w is the molecular weight of water, $\sigma_{v,w}$ is the air-water surface tension, ρ_w the water density, R the ideal-gas constant and T the temperature.
The impact of dissolved substances on the equilibrium water vapour pressure can be described by the law of Raoult (Seinfeld and Pandis, 2006):

$$p_s^0 = x_w p^0, \tag{4.2}$$

where p_s^0 is the water vapour partial pressure over a flat solution and x_w is the mole fraction of water in the solution. The solute causes a reduction of the water equilibrium vapour pressure over the solution.

Since atmospheric droplets virtually always contain dissolved material it is obviously to combine both the Kelvin equation and Raoult's law to treat this general case. Therefore equation 4.2 is combined with equation 4.1 which results in:

$$\frac{p_{wd}(D)}{p^0 x_w} = \exp \frac{4M_w\sigma_{v,w}}{RT\rho_w D}. \tag{4.3}$$

The volume of the droplet can be described by:

$$\frac{1}{6}\pi D^3 = n_w\hat{v}_w + n_s\hat{v}_s, \tag{4.4}$$

where n_x is the number of moles and $\hat{v}_x$ is the molar volume and $x\epsilon\{w,s\}$[1]. In addition the mole fraction x_w can be written as:

$$x_w = \frac{n_w}{n_w + n_s} \tag{4.5}$$

and with equation 4.4 it is possible to derive following relationship:

$$\frac{1}{x_w} = 1 + \frac{n_s}{n_w} = \frac{n_s\hat{v}_w}{\frac{\pi}{6}D^3 - n_s\hat{v}_s}. \tag{4.6}$$

[1] w for water and s for the solved material

With the expression of equation 4.6 the molar fraction appearing in 4.3 can be replaced and it follows:

$$\ln\left(\frac{p_{wd}\left(D\right)}{p^0}\right) = \frac{4M_w\sigma_{v,w}}{RT\rho_w D} - \ln\left(1 + \frac{n_s\hat{v}_w}{\frac{\pi}{6}D^3 - n_s\hat{v}_s}\right). \tag{4.7}$$

If the solution is dilute the volume occupied by the solute compared to the volume of the droplet can be neglected, so that $n_s\hat{v}_s \ll \frac{\pi}{6}D^3$. Furthermore the molar volume of water can be expressed as $\hat{v}_w = \frac{M_w}{\rho_w}$ and with those two assumptions equation 4.7 can be written as:

$$\ln\left(\frac{p_{wd}\left(D\right)}{p^0}\right) = \frac{4M_w\sigma_{v,w}}{RT\rho_w D} - \frac{6n_sM_w}{\pi\rho_w D^3}, \tag{4.8}$$

where the assumption that $\ln\left(1+x\right) \approx x$ for $x \to \infty$ is used. The number of moles n_s can expressed by the properties of the dissolved dry aerosol particle in the solution drop:

$$n_s = \frac{\nu_s\pi D_p^3\rho_s}{6M_s}, \tag{4.9}$$

where ν_s is the dissociation factor of the solute, D_p the dry diameter of the dissolved particle, M_s the molecular weight of the solute, and ρ_s the density of the solute. Equation 4.8 is known as Köhler equation and commonly simplified to

$$\ln\left(\frac{p_{wd}\left(D\right)}{p^0}\right) = \frac{A}{D} - \frac{B}{D^3} \tag{4.10}$$

$$\text{with} \quad A = \frac{4M_w\sigma_{v,w}}{RT\rho_w} \quad \text{and} \quad B = \frac{6n_sM_w}{\pi\rho_w} \tag{4.11}$$

The Köhler equation 4.10 shows two aspects which determine the vapour pressure over an aqueous solution droplet:

- the Kelvin effect which tends to increase the vapour pressure (first term on the r.h.s.)

- the law of Raoult (or solute effect) which tends to decrease the vapour pressure (second term on r.h.s)

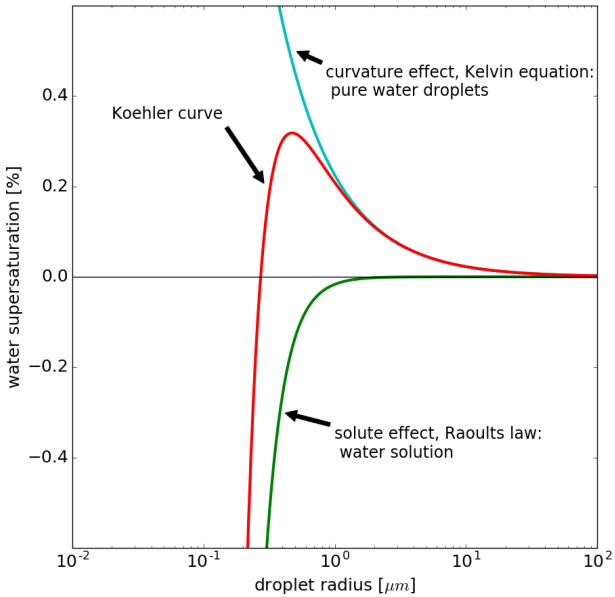

Figure 4.1: Koehler curve of a NaCl solution drop with dry diameter of 0.05 μm.

The equilibrium saturation can be defined as $S_{eq} = \frac{p_{wd}}{p^0}$ and because clouds form in a saturation regime very close to 1 it is possible to replace the equilibrium saturation S_{eq} by the equilibrium supersaturation $s_{eq} = S_{eq} - 1$. The Köhler equation for a solution droplet with NaCl as solute is shown in figure 4.1. In figure 4.2 the equilibrium supersaturation for a solution droplet conatining NaCl is shown but with different dry diameters for the aerosol particle. It is already obvious that the size of the participating aerosol particles during cloud formation is an important factor. Also it follows that larger particles have a lower equilibrium supersaturation.

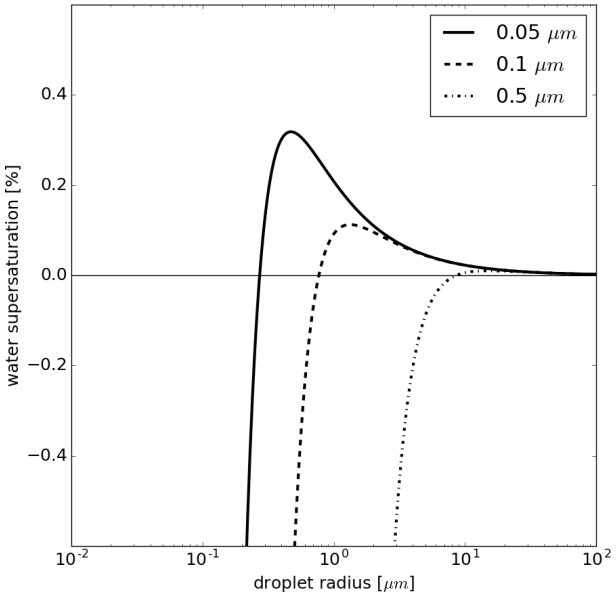

Figure 4.2: Same as figure 4.1 but with different dry diameters.

It is obvious that every curve in figure 4.2 pass through a maximum which is called the *critical supersaturation* s_{crit} and reaches its maximum at the *critical droplet diameter* which can be derived from equation 4.10 by determining the maximum $\left(\frac{\mathrm{d}s_{eq}}{\mathrm{d}D} = 0\right)$:

$$D_{crit} = \left(\frac{3B}{A}\right)^{1/2} \tag{4.12}$$

and it yields for the corresponding critical saturation:

$$\ln S_{crit} = \left(\frac{4A^3}{27B}\right)^{1/2} = \left(\frac{4A^3\rho_w M_s}{27\nu_s\rho_s M_w D_p^3}\right)^{1/2} \tag{4.13}$$

From equation 4.13 it follows that with an increasing diameter the Kelvin effect is dominating over the solution effect. Very clearly seen in case of the diameters greater then D_{crit}.

Assuming a constant ambient supersaturation and concentrating on the part where $D < D_{crit}$ it will be explained that the droplet is in a stable equilibrium. The drop will face constantly small perturbations due to a gain or loss of a little amount of water molecules. If this leads to a small growth of the droplet the equilibrium vapour pressure is higher than the ambient saturation and the droplet will shrink again due to evaporation of water. Perhaps returning to its original equilibrium state. On the other hand considering a small loss of molecules the droplet will shrink and now the equilibrium water vapour pressure of the droplet is lower than the ambient value and water will condense on the droplet, also returning to its original state. On the rising part of the Köhler curve the droplet is in a stable equilibrium with its environment.

Highlighting now the part of the curve where $D > D_{crit}$ and a droplet is experiencing small perturbations by gaining a small amount of water molecules. This leads to a slight increase of the droplet. Now its equilibrium vapour pressure is smaller than the ambient value and water will condense on the drop and it will grow further. On the other side a small shrinkage by a loss of few water molecules would lead to a further evaporation of the droplet because of its higher equilibrium vapour pressure. A pure water droplet would evaporate completely and a drop containing a solute would shrink until it intersects the ascending branch of the Köhler curve corresponding to the stable equilibrium. The descending branch of the Köhler curve corresponds to an unstable equilibrium.

Assuming that the ambient saturation S exceeds the critical saturation S_{crit} there would be no feasible equilibrium size for the particle since S would be always greater than the equilibrium vapour pressure of the droplet and the drop would grow infinitely. Therefore an aerosol droplet can grow fast to the size of a cloud

(or fog) droplet. In this case the aerosol droplet would be called activated.

It can be noted that S_{crit} is always higher than unity and analogous define the critical supersaturation as $s_{crit} = S_{crit} - 1$.

From equation 4.13 it follows that the critical saturation is a function of the dry diameter D_p of the particle. If follows that smaller particles posses a higher S_{crit} which means that larger particles are faster activated to cloud droplets. Assuming a fixed S all particles with $S_{crit} > S$ would grow until they reach an equilibrium size corresponding to the point of the stable part of the Köhler curve. On the other hand all particles with $S_{crit} < S$ become activated and grow indefinitely as long as $S > S_{crit}$.

This can be seen in figure 4.2 where the Köhler curve is plotted for three particles with different dry diameters. Smaller particles need a higher supersaturation to get activated to cloud droplets. Larger particles on the other hand would need a lower supersaturation for activation.

It should be noted that aerosol activation process is treated instantaneous, which underlays the assumption that aerosol particles have enough time to grow to D_{crit}. In case of large particles this can lead to errors in the calculation since particle growth is proportional to D^{-1} and they grow to slowly to reach D_{crit} during the typical time if $s > s_{crit}$. This limitation of transfer rates on growth rate is called kinematic limitations and can cause deviations from assumptions of instantaneous activation (Nenes et al., 2001).

Calculation of Supersaturation in an Ascending Air Parcel

In the previous chapter it was shown that the activation of an aerosol particle to a cloud droplet depends on the ambient supersaturation s in case of $s > s_{crit}$. During cloud formation s is mainly determined by the adiabatic cooling rate, which leads to an increase in s, and by condensation of water, which causes an decrease in s. Those two processes determine variation of s over time and the rate of change of supersaturation has to be derived. This can be written, if mixing processes with environment and diabatic cooling is neglected (Seinfeld and Pandis, 2006), as:

$$\frac{\mathrm{d}s}{\mathrm{d}t} = \alpha w - \frac{\gamma}{\rho_a}\frac{\mathrm{d}q_c}{\mathrm{d}t} \tag{4.14}$$

The first term on the r.h.s. of equation 4.14 is the contribution by adiabatic cooling, where the second term on r.h.s. is contribution by condensation of water within the ascending air parcel. In equation 4.14 q_c is the mass concentration of water and w is the vertical velocity. The factors α and γ are depending on pressure, temperature, physical constants and are given by (Seinfeld and Pandis, 2006):

$$\begin{aligned} \alpha &= \frac{l_{wv} M_w g}{c_p R T^2} - \frac{g M_a}{RT} \\ \gamma &= \frac{p M_a}{p^\circ M_w} + \frac{l_{wv}^2 M_w}{c_p R T^2} \end{aligned} \tag{4.15}$$

where g is the gravitational acceleration, M_a the molar mass of air, l_{wv} latent heat of evaporation, c_p the specific heat capacity of air at constant pressure. Note that during deriving equation 4.14 the assumption $S = 1 + s \approx 1$ was made since s reaches values of $s \approx 0.01$ within clouds. In absence of condensation, supersaturation is increasing linearly with the vertical velocity. On the other side supersaturation is decreased by condensation of water. This suggests that supersaturation within a cloud is a balance between the cooling rate and the liquid water increase. Latter is limited by mass transport to the cloud particles and this depends on the particle size distribution and their state of activation.

An important quantity is the maximum supersaturation reached during cloud formation. Particles with a critical supersaturation lower than the reached maximum supersaturation are activated and grow to the size of a cloud droplet. While particles with a critical supersaturation larger than reached maximum supersaturation remain near equilibrium and never grow enough to be considered as a cloud droplet and called *interstitial aerosol*. In principle the aerosol population within a cloud can be separated into two groups: Interstitial aerosols, which contain a significant amount of water but are not activated and cloud droplets, which sizes change significantly due to corresponding mass changes (Seinfeld and Pandis, 2006).

4.2.2 Impact of Aerosols on Cloud Optical Properties

Beside the effect of aerosols on microphysical processes of a cloud, they also have an impact on cloud optical properties. In this section the cloud optical properties are discussed for a simple case of sunlight crossing a single cloud layer (Petty, 2004). Following the Beer's law the transmittance t_c of a single cloud is given by:

$$t_c = e^{-\tau_c/\mu}, \tag{4.16}$$

where τ_c is the cloud optical thickness and μ the cosine of the solar zenith angle.
The optical depth τ_c is defined as:

$$\tau_c = \int_{z_{cb}}^{z_c t} \beta_{ext,c}\,(z)\,\mathrm{d}z, \tag{4.17}$$

with the extinction coefficient $\beta_{ext,c}$, and z as vertical coordinate given in metres. The limit z_{cb} defines the height of the cloud base and z_{ct} defines the height of the cloud top.

The extinction coefficient can be calculated by

$$\beta_{ext,c} = \int_0^\infty Q_{ext}\pi r^2 n_c\,(r)\,\mathrm{d}r, \tag{4.18}$$

where Q_{ext} is the dimensionless extinction efficiency, $n_c\,(r)$ is the droplet size distribution and r is the cloud droplet radius. Assuming a monodisperse cloud and using $Q_{ext} = 2$ as a good approximation for cloud droplets and visible light (Petty, 2004) it yields:

$$\beta_{ext,c} = 2N_c\pi r^2. \tag{4.19}$$

Using that $q_c = (4/3)\pi\rho_w N_c r^3$ it follows:

$$\beta_{ext,c} = \frac{3}{2}\frac{q_c}{\rho_w r}. \tag{4.20}$$

Substituting Eq. 4.20 into Eq. 4.17 it yields for the optical depth:

$$\tau_c = \frac{3}{2\rho_w r} LWP, \tag{4.21}$$

where $LWP = \int_{z_{cb}}^{z_i ct} q_c \mathrm{d}z$ is the liquid water path of the cloud layer in $\mathrm{g\,m^{-2}}$. From equation 4.21 it follows that $\tau \propto 1/r$ and $\tau \propto LWP$. A fixed LWP leads to an increase in cloud optical depth if the radius of the cloud droplet is decreased. By substituting r in Eq. 4.21 it yields:

$$\tau_c \approx \left(\frac{9}{2} \frac{LWP^2 \pi \left(z_{ct} - z_{cb}\right)}{\rho_w} N_c \right)^{1/3}. \tag{4.22}$$

For a cloud with a fixed LWP and a fixed geometrical thickness optical thickness τ_c is proportional to $N^{1/3}$. Since N_c is determined by the number concentration of activated aerosol particles, τ_c also depends on the aerosol particles which are present during cloud formation process.

In reality clouds contain droplets of different sizes and therefore τ_c is a function of the cloud droplet size distribution. This can be expressed by the cloud effective radius r_{eff}.

$$\beta_{ext} \approx \frac{3}{2} \frac{LWP}{\rho_w r_{eff}}. \tag{4.23}$$

Impacts on cloud optical properties due to a change of aerosols compared to a certain low background concentration of aerosols is visible during the formation of so called 'ship-tracks' (Coakley et al., 1987), where optical thick clouds occur in the vicinity of ship exhausts although stratified optical thin clouds are prevailing.

4.2.3 Impact of Aerosols on Cloud Albedo

Following Seinfeld and Pandis (2006) the cloud albedo A_c can be written as a function of cloud optical thickness τ_c (in case that the radius of cloud droplets is much larger than the wavelength):

$$A_c = \frac{\tau_c}{\tau_c + 7.7}. \tag{4.24}$$

In Figure 4.3 the dependency of A_c on τ_c is shown. If $\tau_c \to 0$ also $A_c \to 0$. But in case of $\tau_c >> 7.7$ it follows that $A_c \to 1$.

To establish the link between changes in cloud droplets N_c and cloud albedo A_c it can be assumed that A_c is a function of N_c,

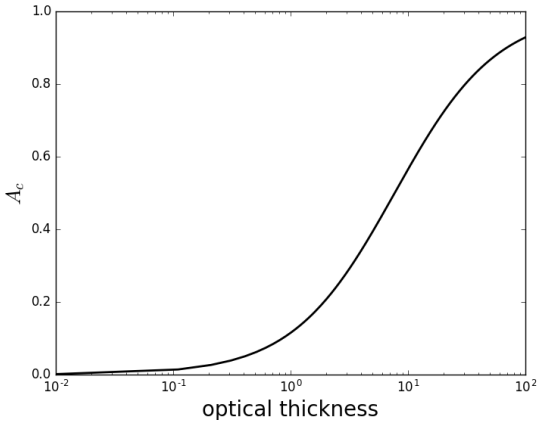

Figure 4.3: Cloud albedo as a function of optical thickness (Seinfeld and Pandis, 2006)

LWP and $h = z_{ct} - z_{cb}$ (Seinfeld and Pandis, 2006) and it yields for the derivative $\mathrm{d}A_c/\mathrm{d}N_c$:

$$\begin{aligned}\frac{\mathrm{d}A_c}{\mathrm{d}N_c} =& \frac{\mathrm{d}A_c}{\mathrm{d}\tau_c}\frac{\mathrm{d}\tau_c}{\mathrm{d}N_c} \\ =& \frac{\mathrm{d}A_c}{\mathrm{d}\tau_c}\left(\frac{\partial\tau_c}{\partial h}\frac{\mathrm{d}h}{\mathrm{d}N_c} + \frac{\partial\tau_c}{\partial LWP}\frac{\mathrm{d}LWP}{\mathrm{d}N_c} + \frac{\partial\tau_c}{\partial N_c}\right).\end{aligned} \tag{4.25}$$

Usually it is assumed that there is no dependence of LWP on N_c. Furthermore, it is assumed that there is no dependence of cloud thickness h on N_c (Seinfeld and Pandis, 2006). Those derivates become zero and it follows:

$$\begin{aligned}\frac{\mathrm{d}A_c}{\mathrm{d}N_c} =& \frac{\mathrm{d}A_c}{\mathrm{d}\tau_c}\frac{\partial\tau_c}{\partial N_c} \\ =& \left(\frac{A_c}{\tau_c}(1-A_c)\right)\left(\frac{\tau_c}{3N_c}\right) \\ =& \frac{A_c(1-A_c)}{3N_c}.\end{aligned} \tag{4.26}$$

Twomey (1991) termed the quantity $\mathrm{d}A_c/\mathrm{d}N_c$ *susceptibility* and determines the sensitivity of cloud reflectance according to changes in the cloud microphysical properties. From equation 4.26 it follows that the susceptibility has its maximum at $A_c = 0.5$ and because it is inverse proportional to N_c it becomes high when N_c is low (for a fixed A_c). Furthermore it is clear from figure 4.4 that A_c is most sensitive to changes between values of 0.25 and 0.75 and if N_c is low.

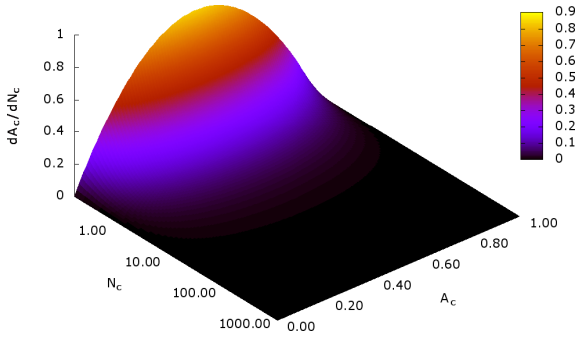

Figure 4.4: Susceptibility of cloud reflectance to changes in N_c for a cloud with constant liquid-water content. $\Delta A/\Delta N_c$ is % per unit N_c. Adapted from Seinfeld and Pandis (2006)

5 Marine Cloud Brightening as a Technique for Climate Engineering

Main target of Climate Engineering[1] is to counteract global warming caused by an increase in CO_2-level. An early mention of Climate Engineering in literature can be found in the work of Marchetti (1977). He describes in his work the deep-sea disposal of $CO_2$to counteract the problems accompanied with the rise of the CO_2-level in the atmosphere. Since then, but especially in the last few years, new proposals to counteract the increase of global mean temperature were made. The proposals can be separated into two main categories. First category is based on manipulating the solar insolation on the earth surface. Therefore all proposals which target the direct change of incoming solar radiation is summed up in the generic term 'Solar Radiation Management' (SRM). The second category refers to techniques with the objective to remove CO_2 from the atmosphere. Therefore this category is often regarded as 'Carbon Dioxide Removal'(CDR).

CDR will not be part of this work and it is referred to corresponding literature. The next part will present a short overview of the different methods of SRM but with a more detailed focus on marine cloud brightening - the main topic of this work.

As mentioned before SRM is targeting solar insolation. Several examples and ideas can be found in literature and they range from space born schemes to modifications on city buildings. Table 5.1 gives a short overview of several techniques and gives one example. One hot topic discussed as a technique of SRM is stratospheric aerosol injection (SAI), where aerosol particles are released into the stratosphere and enhancing the reflectivity of the earth. A natural guide to this technique is the eruption of the volcano

[1] also called 'Geoengineering'

Pinatubo, where afterwards the global mean temperature was slightly decreased. For a more detailed perspective into SAI it is referred to the corresponding literature.

Table 5.1: Overview of different types of solar climate engineering

SRM Technique	Examples
Space-based schemes	Mirrors in space
Stratospheric aerosols	Sulfate particles in stratosphere
Cloud brightening	Enhanced Albedo of low-level clouds
Ocean whitening	Bubbles in vast regions of ocean
Plant reflectivity	Crops with higher albedo
Change properties of buildings	Whitening of roofs

As already mentioned in chapter 4.1 clouds play a major role in the Earth's energy budget by scattering light back into space. Due to the very low albedo of ocean water marine low-level clouds above are very effective in reflecting sunlight. Changing the albedo, lifetime or areal extent of these type of clouds could lead to an impact on radiation not only on local but also on global scale.

Chapter 4.2.2 and 4.2.3 show that changes in N_c is accompanied with changes in cloud optical properties. These changes underlay the assumptions of a constant liquid water content and a fixed cloud depth (Twomey, 1977). This assumption (same liquid water volume) means that with smaller particles a larger surface area is gained which leads to an increase in light scattering. Since brightening of clouds due to an increase in N_c was highlighted by Twomey (1977) this effect is also known as Twomey effect. Often this effect is also referred to the *first indirect aerosol effect*. The idea to deliberately modify cloud albedo of marine low-level clouds is most commonly known as "marine cloud brightening" (MCB).

But MCB is accompanied by limitations. First of all MCB is limited to a certain type of cloud. Second the clouds must have a low albedo. Clouds with a high albedo for example are already reflecting nearly 100% of the incoming solar radiation and the addition of aerosol particles would only have a little or none effect on albedo (compare figure 4.4). For this reason large cumulus clouds, clouds associated with big storm systems and substantial precipitation are not susceptible to aerosol modification. Of course there could be other feedbacks on cumulus clouds by modification of aerosol concentration that change precipitation, areal extend and lifetime of the clouds (Rosenfeld et al., 2013). This could have subsequent effects on cloud radiative forcing, but the processes are at the moment better understood for pure warm-phase clouds, while processes taking place in mixed-phase clouds are currently less understood. High-level clouds on the other hand are not targeted in case of MCB. But recently the idea of dissolving cirrus clouds rather than enhancing them emerged to counteract anthropogenic caused global warming (Mitchell and Finnegan, 2009; Storelvmo et al., 2013; Storelvmo and Herger, 2014).

Therefore only low-level boundary layer clouds are considered for MCB. A further limitation is the occurrence of suitable low-level clouds, which are often limited to small regions of the planet and therefore large changes in the local energy-fluxes are necessary to produce a significant planet-scale change. The local effectiveness is mainly limited by two conditions: A relatively low underlying albedo (below the clouds) and clouds with low N_c. These conditions are found in four major regions on the planet (Korhonen et al., 2010) which share all the same conditions: persistent marine stratocumulus clouds (SCU). The four regions are namely: North East Pacific, South East Pacific, South Atlantic, Indian Ocean.

In former studies those four regions were found to be the most favourable (Salter et al., 2008) and together they cover around 13% of the earth's surface. Those regions could also be identified by satellite observations which investigated the sensitivity of clouds to changes in aerosol loadings (Andersen et al., 2016). According to the simulations of Korhonen et al. (2010) and the observations of Platnick and Oreopoulos (2008) and Andersen et al. (2016) one of the most favourable region is the South East Pacific (SEP) due to small changes in aerosol loading. This is one reason why this region was chosen in this work.

On the basis of the work of Twomey (1977) Latham et al. (2008) developed the idea to change cloud albedo of low-level marine clouds by adding additional aerosols near cloud base. The enhanced aerosol concentration would increase the number of available CCN and increase the cloud droplet number concentration N_c. The increase of N_c would lead to a change of cloud properties and as a consequence the clouds would be more reflective.

Latham et al. (2008) suggested the same regions for seeding which are mentioned before. The additional aerosol has to be injected into the planet boundary layer (PBL). For this purpose he suggests to use seawater which should be sprayed into the lower troposphere. This could be for example achieved by ships (Latham et al., 2008; Salter et al., 2008).

In addition the residual time of aerosol particles in the PBL is quite short where the aerosol load is mainly driven by frontal precipitation or local drizzling events, for example where marine stratocumulus clouds are quite frequently occurring. Therefore the aerosol concentration is highly fluctuating. The residual time is about 2 - 5 days in the PBL (Coakley Jr et al., 2000). This results in highly variable changes in cloud albedo and radiative forcing in space and time. Following that the injections must be more or less continuous, which is quite different to the discussed deployment distributions in case of SAI, where aerosol forcing can spread globally and has much longer residual times.

The effect of high amount of aerosol particles on low-level clouds in an otherwise pristine surrounding is already observable. Indeed there is evidence that cloud albedo can be modified by human activities by releasing aerosol particles. In figure 5.1 there are so called 'ship tracks' visible at the coast of California. Lines of clouds which are brighter than the surrounding clouds are visible. Those clouds are influenced by aerosol particles originating from ship exhausts. The emitted particles can act as CCN within the marine boundary layer. Schreier et al. (2006) investigated the cloud optical properties of ship tracks with satellite data and found that below ship tracks mean solar surface radiation is reduced and mean top of the atmosphere reflectance is increased. In a further study Russell et al. (2013) used controlled particle emissions by smoke generators on a vessel much smaller than cargo ships. Although it could be shown that those emissions had a positive effect on cloud albedo, it was only effective for a small fraction of time, even

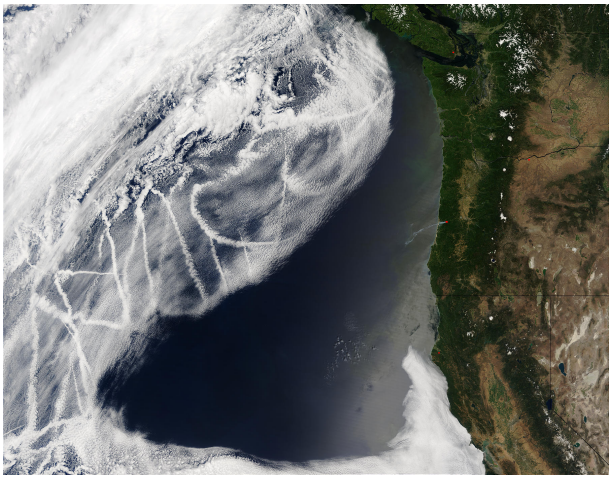

Figure 5.1: Visible satellite image which shows Ship Tracks retrieved by NASA's Terra MODIS. Source: http://visibleearth.nasa.gov/view.php?id=66963

in clouds which were classified as susceptible to additional CCN. However this experiment could show that it is possible to influence cloud albedo with a quite simple technology.

To deploy the additional particles in the atmosphere several aspects have to be taken into account. Since the particles are released near the surface they have only a residual time of a few days. Therefore they will remain very near to their source, since they will not be advected over large distances before they are removed by scavenging or deposition. Because of that they have to be replenished continuously over a large area. To achieve a significant change in global albedo a large fleet of vessels would be needed for large-scale deployment, which would be able to seed susceptible clouds in favourable regions (Salter et al., 2008). Since composition and size affects the efficiency of MCB it is vital which kind of particles are deployed. From chapter 4.2.1 it follows that larger, hygroscopic particles are a more efficient CCN. Latham (2002) suggested that seawater could be an unlimited reservoir for additional aerosol particles. He proposed that the release of sea spray into the boundary layer would lead to evaporation of the

small droplets and form small sea salt particles, which then would be available as CCN.

But this could turn out to be very difficult because due to the size and amount of the released particles there could be competitive effects in cloud formation. With the release of additional particles supersaturation is reduced, which leads to the fact that an increase in aerosol particles may not lead to an increase in cloud droplet number concentration and hence cloud albedo. The size of the particles is important, since larger particles are more effective to develop to cloud droplets. As they form cloud droplets they are reducing supersaturation, which leads to a suppression of the cloud droplet activation of smaller aerosol particles. This could influence cloud formation in a way that smaller particles may have been activated without seeding, but are not activated with seeding. Therefore seeding could lead to lower cloud droplet number concentrations, accompanied by larger sized cloud droplets. This would be the opposite effect which is intended by MCB, a 'negative' Twomey effect. Jung et al. (2015) could measure an increase in cloud droplet size and a decrease in cloud droplet number concentration after seeding stratocumulus clouds with salt powder in the range of 1 - 10 μm in diameter. Therefore the efficiency of MCB depends on the size of the released sea salt particles and because of that the sea salt particles which are proposed to be released for MCB should be smaller than 1 μm.

To evaluate the impact of MCB Latham et al. (2008) made a simple assumption of the change of cloud droplets ΔN_c which would be necessary to counteract a warming of 3.7 Wm^{-2} due to a doubling of CO_2. This underlies some simplifications, like only taking the Twomey effect into account and that only marine stratocumulus clouds are seeded which are not overlaid by other clouds, like a cirrus above. And only short-wave radiative forcing is taken into account. The mean insolation L on reaching earth can be described by:

$$L = 0.25 S_0 \, (1 - A) \tag{5.1}$$

where changes in albedo ΔA leads to a change in radiative forcing ΔL and using the value for S_0 it yields:

$$\Delta L = -340 W m^{-2} \Delta A \tag{5.2}$$

By defining the fraction of ocean surface $f_1 = 0.7$ to earth surface, and the fraction of non-overlaid marine stratocumulus clouds over ocean $f_2 = 0.25$, and the fraction of seeded clouds f_3 it is possible to relate changes in cloud albedo A_c to changes in global albedo A. By using equation 5.2 for ΔA it results in:

$$\Delta A_c = \frac{\Delta A}{f_1 f_2 f_3} = -\frac{\Delta L}{60 W m^{-2} f_3}. \tag{5.3}$$

If it is possible to seed all suitable clouds ($f_3 = 1$) it would only need an increase of $\Delta A_c = 0.062$, meaning a 12% increase, to counteract the forcing due to CO_2 doubling.

The impact on A_c by a change of cloud droplet from a base value $N_{c,0}$ to a new value N_c can be described by following relationship (Schwartz and Slingo, 1995):

$$\Delta A_c = 0.075 \ln \left(N_c / N_{c,0} \right) \tag{5.4}$$

which then can be used in equation 5.3:

$$\begin{aligned} -\Delta L &= 4.5 W m^{-2} f_3 \ln \left(N_c / N_{c,0} \right) \\ \left(N_c / N_{c,0} \right) &= \exp \left(-\Delta L / 4.5 W m^{-2} f_3 \right) \end{aligned} \tag{5.5}$$

This shows that for $f_3 = 1$ the ratio $N_c/N_{c,0}$ would have to reach a value of 2.3 to achieve a negative forcing of -3.7 Wm^{-2} to compensate for CO_2 doubling. On the other side Latham et al. (2008) shows that if $f_3 < 0.3$ it is not achievable to compensate for CO_2 doubling. He also sees a value below 10 reasonable for the ratio $N_c/N_{c,0}$. But still this is a rough assumption for what would be needed to counteract 3.7 Wm^{-2}. Since only simple assumptions are made for this calculation, as only short-wave feedbacks are taken into account. Also only aerosol-cloud-radiation-interactions are taken into account (Twomey effect). An even more intriguing question is, if it is technical possible to seed continuous more then half of the clouds around the world. For the technical aspects of seeding by ships see Salter et al. (2008).

MCB is still a challenge for global climate models (GCMs) as clouds and aerosols and their interactions are difficult to represent in GCMs which is caused by their coarse resolution. But the coarse resolution is necessary to simulate years and decades in a reasonable computational time. Therefore cloud processes have to

be parametrized in simple ways. With this compromise boundary layer clouds, like those essential for MCB, are poorly represented in GCMs, which lead to unidentified biases and uncertainties in their simulations.

Table 5.2: Overview of global studies regarding MCB. Alterskjær and Kristjánsson (2013) made simulations for different sized emission particles (aitk = aitken mode, acc = accumulation mode, coa = coarse mode).

Publication	Fixed CDNC	Injected global area	radiative forcing [Wm^{-2}]
Alterskjær et al. (2012)	-	$> 50\%$	-4.8
Alterskjær and Kristjánsson (2013)	-	$> 50\%$	-3.3 (aitk) 8.4 (acc) 1.2 (coa)
Hill and Ming (2012)	-	$< 10\%$	-0.76
Jones et al. (2009)	375 cm^{-3}	$<10\%$	-0.97
Jones and Haywood (2012)	375 cm^{-3}	$<10\%$	-1.0
Latham et al. (2008)	375 cm^{-3}	10 - 20 %	-8.0
Korhonen et al. (2010)	-	$\approx 10\%$	not given
Partanen et al. (2012)	-	$< 10\%$	-5.1
Rasch et al. (2009)	1000 cm^{-3}	20% 70%	-2.5 -3.9

Table 5.2 gives an overview of several model studies with global models. They are not comparable one to one since the seeding scenarios of the climate engineering studies vary over a wide range. Starting from the seeded area, where some studies seeded the

whole oceans over the world, or areas between 30°N and 30°S (Alterskjær et al., 2012; Alterskjær and Kristjánsson, 2013; Rasch et al., 2009) and other studies seeded only the susceptible areas with marine stratocumulus clouds (Hill and Ming, 2012; Jones et al., 2009; Jones and Haywood, 2012; Partanen et al., 2012).

In general there exist two approaches to investigate MCB with global models. The first approach is quite simple and prescribed important cloud properties are changed like cloud droplet number concentrations N_c. This underlies the assumption that it would be possible to control cloud characteristics perfectly and explore the systematically changes to climate dynamics and response to global mean temperature. Studies with this approach (Latham et al., 2008; Jones et al., 2009; Rasch et al., 2009; Hill and Ming, 2012) identified specific regions over the ocean and then increased N_c (compare table 5.2), which produced changes in cloud radiative forcing. Many of these studies showed a common response in a cooling of the Pacific, similar to a "'La Niña"' phenomenon. Despite its regional scale MCB showed in all the studies a global mean cooling and an increase in polar sea ice.

The second approach allows a broader range of interaction within the GCM to compare simulations with and without added particles into the MBL (Alterskjær et al., 2012; Alterskjær and Kristjánsson, 2013; Korhonen et al., 2010; Partanen et al., 2012). In these studies simulations carried out with added sea salt particles to the lowest model layer and they all found a cooling effect due to a change of cloud albedo caused by the indirect aerosol effect of the seeded particles. On the other side large differences in the predicted regional temperature responses were found. This is not very surprising since differences are also found in changes of precipitation due to global warming comparing different GCMs amongst each other, because processes controlling precipitation are still uncertain in GCMs. Partanen et al. (2012) and Jones and Haywood (2012) could also asses the role of a direct radiative effect of the added sea salt particles to the total radiative impact. Alterskjær and Kristjánsson (2013) found that the sign of forcing depends on the size of emitted particles. The study of Korhonen et al. (2010) only evaluated the changes in N_c but not in radiative forcing since the aerosol model they used incorporated no feedbacks on meteorological fields. But they found that the seeding with additional sea salt particles had an effect on H_2SO_4 since the additional sea

salt particles act as a condensational sink. Although they found a reduction of H_2SO_4 by ≈60% it only had a minor impact on natural particle size distribution and CCN concentration.

The various results shown in table 5.2 from a very high to a very small radiative impact shows the high uncertainties in the results of GCMs. This is on the one hand related to some simple approaches of physical processes which have to be made in GCMs but also due to different seeding approaches, like different emissions fluxes, or the seeded cloud fraction. Among the models there is the indication that MCB is able to reduce global mean temperature and that the targeted susceptible clouds will cool particularly the eastern North and South Pacific. This would also lead to a global cooling, including the cooling of the Arctic. But this must be handled with some caution since cloud processes, especially those for marine low-level clouds, are parametrized in a rather simple way and do not always compare well to observations, especially regarding the Twomey effect. Due to the deficient representation of low-level clouds in GCMs and diversity of model results the IPCC suggests only a low confidence in the sign of low level cloud feedbacks contribution to global warming (Boucher et al., 2013). This of course impacts the evaluation of MCB.

6 The Model System COSMO-ART

During this work the comprehensive model system COSMO-ART is used to investigate the effects of marine cloud brightening on the regional scale. This chapter will give a short overview of the model system COSMO-ART.

COSMO-ART is based on the non-hydrostatic mesoscale weather forecast model COSMO (**C**onsortium for **S**mall-scale **MO**delling) used by the German Weather Service (Deutscher Wetterdienst - DWD, Baldauf et al., 2011). This model has been extended with comprehensive modules for aerosol dynamics and gas phase chemistry. ART is an acronym for **A**erosols and **R**eactive **T**race gases (Vogel et al., 2009). The model is online coupled which means that aerosol and gas phase processes are coupled with the state of the atmosphere and treated in a consistent way since they use the same grid for all scalars, e.g. temperature, humidity, aerosol and gas concentrations. Processes affecting all scalars (e.g. advection) are using the same numerical schemes and time step for integration. This allows to simulate the effects of atmospheric processes on aerosol dynamics and gas phase and vice versa in a consistent manner.

It is possible to simulate the transport of non-reactive tracers, but also the transport of chemical reactive aerosol and gases and their impact on meteorological processes. Secondary aerosols and primary aerosols like soot, dust, sea salt and biological particles like pollen can be taken into account. Spacial and temporal evolution of the reactive trace gases and aerosols are calculated by balance equations of the corresponding substances. Additionally to transport processes like turbulent diffusion, dry and wet deposition, coagulation, condensation and sedimentation are taken into account (Vogel et al., 2009). Washout represents a major sink of aerosol particles which was implemented by Rinke (2008) into COSMO-ART. Since aerosols can act as CCN and therefore

influence the evolution of cloud development the process of aerosol activation on warm phase and cold phase clouds was implemented by Bangert et al. (2011).

The gas phase reactions are calculated by the RADMKA - **R**egional **A**cid **D**eposition **M**odel Version **KA**rlsruhe - mechanism (Vogel et al., 2009) which is based on the gas phase mechanism RADM2 - **R**egional **A**cid **D**eposition **M**odel - (Stockwell et al., 1990). Inorganic species and the calculation of photochemical formation of gaseous precursors regarding the formation of secondary aerosols are calculated by the SORGAM - **S**econdary **ORG**anic **A**erosol **M**odel - mechanism (Schell et al., 2001). The nucleation of secondary aerosol particles is based on the binary homogeneous nucleation of sulfuric acid and water and calculated with the parameterization of Kerminen and Wexler (1994). Further DMS emissions as a precursor of sulfate particles was implemented by Lundgren (2010).

The aerosol module MADEsoot (Vogel et al., 2009) is used to describe the aerosol population by eleven overlapping log-normal sized distributions, so-called modes. The module also describes the aerosol dynamic processes. Since the aerosol population is described by a log-normal size distribution the standard deviation σ_l for every mode is prescribed and held constant over time. Additionally a initial mean diameter $D_{p,l}$ is prescribed for initialisation but D_p can vary together with number and mass concentration. Five modes represent sub-micron particles consisting of sulfate, ammonium, nitrate, organic compounds, water, and soot in a range of mixing states and sizes. This modes can also interact with anthropogenic emissions of aerosols and gases. Sea salt and dust are each represented by three modes for different size ranges. Sea salt and dust emissions are calculated online by modelled atmospheric state, e.g. 10-m wind velocity, friction velocity, surface properties like sea surface temperature and soil properties (Lundgren, 2010; Stanelle et al., 2010). An overview of the modes used in COSMO-ART is given in table 6.1

6.1 Aerosol Treatment

The concept of describing the aerosol population in COSMO-ART is based on the approach of Whitby (1978) who found that observed

Mode	Chemical composition and mixing state	σ_l	Initial D_p (μm)
if	SO_4^{2-}, NO_3^-, NH_4^+, H_2O, SOA (externally mixed)	1.7	0.01
ic	SO_4^{2-}, NO_3^-, NH_4^+, H_2O, SOA, soot (internally mixed)	2.0	0.08
jf	SO_4^{2-}, NO_3^-, NH_4^+, H_2O, SOA (externally mixed)	1.7	0.07
jc	SO_4^{2-}, NO_3^-, NH_4^+, H_2O, SOA, soot (internally mixed)	2.0	0.08
so	pure soot	1.4	0.08
sa	NaCl	1.9	0.2
sb	NaCl	2.0	2.0
sc	NaCl	1.7	12
da	mineral dust	1.9	0.2
db	mineral dust	2.0	1.0
dc	mineral dust	1.7	12

Table 6.1: Overview of the modes and their chemical composition in COSMO-ART.

aerosol populations show a modal structure and therefore it can be described by a continuous size distribution as a function of the particle diameter.
The total number density N of an aerosol population can be described by following integral:

$$N = \int_0^\infty n\left(D_p\right) \mathrm{d}D_p \tag{6.1}$$

where $n(D_p)\ \mathrm{d}D_p$ describes the number density of particles with diameter D_p per m^{-3} air within the size range D_p and $(D_p + \mathrm{d}D_p)$. Because COSMO-ART describes several modes of aerosols this is applied to every single mode l (compare table 6.1).

The total size distribution of the aerosol particles is separated into several overlapping modes, depending on their size and chemical composition. Therefore every single mode can be described by a log-normal size distribution:

$$n_l(D_p) = \frac{1}{D_p} \frac{N_l}{\sqrt{2\pi} \ln \sigma_l} \exp\left(-\frac{\ln^2(D_p/D_{g,l})}{2\ln^2 \sigma_l}\right) \tag{6.2}$$

where N_l is the number concentration, σ_l the geometric standard deviation, and $D_{g,l}$ the median diameter of mode l. It is often preferred to use the logarithm of the diameter since the diameter can vary over several orders of magnitudes. This gives the following expression of the number distribution:

$$n_l(\ln D_p) = \frac{N_l}{\sqrt{2\pi} \ln \sigma_l} \exp\left(-\frac{\ln^2(D_p/D_{g,l})}{2\ln^2 \sigma_l}\right) \tag{6.3}$$

Following equation 6.3 the size distribution function and total number concentration of aerosols can calculated by:

$$\begin{aligned} n_N(D_p) &= \sum_l n_l(D_p), \\ N &= \sum_l N_l = \sum_l \int_0^\infty n_l(D_p)\, \mathrm{d}D_p \end{aligned} \tag{6.4}$$

To simulate the temporal evolution of $n_l(D_p)$ exactly it would be necessary to simulate the temporal evolution of N_l, σ_l, and $D_{g,l}$ but for some processes (advection, diffusion) the differential equations of σ_l and $D_{g,l}$ cannot be solved directly (Whitby and McMurry, 1997). Therefore the equations are formulated for integral moments of $n_l(D_p)$ where the k-th moment $M_{k,l}$ of the size distribution of each mode l is defined by:

$$M_{k,l} = \int_0^\infty D_p^k n_l(D_p)\, \mathrm{d}(D_p) \tag{6.5}$$

The moments are related to integral quantities of the aerosol population:

$$N_l = \int_0^\infty n_l\left(D_p\right) \mathrm{d}\left(D_p\right) \qquad = M_{0,l} \tag{6.6}$$

$$O_l = \pi \int_0^\infty D_p^2 n_l\left(D_p\right) \mathrm{d}\left(D_p\right) \qquad = \pi M_{2,l} \tag{6.7}$$

$$V_l = \frac{\pi}{6} \int_0^\infty D_p^3 n_l\left(D_p\right) \mathrm{d}\left(D_p\right) \qquad = \frac{\pi}{6} M_{3,l} \tag{6.8}$$

$$m_l = \frac{\pi}{6} \rho_p \int_0^\infty D_p^3 n_l\left(D_p\right) \mathrm{d}\left(D_p\right) \qquad = \frac{\pi}{6} \rho_p M_{3,l} \tag{6.9}$$

where O_l is the surface concentration, V_l the volume and m_l the mass concentration of mode l. To fully determine $n_l(D_p)$ all three moments of the log-normal distribution would be necessary to be known. But to achieve a numerically feasible solution of the resulting equation system σ_l is held constant. Therefore only two moments have to be calculated to derive $n_l(D_p)$. In COSMO-ART balance equations for N_l and m_l are calculated which are proportional to $M_{0,l}$ (Eq. 6.6) and $M_{3,l}$ (Eq. 6.9). Then for given N_l, m_l, and σ_l the mean diameter $D_{g,l}$ can be derived by:

$$D_{g,l} = \left(\frac{6 m_l}{\pi \rho_p \exp\left(4.5 \ln^2 \sigma_l\right) N_l} \right)^{1/3}, \tag{6.10}$$

and then finally compute $n_l(D_p)$ with equation 6.3.
The Reynolds-averaged balance equations are solved for N_l and m_l which are given by (Doms et al., 2011; Jacobson, 2005):

$$\frac{\partial}{\partial t} Y_l = \underbrace{-\nabla \cdot \left(\mathbf{v} Y_l\right)}_{\substack{\text{advection} \\ \text{(flux form)}}} + \underbrace{\nabla \mathbf{F}_{Y_l}}_{\text{turbulence}} + \underbrace{\frac{\partial}{\partial z}\left(\overline{w_l^{\text{sed}}} Y_l\right)}_{\substack{\text{gravitational} \\ \text{sedimentation}}} + \underbrace{S_{Y_l}}_{\substack{\text{microphysical} \\ \text{processes}}} \tag{6.11}$$

where Y_l is either the mass $Y = m$ or number $Y = N$ concentration for each mode l. The form of equation 6.11 is only applicable to the conservative flux-form advection scheme in COSMO (Runge-Kutta time integration with a Bott-advection scheme) which is

recommended for studies of aerosol-cloud interaction because of its mass conserving formulation. For other available advection schemes the balance equations have to be formulated in advection form for mass specific quantities (Bangert, 2012). Turbulent fluxes are parametrized according to the cloud hydrometeors in COSMO (Doms et al., 2011). Contribution of molecular diffusion is small and therefore neglected.
S_{Y_l} describes microphysical processes and is either a source or a sink for the corresponding mode l. Following processes take place for specific modes:

$$\begin{aligned} S_{N_l} &= S^{\text{nuc}}_{N_{l=if}} + S^{\text{coag}}_{N_l} + S^{\text{coag}^\circ}_{N_l} + S^{\text{conv}}_{N_l} + S^{\text{wash}}_{N_l} \\ S_{m_l} &= S^{\text{nuc}}_{m_{l=if}} + S^{\text{coag}}_{m_l} + S^{\text{cond}}_{m_l} + S^{\text{conv}}_{m_l} + S^{\text{wash}}_{m_l} \end{aligned} \tag{6.12}$$

with l = if, ic, jf, jc, c.

The modes sa, sb, sc, and da, db, dc do not interact with other modes and only the sea salt modes (sa, sb, sc) interact with the gas phase through condensation of sulfuric acid on the sea salt particles (Lundgren, 2010). Therefore it follows:

$$\begin{aligned} S_{N_l} &= S^{\text{conv}}_{N_l} + S^{\text{wash}}_{N_l}, \\ S_{m_l} &= S^{\text{cond}}_{m_l} + S^{\text{conv}}_{m_l} + S^{\text{wash}}_{m_l}, \end{aligned} \qquad \text{for } l = \text{sa, sb, sc} \tag{6.13}$$

and

$$\begin{aligned} S_{N_l} &= S^{\text{conv}}_{N_l} + S^{\text{wash}}_{N_l}, \\ S_{m_l} &= S^{\text{conv}}_{m_l} + S^{\text{wash}}_{m_l}. \end{aligned} \qquad \text{for } l = \text{da, db, dc} \tag{6.14}$$

The microphysical processes S_{Y_l} are:

$S^{\text{nuc}}_{Y_l}$	nucleation rates from the gas phase
$S^{\text{wash}}_{Y_l}$	rate of change due to scavenging below cloud
$S^{\text{coag}}_{Y_l}$	tendencies due to intermodal coagulation
$S^{\text{coag}^\circ}_{N_l}$	tendency due to intramodal coagulation
$S^{\text{cond}^\circ}_{m_l}$	condensation rate
$S^{\text{conv}^\circ}_{Y_l}$	tendency due to convective sub-grid scale transport

Emissions and deposition on the surface are boundary conditions of equation 6.11. A more detailed overview of the single processes and their description are given in Vogel et al. (2009)

6.1.1 Sea Salt Emissions

The parametrization of the sea salt emission flux was introduced by Lundgren (2006). Due to simplification the parametrization of sea salt production assumes that the freshly emitted sea salt contains only pure $NaCl$. The flux of sea salt particles into the lowest model layer is described as a function of sea surface temperature (SST) and horizontal wind velocity. Within the size range of 0.02 - 28 μm three parametrizations are used to describe the flux of sea salt particles (the flux is given in $m^{-2}s^{-1}$).

For particles with a dry diameter of 0.02 bis 1 μm (mode sa) the parametrization of Mårtensson et al. (2003) is used. In this case the flux is a function of horizontal wind velocity in 10m height (U_{10} in ms^{-1}) and SST:

$$\frac{dF_0}{d\log D_p} = \Phi\left(SST, D_p\right) 3,84 \cdot 10^{-6} U_{10}^{3,41} \tag{6.15}$$

where F_0 is the particle number flux. $\Phi\left(T_w, D_p\right)$ describes the particle flux per whitecap area and is depending on SST and dry particle diameter D_p (given in m):

$$\Phi\left(SST, D_p\right) = A_q\left(D_p\right) \cdot SST + B_q\left(D_p\right) \qquad q = 1, 2, 3 \tag{6.16}$$

The coefficients $A_q\left(D_p\right)$ and $B_q\left(D_p\right)$ are described in more detail in Mårtensson et al. (2003) and Lundgren (2006).

The emission flux for super micrometer sea salt particles in the size range of 1 - 9 μm D_p (mode sb) is parametrized by the function of Monahan et al. (1986)

$$\frac{dF_0}{dr_{80}} = 1,373 U_{10}^{3,41} r_{80}^{-3} \left(1 + 0,057 r_{80}^{1,05}\right) 10^{1,19 e^{-B^2}} \tag{6.17}$$

$$\text{where } B = \frac{0,380 - \log r_{80}}{0,650}$$

r_{80} refers to the wet radius of the aerosol with an ambient relative humidity of 80% and is given in μm.
Sea salt emissions in the range of 9-28 μm (sc) is described by the

work of Smith et al. (1993) in form of two log-normal distributions:

$$\frac{dF_0}{dr_{80}} = \sum_{x=1,2} C_x \exp\left(-f_x\left(\ln\frac{r_{80}}{r_x}\right)\right) \tag{6.18}$$

$$\text{where} \begin{cases} f_1 = 3,1\mu m, r_1 = 2,1\mu m, \log C_1 = 0,676U_{10} + 2,34 \\ f_2 = 3,3\mu m, r_2 = 9,2\mu m, \log C_2 = 0,959U_{10}^{0,5} - 1,475 \end{cases}$$

If the wet aerosol diameter is described as a function of the dry diameter the parametrizations 6.15 to 6.18 can be brought to the same form (Lewis and Schwartz, 2006). Then the flux of number concentration $F_{N,i}$ of each mode $i = sa, sb, sc$ is achieved by integration of the respective size intervall:

$$F_{N,i} = \int_{D_a}^{D_b} \frac{dF_0}{d\log D_p} d\log D_p = \lim_{n\to\infty} \sum_{i=1}^{n} \frac{dF_0}{d\log D_p} \Delta\log D_p \tag{6.19}$$

with the constant size step of $\Delta \log D_p = 0.1$. The flux of mass density $F_{m,i}$ is calculated from the number density flux for each of the three sea salt modes using following relation:

$$F_{m,i} = \frac{\pi\rho_p D_{gi,ini}^3}{6} \exp\left(4,5\ln^2\sigma_i\right) \cdot F_{N,i}. \tag{6.20}$$

where $D_{i,ini}$ and σ_i is given in table 6.1. The emissions of sea salt $E_{N,i}$ and $E_{m,i}$ enter the conservation equations for each mode via the lower boundary condition:

$$E_{N,i} = \frac{F_{N,i}}{\Delta z_s} \tag{6.21}$$

$$E_{m,i} = \frac{F_{m,i}}{\Delta z_s} \tag{6.22}$$

where Δz_s is the height of the lowest model domain (Lundgren, 2010).

6.1.2 Climate Engineering Sea Salt Emissions

Latham et al. (2008) made the suggestion to use sea water to produce sea-spray which then act as as extra available CCN for

marine stratocumulus clouds. Therefore an additional sea salt flux is introduced in case of the climate engineering (CE) simulations. The additional sea salt flux is added at every grid point over ocean water to achieve a high impact on cloud properties. This gives also the advantage to investigate the competition between the additional released particles and particles originating from anthropogenic sources.

The additional particle flux is based on the parametrized flux of Korhonen et al. (2010). In the work of Korhonen et al. (2010) the flux is a function of wind speed until a certain threshold is reached. At wind speeds higher than the threshold the flux is set constant.

In this work although the flux is set constant at all time and nearly as high as the constant flux of Korhonen et al. (2010). This simulates that the spraying ships would be always able to spray everywhere the same amount of particles to investigate the maximum impacts of CE emissions. This includes the investigation of areas with low natural sea salt concentrations.

The CE emissions are added to the natural sea salt emissions. Subsequently the sea spray originating from the CE emissions will be treated like natural sea salt and undergoes the same processes.

Three different CE scenarios are conducted. In the first small particles are seeded. Hence the CE flux is added to the smallest sea salt mode *sa* (see chapter 6.1.1). In the second scenario the CE flux is added on the second, but larger, sea salt mode *sb*. This scenario gives further insights to the importance of the size of the seeded particles. A third scenario simulates the impact of seeding with smaller and larger particles together. Therefore the flux is splitted into a flux on the sea salt mode *sa* and *sb* with a weighting of 50% each. This simulates the case that is is technically not possible to achieve seeding with only small particles. For each scenario the efficiency of CE is evaluated in chapter 9.

To calculate the flux of the CE emissions the number density flux $F_{N,CE}$ is calculated by:

$$F_{N,CE} = 5.4 \cdot 10^4 6^{1,5} \quad [\mathrm{m}^{-2}\mathrm{s}^{-1}] \tag{6.23}$$

The flux of mass density $F_{m,CE}$ is calculated analogous to equation 6.20 with:

$$F_{m,CE} = \frac{\pi \rho_p D_{gi,ini}^3}{6} \exp\left(4,5 \ln^2 \sigma_i\right) \cdot F_{N,CE} \tag{6.24}$$

Where $D_{gi,ini}^3$ depends on the chosen CE scenario and the inital diameter of the seeded mode.

The CE emissions $E_{N,CE}$ and $E_{m,CE}$ enter the conservation equations via the lower boundary condition:

$$E_{N,CE} = \frac{F_{N,CE}}{\Delta z_s} \tag{6.25}$$

$$E_{m,CE} = \frac{F_{m,CE}}{\Delta z_s} \tag{6.26}$$

Note that Latham et al. (2008) suggested the release of monodisperse particles. COSMO-ART however uses a modal approach for aerosol particles and therefore the CE particles aren't monodisperse. This is justified due to the fact that latest after the release of the particles coagulation will take place and they will change their size distribution.

In this work stratocumulus clouds in the marine boundary layer (MBL) are targeted for seeding. They typically occur in the lowest 1.5 km of the troposphere. While the marine boundary layer is well mixed it is not necessary for the particle plume to be buoyant, as neutral buoyancy will result in mixing until temperature inversion is reached. The timescale is estimated to be 1 to 3 hours (Lu and Seinfeld, 2006).

6.2 Cloud Microphysics

Cloud microphysical processes in operational use of COSMO are represented by a one-moment bulk scheme which describes hydrometeor classes following a traditional grouping (Houze Jr, 2014) (cloud droplets, rain drops, cloud ice, graupel, snow) by only calculating one moment namely mass mixing ratio and keeping number concentration fixed.

To simulate aerosol cloud interaction only calculating one moment is not sufficient enough. At least two moments have to be calculated which means in this case including information of cloud droplet number concentration. Therefore the two-moment scheme

of Seifert and Beheng (2006) is used for COSMO. This also means that additionally the budget equation of the number concentration has to be solved which is given by following expression:

$$\frac{\partial N_c}{\partial t} = -\nabla \cdot (\mathbf{v} N_c) + \nabla \cdot \mathbf{F} N_c + S_{N_c} \tag{6.27}$$

while the microphysical processes S_{N_c} include:

$S_{N_c}^{\mathrm{act}}$ Activation of CCN to cloud droplets

$S_{N_c}^{\mathrm{ac}}$ Self-collection of cloud droplets

$S_{N_c}^{\mathrm{acc}}$ Accretion of cloud droplets by raindrops

$S_{N_c}^{\mathrm{melt}}$ Melting of ice crystals

$S_{N_c}^{\mathrm{freez}}$ Freezing of cloud droplets

$S_{N_c}^{\mathrm{rim}}$ Collection of cloud water by snow (riming)

$S_{N_c}^{\mathrm{shed}}$ Collection of cloud water by wet snow to form rain (shedding)

Although the investigated clouds within this thesis are warm-phase clouds and the first three processes are dominating the processes in warm-phase clouds the last four processes are listed for completeness.

The size distribution assumed for the cloud droplets is a Gamma function. The autoconversion, accretion and selfcollection is calculated according to the parametrization of Seifert and Beheng (2001) and is a function of the varying cloud droplet size distribution. The autoconversion rate for example is inversely proportional to N_c and the parametrization, which relies on the solution of a stochastic collection equation, is validated against simulations using a spectral bin model (Seifert et al., 2006).

If the two-moment scheme is used in COSMO the calculation of the cloud droplet number concentration is defined by different prescribed aerosol scenarios. The scenarios range from a maritime case to a polluted continental case (100 cm^{-3} to 3200 cm^{-3} CCN) but all the scenarios unite the disadvantage that aerosol concentration is constant over the whole domain and time. This may be reasonable for sensitivity studies within very small domains or to investigate single cases but in cases with high aerosol variability this scenario approach has its limitations.

COSMO-ART brings the advantage to use prognostic aerosols instead of prescribed scenarios. This is obvious in regions with very sharp gradients of aerosol concentration, where neither a clean maritime nor polluted continental scenario is prevailing. Then aerosol activation is calculated like it is described in chapter 6.3.1.

6.3 Aerosol Cloud Interaction

6.3.1 Aerosol Activation

Depending on their chemical properties, atmospheric aerosol particles can act as cloud condensation nuclei (CCN) during cloud formation. Therefore, they determine the initial size distribution of cloud droplets (Twomey, 1959) and as a consequence, aerosol particles influence optical properties and microphysical processes of clouds.

Therefore the calculation of available CCN is based on the classical Köhler theory (Köhler, 1936b). For the representation of the internal chemical mixture of the particles the approach of Hänel (1976) is used. Since COSMO-ART uses a lognormal distribution for aerosol representation the parameterization of Fountoukis and Nenes (2005) for cloud droplet formation is used. The principle path of the parametrization is shortly described in the following. First the CCN concentration is calculated as function of supersaturation ("CCN spectrum") using the Köhler theory. Then the CCN spectrum is included within the dynamical framework of an adiabatic parcel with a constant updraft velocity (or cooling rate) to compute the maximum supersaturation s_{max} achieved during the cloud parcel ascent (Nenes and Seinfeld, 2003; Fountoukis and Nenes, 2005). An ideal solutions is assumed, since non-ideal behaviour of solution droplets depends on droplet size. If the chemical composition of an aerosol mode does not vary with size then the aerosol distribution $\mathrm{n}(D_P)$ can be mapped to supersaturation space and critical supersaturation distribution $n^s(s)$ and it yields:

$$n^s(s) = \frac{\mathrm{d}N}{\mathrm{d}s} = -\frac{\mathrm{N}}{\mathrm{d}\ln D_P}\frac{\mathrm{d}\ln D_p}{\mathrm{d}s}. \tag{6.28}$$

The critical supersaturation of a particle with the diameter D_p is calculated by:

$$s_c = \frac{2}{\sqrt{B}} \left(\frac{A}{3D_p} \right)^{3/2} \tag{6.29}$$

where $A = \frac{4\sigma M_w}{\rho_w}$ and $B = \frac{\nu \rho_s M_w}{\rho_w M_s}$, σ is the surface tension, ρ_w is the density of water and M_w is the water molecular weight, ρ_s is the solute density, M_s the solute molecular weight, ν the number of ions resulting from the dissociation of one solute molecule.

With equation 6.29 it follows:

$$\frac{\mathrm{d} \ln D_p}{\mathrm{d}s} = -\frac{2}{3s} \tag{6.30}$$

and

$$\frac{D_p}{D_g} = \left(\frac{s_g}{s} \right)^{2/3}. \tag{6.31}$$

With this and the formula of a lognormal distribution we can retrieve the critical supersaturation distribution:

$$n^s(s) = \sum_{i=1}^{l} \frac{2N_i}{3s\sqrt{2\pi} \ln \sigma_i} \exp \left[-\frac{\ln^2 \left(s_{g,i}/s \right)^{2/3}}{2 \ln^2 \sigma_i} \right], \tag{6.32}$$

where $s_{g,i}$ is the critical supersaturation of a particle with the diameter $D_{g,i}$.

From 6.32 the CCN spectrum (concentration of particles with $s_c \leq s$) can derived by:

$$CCN(s) = \int_0^s n^s(s)\, \mathrm{d}s = \sum_{i=1}^{l} \frac{N_i}{2} erfc \left[\frac{2 \ln \left(s_{g,i}/s \right)}{3\sqrt{2} \ln \sigma_i} \right]. \tag{6.33}$$

If the maximum supersaturation s_{max} is known then the activated cloud droplet number N_c^* can calculated from equation 6.33, which yields

$$N_c^* = CCN(s_{max}). \tag{6.34}$$

Now the maximum supersaturation has to be calculated. This is achieved by assuming an adiabatically rising air parcel. The rate

of change of the supersaturation s for a cloud parcel ascending with a constant updraft velocity w is (Seinfeld and Pandis, 2006; Pruppacher and Klett, 1997):

$$\frac{\mathrm{d}s}{\mathrm{d}t} = \alpha w - \gamma \frac{\mathrm{d}x_c}{\mathrm{d}t}, \tag{6.35}$$

where

$$\alpha = \frac{gM_w\Delta H_v}{c_p RT^2} - \frac{gM_a}{RT}, \quad \gamma = \frac{pM_a}{p^s M_w} - \frac{M_w \Delta H_v^2}{c_p RT^2} \tag{6.36}$$

and where ΔH_v is the latent heat condensation of water, T is the parcels temperature, M_w is the molecular weight of water and M_a the molecular weight of air, g is the acceleration due to gravity, c_p is the capacity of air, p^s is the water saturation vapour pressure, p the ambient pressure and R the universal gas constant.

The first term on the right hand side of equation 6.35 expresses the tendency of the ascending parcel to increase supersaturation due to adiabatic cooling. While in the second term $\frac{\mathrm{d}x_c}{\mathrm{d}t}$ is the rate of condensation of liquid water onto the activated droplets and expresses the tendency of supersaturation to be decreased by depletion of water vapour onto activated cloud droplets.

Maximum supersaturation s_{max} is reached when both terms are equaling each other. While the first term in equation 6.35 can be calculated with the updraught velocity within the model, the second term has to be parameterized. For the second term the parameterization of Nenes and Seinfeld (2003) is used and the work of Nenes and Seinfeld (2003) is referred for further detail.

6.3.2 Activation Rate

The activation rate, which depends on maximum supersaturation that occurs during formation of cloud droplets, is the main challenge linking aerosol particles with clouds in a three dimensional model. The parametrization of Fountoukis and Nenes (2005) is used within COSMO-ART to describe the activation of aerosol particles including the Giant CCN correction of Barahona et al. (2010). The maximum supersaturation with respect to water and consequently the number of activated particles is calculated based on an ascending air parcel framework and Koehler theory as a

function of aerosol properties and updraft velocity. To take into account size-dependent growth kinetics an average modified diffusivity for water vapour is used (Fountoukis and Nenes, 2005).
To derive a nucleation rate of cloud droplets $S_{N_c}^{act}$ several assumptions are made. For the nucleation rate of cloud droplets three different cases are defined for which nucleation of cloud droplets can occur. For a newly formed cloud (or if cloud droplet number is below $10\,\mathrm{cm}^{-3}$) as well as for in-cloud activation of aerosol particles above the cloud base the parametrization is directly applied and the nucleation rate of cloud droplets is given by

$$S_{N_c}^{act} = \max\left(\left[N_c^* - N_c\right]/\Delta t, 0\right) \quad \text{(new cloud and in-cloud case)} \tag{6.37}$$

where Δt is the time step and N_c is the cloud droplet number concentration before droplet nucleation. N_c^* is given by equation 6.34. In case of in-cloud activation the growth of the existing cloud droplets can be considered in the parametrization of s_{max} using the extension of Barahona et al. (2010) for the growth of large inertially-limited aerosol particles. One should note that aerosol particles that have been activated at the cloud base are considered in the calculation of the in-cloud activation. This can potentially cause an overestimation of the number of activated droplets inside the cloud, especially for low aerosol number concentrations. Nevertheless, in-cloud activation is accounted for to avoid unrealistic low N_c in case of convective cloud systems with strong updrafts inside the clouds (Bangert, 2012).
In case of an already existing cloud the nucleation rate of droplets at the cloud base is calculated on the basis of advection and turbulent diffusion of particles into the cloud base.

$$S_{N_c}^{act} = -\frac{\partial}{\partial z} N_c^*\left(s_{max}\right) w + \frac{\partial}{\partial z} K \frac{\partial}{\partial z} N_c^*\left(s_{max}\right) \quad \text{(cloud base case)} \tag{6.38}$$

where K is the turbulent diffusion coefficient (Bangert et al., 2011, 2012). For all cases the maximum number concentration of cloud droplets after nucleation is restricted by total number concentration of aerosol particles.

6.3.3 Subgridscale Updraft Velocity

In contrast to global models, mesoscale models (resolution between 2 km and 20 km) are capable to simulate location and characteristics of larger individual cloud systems. Hence, the updraft velocities during cloud formation cannot reproduced quantitatively by the simulated grid-scale vertical velocity w. This will cause a strong underestimation of updraft velocity in the model, which will lead to an underprediction of supersaturation, which will result in an underestimation of cloud droplet number concentrations (CDNC).

Sub-grid scale vertical velocities, w', are described with a Gaussian probability distribution function, $P_w(w')$ following (Morales and Nenes, 2010):

$$P_w\left(w'\right) = \frac{1}{\sqrt{2\pi}\sigma_w} \tag{6.39}$$

The mean of $P_w(w')$ is set equal to the grid scale updraft, w, and the standard deviation, σ_w, is calculated as the square root of the turbulent kinetic energy TKE. A weighted mean of the activated particles, N_c^*, is calculated by numerically solving the integral

$$N_c^* = \frac{\int_0^\infty N_c^*\left[s_{max}\left(w'\right)\right] P_w\left(w'\right) \mathrm{d}w'}{\int_0^\infty P_w\left(w'\right) \mathrm{d}w'} \tag{6.40}$$

6.4 Convection Parameterization

Cumulus convection has a major impact on the vertical structure and redistribution of temperature, moisture, and aerosol fields of the atmosphere and therefore cannot be neglected. Since those processes take place on horizontal scales which are much smaller than the grid size of large-scale models (for example GCMs) and the grid size of mesoscale models (NWP) cumulus convection has to be parametrized.

The parametrization has to take several aspects of convection into account like diabatic heating due to the release of latent heat originating from cloud condensation and from formation and evaporation of precipitation. Also vertical transports of heat, moisture and momentum in cumulus updraughts and downdraughts has to be taken into account, as well as regions with compensat-

ing downward motions, which interact with the cumulus clouds by lateral exchange due to entrainment and detrainment. All these processes tend to stabilize the original unstable stratification. Arakawa (2004) for example gives a short overview of cumulus parametrizations. For application in COSMO the mass flux based parametrization of Tiedtke (1989) is used.

6.4.1 Shallow Convection

The parametrization of Tiedtke (1989) treats three different types of convection occurring in a single grid cell, namely deep convection, shallow convection and midlevel convection. All of them are treated the same way except of their closure assumptions. Because the clouds (stratocumulus clouds) which are topic of this work originate from shallow convection, only the part of shallow convection will be described more detailed.

With coarser resolutions (grid spacing $> 7\,\mathrm{km}$) the Tiedtke scheme is used considering all types of convection (deep, shallow, midlevel). If COSMO is used with higher resolutions, like a grid spacing of 2.8 km, it is assumed that the deep convection is explicitly resolved. However small-scale shallow convection is assumed that it still has to be parametrized. Shallow convection is important for the transport of heat and moisture by nonlocal fluxes. In principle this clouds could be treated by a planet boundary layer (PBL) scheme (Siebesma et al., 2007) but such a PBL scheme is not yet available for COSMO.

To overcome this problem a simple mass-flux scheme which is based on the Tiedtke-Scheme (Tiedtke, 1989) is used. The original scheme distinguish between three types of convection: deep, midlevel and shallow. Since the original Tiedtke scheme includes shallow convection it is easy to extract this part and use it for shallow convection alone. For example a threshold for the cloud depth has to be defined which is set arbitrarily to $\Delta p = 250\,\mathrm{hPa}$ within the parametrization. Although Baldauf et al. (2011) stated that in certain conditions a parametrization of shallow convection is necessary to avoid an overprediction of boundary layer clouds over Germany, it can be shown later that this is not valid for the case investigated in this work.

As already mentioned the cumulus parametrization according to Tiedtke (1989) is based on a mass-flux approach and the feedbacks

of subgrid scale cumulus convection like vertical fluxes of mass, heat, moisture and momentum in up- and downdraughts are calculated by using a simple bulk cloud model.

The prognostic equations for the grid-scale variables are obtained by averaging the microturbulent equations for heat, moisture and momentum over the spatial scales which correspond to the model grid spacing. By Neglecting nonhydrostatic effects on the mesoscale as well as changes in the mean vertical velocity, the thermodynamic forcing due to moist convection (MC) can be formulated by the following tendencies, which can be denoted by M_Ψ^{MC} and are then added to the grid scale model equations:

$$\begin{aligned} c_{pd} M_T^{MC} = \left(\frac{\partial s}{\partial t}\right)_{MC} &= -\frac{1}{\rho}\frac{\partial}{\partial z}\left[M_u\left(s_u - s\right) + M_d\left(s_d - s\right)\right] \\ &\quad + L\left(c_u - e_d - e_l - e_p\right) \\ M_{q_v}^{MC} = \left(\frac{\partial q_v}{\partial t}\right)_{MC} &= -\frac{1}{\rho}\frac{\partial}{\partial z}\left[M_u\left(q_{v,u} - q_v\right) + M_d\left(q_{v,d} - q_v\right)\right] \\ &\quad - \left(c_u - e_d - e_l - e_p\right) \\ M_\alpha^{MC} = \left(\frac{\partial \alpha}{\partial t}\right)_{MC} &= -\frac{1}{\rho}\frac{\partial}{\partial z}\left[M_u\left(\alpha_u - \alpha\right) + M_d\left(\alpha_d - \alpha\right)\right] \end{aligned} \tag{6.41}$$

where $s = c_{pd}T + gz$ is the dry static energy, α denotes the horizontal wind components(u or v). The subscripts u and d indicate if the variable is part of the up- or downdraught.

A crucial point of this parametrization is the assumption that horizontal averaging is large enough to contain a whole ensemble of clouds. Which on the other side means that the area covered by up- and downdraughts is considerable smaller than the models grid box. Furthermore the convective scale eddy transport of dry static energy, moisture and momentum and the cumulus-induced subsidence in the environmental air are not described in terms of a contribution of every single ensemble member, but represented as an average of their values by using a one-dimensional bulk cloud model after Yanai et al. (1973). This means that the net effects of an ensemble of clouds is represented by a representative single cloud.

The parametrization underlies the assumption that area fraction of up- and downdraught is very small compared to the grid box so

that values of environmental variables can be approximated by the area mean values. In equation 6.41 following symbols are used:

M_u	updraught mass flux, defined by $M_u = \rho a_u(w_u - w)$
a_u	area of the updraught
w_u	vertical velocity in the updraught
M_d	downdraught mass flux, defined by $M_d = \rho a_d(w_d - w)$
a_d	area of the downdraught
w_d	vertical velocity in the downdraught
s_u, s_d	dry static energy in the up- and downdraught
q_u, q_d	specific humidity in the up- and downdraught
α_u, α_d	horizontal wind components in the up- and downdraught
c_u	condensation in the updraught (area mean)
e_d	evaporation of the precipitation in the downdraught (area mean)
e_l	evaporation of cloud water in the environment (area mean)
e_P	evaporation of precipitation below cloud base (area mean)
L	latent heat with $L = L_v$ (heat of evaporation) for $T \geq 0°C$ and $L = L_S$ (heat of sublimation) for $T < 0°C$

For rain water formed in the convective cloud column equilibrium is assumed. The budget equation for the area mean value of the flux of convective precipitation (denoted as P) then reads

$$\frac{\partial P}{\partial z} = -\rho \left(g_P - e_d - e_P \right) \tag{6.42}$$

where g_P denotes the conversation rate of cloud water to rain water (more in Section 6.4.4). The precipitation rate at ground is the integral of 6.42.

6.4.2 The Cloud Model

To compute the convective tendencies in equation 6.41 a simple 1D cloud model is used, where it is assumed that the updraught in the cloud ensemble is in steady state. For the ascending air the budget equations of mass, heat, moisture and momentum are

$$\begin{aligned}
\frac{\partial M_u}{\partial z} &= E_u - D_u \\
\frac{\partial}{\partial z}\left(M_u s_u\right) &= E_u s - D_u s_u + L\rho c_u \\
\frac{\partial}{\partial z}\left(M_u q_{v,u}\right) &= E_u q_v - D_u q_{v,u} - \rho c_u \\
\frac{\partial}{\partial z}\left(M_u q_{c,u}\right) &= -D_u q_{c,u} + \rho\left(c_u - g_P\right) \\
\frac{\partial}{\partial z}\left(M_u \alpha_u\right) &= E_u \alpha - D_u \alpha_u
\end{aligned} \tag{6.43}$$

where $q_{c,u}$ is the cloud water content in the updraught. A similar set of equations is applied to the quantities of the downdraught, where it is assumed that downdraught region is at saturation (maintained by evaporation of rainwater) and contains no cloud water:

$$\begin{aligned}
\frac{\partial M_d}{\partial z} &= E_d - D_d \\
\frac{\partial}{\partial z}\left(M_d s_d\right) &= E_d s - D_d s_d - L\rho e_d \\
\frac{\partial}{\partial z}\left(M_d q_{v,d}\right) &= E_d q_v - D_d q_{v,d} - \rho e_d \\
\frac{\partial}{\partial z}\left(M_d \alpha_d\right) &= E_d \alpha - D_d \alpha_d
\end{aligned} \tag{6.44}$$

The vertical integration of 6.43 from cloud base to cloud top and of 6.44 from top of the downdraughts to the surface yields the values of the variables within the up- and downdraught to calculate the convective tendencies. To perform the integration following issues have to be specified:

- the mass flux M_u and the values of $s_u, q_{v,u}, q_{c,u}$ and α_u at the cloud base as lower boundary condition

- the mass flux M_d and the values of $s_d, q_{v,d}$ and α_d at the top of the downdraughts as upper boundary condition

- the detrainment rates E_u and E_d as well as the detrainment rates D_u and D_d of up- and downdraughts as functions of available grid-space model parameters and

- a parametrization for microphysical processes

Since only the first three points can be assumed in the nearer sense as closure conditions (direct connection of cumulus convection to grid-scale forcing) they will be discussed in Section 6.4.3. Although the microphysical processes are more specific to the cloud model it is a parametrization within the parametrization and will be shortly discussed in Section 6.4.4.

6.4.3 Closure Assumptions

The Tiedtke scheme discriminates three types of convection:

- penetrative convection

- shallow convection

- midlevel convection

All of these are treated by different closure hypotheses and only one type of convection is allowed to be present at a grid point at a time step, which means that layered convection (midlevel above shallow convection) is not described by this scheme.

Shallow and penetrative convection originates from atmospheric boundary layer, but differ in their vertical extend (defined by vertical extend of the unstable stratification). Penetrative convection often forms in regions with large-scale convergence in lower troposphere, while shallow convection may also be formed in case of slightly divergent flow. The latter is often driven by evaporation from the ground or water surface.

Midlevel convection however is originated at levels within the free troposphere. Convective cells of this type often occur in rainbands at warm fronts or in the warm sector of extratropical cyclones. They are probably formed by dynamically forced lifting low-level air until it becomes saturated at the level of free convection. Often

a low-level temperature inversion exists which inhibits convection to be initiated freely from the surface layer.

Depending on the presence of a specific type of convection different closure hypotheses are applied. As already mentioned the closure assumption for midlevel convection is neglected.

a) **Updraught mass flux at cloud base**
In case of shallow convection, an equilibrium type of closure is applied by imposing a moisture balance for the subcloud layer such that the vertically integrated specific humidity is maintained in the presence of grid-scale, turbulent and convective transport (Kuo-type-closure). Using the source term $M_{q_v}^{MC}$ from 6.41 in the budget equation of the specific humidity q_v, this balance is formulated by

$$\begin{aligned}&\left[M_u\ (q_{v,u} - q_v) + M_d\,(q_{v,d} - q_v)\right]_{zb} = \\ &\quad -\int_{z_s}^{z_b} \left(\rho \mathbf{v} \cdot \nabla q_v + \frac{\partial F^{q_v}}{\partial z}\right) \mathrm{d}z, \end{aligned} \tag{6.45}$$

where z_s is the terrain height, z_b is the height of the cloud base. Convection will only occur when the right hand side if equation 6.45 is positive, i.e. when moisture convergence tends to increase the subcloud moisture content.

In case of penetrative convection it is supposed that the advective forcing is the major contributor to the moisture convergence. The closure condition 6.45 is well justified over tropical oceans where the boundary layer moisture content usually changes little over time during convective activity, but little is known on how well it holds for other areas. The quasi-steady moisture balance is also applied for shallow convection. The difference is that the moisture supply to cumulus clouds is now largely through vertical turbulent transports driven by surface evaporation whereas the contribution of grid-scale advection transports are either small or even negative.

b) **Downdraught mass flux at the level of free sinking**
Precipitation from deep convective cells is usually associated with downdraughts initiated due to water loading and evaporative cooling during the clouds life cycle. In the scheme

downdraughts are considered to originate from cloud air influenced by the mixing with environmental air at the level of free sinking (LFS). The LFS is assumed to be the highest model layer where a mixture of equal parts of cloud air and saturated environmental air at wet-bulb temperature becomes negative buoyant with respect to the environment. This procedure defines also the boundary values of $s_d, q_{v,d}$ and α_d at the top of the downdraughts. The downdraught mass flux at z_{LFS}, the height of free sinking, is assumed to be directly proportional to the updraught mass flux at cloud base. That is,

$$(M_d)_{z_{LFS}} = \gamma_d \, (M_u)_{z_b} \tag{6.46}$$

The coefficient γ_d is a tunable parameter which determines the intensity of the downdraughts. In the present model version: $\gamma_d = 0.3$.

c) **Specification of entrainment and detrainment**
Lateral transport across cloud boundaries is represented by entrainment and detrainment. For the updraught, entrainment is just assumed to occur via turbulent exchange of mass (turbulent entrainment E_u^T) and through organized inflow associated with large-scale convergence (dynamic entrainment E_u^D). Detrainment concerning the updraught is assumed to have contributions from turbulent mixing (turbulent detrainment D_u^T) and from organized outflow at the top of the cloud (dynamic detrainment D_u^D). For the downdraught only turbulent entrainment and detrainment (E_d^T, D_d^T) is considered:

$$\begin{aligned} E_u &= E_u^T + E_u^D, \\ D_u &= D_u^T + D_u^D, \\ E_d &= E_d^T, \\ D_d &= D_d^T. \end{aligned} \tag{6.47}$$

The lateral turbulent mixing terms are parametrized the following way:

$$\begin{aligned} E_u^T &= \epsilon_u M_u, \\ D_u^T &= \delta_u M_u, \\ E_d^T &= \epsilon_d |M_d|, \\ D_d^T &= \delta_d |M_d|. \end{aligned} \tag{6.48}$$

where $\epsilon_u = \delta_u$ and $\epsilon_d = \delta_d$ is assumed for the entrainment/detrainment parameters to ensure that there is no vertical change of updraught mass flux due to turbulent mixing processes. The fractional entrainment rate for shallow convection is set to $\epsilon_u = 3.0 \cdot 10^{-4}\,\mathrm{m}^{-1}$. Dynamic entrainment is neglected for shallow convection.

Dynamic detrainment usually occurs in the upper regions of cumulus clouds, where the rising air loses its buoyancy relative to environmental air which results in a deceleration of the updraught vertical velocity and a corresponding organized lateral outflow. The scheme parametrize roughly the effect of overshooting cumuli by assuming that only a fraction $(1-b_u)$ of the updraught mass flux is made available for lateral outflow in the layer k_T that contains the level of zero-buoyancy. The remaining fraction b_u is allowed to penetrate into the stable layer above $(k_T - 1)$ and to detrain there:

$$D_u^D = \begin{cases} (1-b_u)_{k+1/2} \,/ \Delta z_k & \text{if } k = k_T, \\ b_u \,(M_u)_{k+1/2} & \text{if } k = k_T - 1 \\ 0.0 & \text{else.} \end{cases} \tag{6.49}$$

This formulation is applied for all types of convective clouds, where b_u is a tunable parameter which is set to 0.33. Because 6.49 is formulated in the computational space (and originally for quite coarse vertical resolution of the ECMWF global model) care has to be taken in case of increasing vertical resolution. Sensitivity tests show that this is a crucial parameter in determining total grid scale cloud water content, which is briefly shown in chapter 7.

d) **Temperature and humidity parameters at cloud base**
In order to integrate the updraught equations 6.43 using the

above closure assumptions, the variables T, q_v, q_c and α at cloud base must be specified as lower boundary conditions.

First it is checked if shallow convection can occur at a grid point. At the first model level above the surface ($k = N_\zeta$) an air parcel is defined with grid-scale values of temperature (plus a small excess value), specific humidity and horizontal momentum. By lifting the parcel adiabatically the condensation level at $k = k_B$ is computed while this level defines cloud base (level of free convection, where parcel becomes buoyant with respect to environment). The parcels values of T, q_v, q_c and α at cloud base $k = N_B$ are then used as boundary conditions to integrate the updraught equations.

6.4.4 Microphysical Processes

Below a brief summary of the microphysical processes of the 1D cloud model is given.

a) **Condensation/deposition within the updraught**
The calculation of the condensed water in the ascending air underlies a simple saturation adjustment. Whenever supersaturation is reached the specific humidity $q_{v,u}$ is set back to saturation value and the difference is interpreted as condensed cloud water. The release of latent heat is taken into account and if temperature is below freezing point, saturation over ice is assumed to diagnose the deposition rate.

b) **Formation of precipitation within the updraught**
Normally a simple parametrization is used to calculate the conversion of cloud water to rain water. But in case of shallow convection the formation of "convective" drizzle is suppressed. On the other side in the investigated region of this work the formation of rain/drizzle would anyway be foiled because in the parametrization the formation of rain is a function of height. In COSMO the default height for rain formation over water is set to 1500 m above water within the parametrization. In case of shallow stratocumulus clouds this is quite questionable because boundary layer height may be well below this value and marine stratocumulus clouds can produce some amount of drizzle.

$\Delta z_c = 1500\,\mathrm{m}$ over water and $\Delta z_c = 3000\,\mathrm{m}$ over land.

c) **Evaporation of precipitation in the downdraught**
In case of shallow convection there is no precipitation which can evaporate, since no precipitation is formed.

d) **Evaporation of cloud water in the environment**
Cloud water which has been detrained into subsaturated environment is assumed to evaporate immediately:

$$e_l = \frac{1}{\rho} D_u q_{c,u} \tag{6.50}$$

e) **Evaporation of precipitation below cloud base**
In case of shallow convection there is no precipitation which can evaporate, since no precipitation is formed.

Adjustments for Shallow Convection Scheme in case of stratocumulus Clouds

The assumption of the entrainment and detrainment rates (ϵ and δ) which are shown in chapter 6.4.3 may be a good assumption for deep convection, but Siebesma and Holtslag (1996) could show with LES simulations that the rates differ by a factor of 10 for shallow stratocumulus clouds from those defined originally in the parametrization and used as default values in COSMO. The values for ϵ and δ found by Siebesma and Holtslag (1996) are:

$$\begin{aligned} \delta &\approx 1.5 \sim 2.5(\cdot 10^{-3}) m^{-1} \\ \epsilon &\approx 2.5 \sim 3(\cdot 10^{-3}) m^{-1} \end{aligned} \tag{6.51}$$

The spread in equation 6.51 is a result of variations of the rates with height. The behaviour of the parametrization with the default values (compare chapter 6.4.3) can be described as a nonleaking funnel with massive detrainment at the cloud top. On the other side the use of the values of equation 6.51 gives the scheme the possibility to enhance lateral mixing and less massive detrainment at the cloud top (Siebesma and Holtslag, 1996). Although the LES simulations of Siebesma and Holtslag (1996) was conducted for a special type of cloud (marine stratocumulus clouds) the shallow convection scheme in its original state assumes the same

entrainment and detrainment rates as for deep convection. This is questionable as the LES study could show.

6.4.5 Convective Cloud Cover

Since convective clouds are an important factor in the radiation budget the cloud cover from convectional processes have to be taken into account in the radiation scheme of COSMO. Therefore a convective cloud cover in a grid cell with parametrized convection has to be calculated.

If a convective grid cell is detected the cloud base z_{base} and the cloud top z_{top} are calculated. Afterwards the convective cloud cover is calculated by:

$$CC_{conv} = 0.35 \cdot (z_{top} - z_{base}) / 5000 \tag{6.52}$$

where z_{top} and z_{base} are given in metre. In case of an anvil the cloud cover is doubled in this layer. Convectional cloud cover has a minimal value of 0.05 and a maximum value of 1. This is further used for cloud optical properties as it is discussed in chapter 6.6

6.5 Radiation Scheme

Radiative fluxes of the atmosphere are calculated with the radiation scheme GRAALS (Ritter and Geleyn, 1992). This scheme is based on the δ-two-stream version of the radiative transfer equations which incorporates the effects of scattering, absorption and emission by cloud droplets, aerosols and gases for eight spectral bands k_b (table 6.2).

Table 6.2: Spectral bands of GRAALS in μm.

spectral range	spectral band k_b	wave length [μm]
solar	1	1.53 - 4.64
	2	0.70 - 1.53
	3	0.25 - 0.70
thermal	4	20.0 - 104.5
	5	12.5 - 20.0
	6	8.33 - 9.01 10.31 - 12.5
	7	9.01 - 10.31
	8	4.64 - 8.33

GRAALS can be used with a spatial climatology of aerosols and their optical properties. But within COSMO-ART it is possible to use the prognostic aerosol to include an online coupled aerosol radiation interaction. Optical properties of aerosols are parametrized as a function of aerosol size distribution and chemical composition. To save computational time detailed Mie calculation were performed a priori and the results are used to compute optical properties from prognostic aerosol (Stanelle et al., 2010; Lundgren, 2010).

A flexible treatment of clouds is achieved by allowing partial cloud cover in each model layer and relating the cloud optical properties to cloud liquid water content, which is only used for the standard one moment microphysics cloud scheme of COSMO-ART. In case of the two moment scheme the additional information of number concentration is used to calculate optical properties which then includes the impact of varying cloud size distribution (see chapter 6.6).

6.6 Cloud Optical Properties

6.6.1 Grid Scale Clouds

The cloud optical thickness τ_c depends on the size of the droplets and the liquid water content (Sect. 4.2.2). To simulate the impact of aerosol particles on cloud optical properties changes in droplet size distribution has to be accounted for in the radiation scheme. To calculate radiative transfers with GRAALS the extinction coefficient $\beta_{ext,c}$, the single-scattering albedo ω_c and the asymmetry factor g_c of the clouds has to be calculated (Sect. 6.5).

The extinction coefficient with restriction to the range of visible light is given by Eq. 4.23 as a function of liquid water content LWC and the effective radii r_{eff} of the cloud droplet distribution. With a given droplet size distribution optical parameters like extinction coefficient, single-scattering albedo and asymmetry factors can be determined by Mie theory (Mie solution for spherical particles). However, a calculation of the Mie solution within a three dimensional atmospheric model would be too time consuming.

Therefore the parametrization of Hu and Stamnes (1993) is used to calculate the optical properties of liquid clouds as a function of r_{eff}:

$$\beta_{ext,c} = LWC(a_1 r_{eff}^{b_1} + c_1), \tag{6.53}$$

$$\omega_c = 1 - (a_2 r_{eff}^{b_2} + c_2), \tag{6.54}$$

$$g_c = a_3 r_{eff}^{b_2} + c_3, \tag{6.55}$$

where LWC is the liquid water content of the cloud and a_i, b_i and c_i $(i = 1, 2, 3)$ are fitting constants for a given wavelength derived by Mie calculations. These constants are given in (Hu and Stamnes, 1993).

To use Eq. 6.53 to 6.55 within GRAALS the fitting constants have to be calculated for the eight spectral bands used in GRAALS. In this work the values calculated by Zubler et al. (2011) are used. Precipitation hydrometeors like graupel, snow and rain are not taken into account in the radiation calculations. Radiative feedbacks of ice clouds are also taken into account in COSMO-ART but is not mentioned here, because SCU are warm-phase clouds.

6.6.2 New Sub-grid Scale Clouds Aerosol Cloud Interaction

Although COSMO-ART operates on the regional scale, there is still the possibility that the resolution is not sufficient enough to resolve all processes. A single grid cell could contain clouds which are smaller than the grid cell itself and therefore are not explicitly resolved. This is shown in figure 6.1, with a exemplary model grid. There are blue sky condition, where cloudiness is 0 %. On the other side there are clouds which are resolved by the grids resolution and therefore leading to a grid cell cloudiness of 100 %. But depending on grid size not every type of cloud may be resolved by the model. Imagine clouds from convective processes on very large grid sizes, where they are not resolved explicitly. To avoid this problem subgrid scale clouds are parametrized and only a part of the grid cell of the model is covered with clouds. This is seen in figure 6.1 as conditions with less than 100 % but more than 0 % cloudiness are occurring. Therefore the cloudiness due to subgrid scale clouds has to be parametrized, because the radiative impact of subgrid scale clouds should not be neglected.

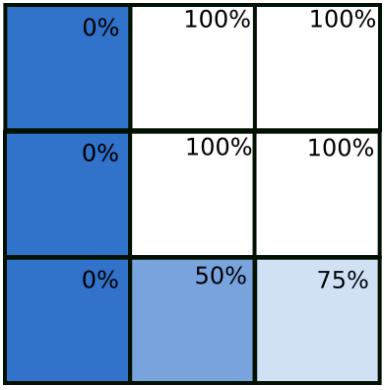

Figure 6.1: Sketch of model grid with resolved (100 %), subgrid scale cloudiness (below 100 %) and blue sky conditions (0 %).

In COSMO-ART a parametrization of subgrid scale clouds is included. In the following steps it will be shown how subgrid scale clouds and their interaction with radiation are parametrized. Note

that all subgrid scale variables are denoted as Ψ' while grid scale variables are, if not other stated, denoted as Ψ.

There are two groups of subgrid scale clouds considered in COSMO-ART. One type arises from convective processes, the other from turbulent subgrid scale processes. It may be confusing talking of convective clouds and subgrid scale clouds due to turbulent processes separately, although both types are subgrid scale clouds. The separation originates from the different processes involved with the two cloud types (convective processes, turbulent small scale processes). The convective clouds are treated within the convection parametrization of the model, which was already described in chapter 6.4. If a convective grid cell is located the convective cloud cover (CC_{con}) is calculated according to equation 6.52 from chapter 6.4.5. The convective cloud cover will be combined with the cloud cover of turbulent subgrid scale clouds, which will be explained in the following.

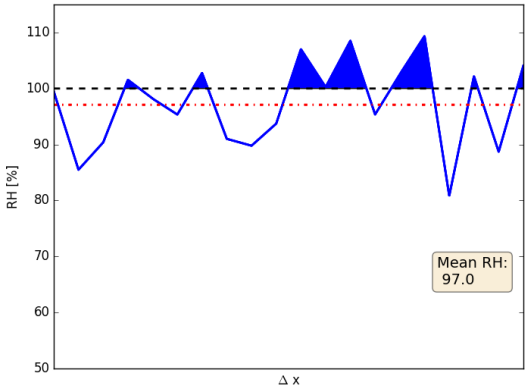

Figure 6.2: Sketch of subgrid scale fluctuation of relative humidity within Δx. Red line indicates grid box relative humidity and black dashed line is at 100% relative humidity.

Assuming that a grid box containing a certain value of relative humidity below supersaturation. In this case no gridscale cloud would be formed. But due to small scale fluctuations of relative

humidity within the grid box subgrid scale clouds may be formed. Of course the subgrid scale clouds reflect a part of the incoming solar radiation and this has to be taken into account.

The sketch in figure 6.2 shows this problem where the relative humidity of the grid box would be at 97% and no gridscale supersaturation is reached. In this case no cloud would be formed on the grid scale. On the other hand small fluctuations of relative humidity within the grid box would occur and may reach 100% or higher. This would lead to the formation of clouds with smaller extend than the grid box itself. To account for that in COSMO-ART a simple empirical approach is used to take into account subgrid scale clouds from turbulent processes. This function is based on relative humidity (RH) which is first calculated by:

$$\begin{aligned} RH &= (q_v + q_c + q_i) / q_{v,sat} \\ &= (q_v + q_c + q_i) / (q_{v,sat,water} \cdot (1 - f_{ice}) + q_{v,sat,ice} \cdot f_{ice}), \end{aligned} \tag{6.56}$$

where $q_{v,sat,water/ice}$ is the specific humidity at saturation over water and ice, q_c the liquid water content, q_i the ice content, f_{ice} is a blending ramp function within the interval [0,1] and is defined as following:

$$f_{ice}(T) = 1.0 - \left(\frac{T - 248.15}{268.15 - 248.15} \right), \tag{6.57}$$

where the temperature T is given in K. Following from that the subgrid scale cloud cover for turbulent driven clouds (CC'^{*}_{tur}) is determined by [1]:

$$CC'^{*}_{tur} = ((RH - \zeta) / (c_L - \zeta))^2, \tag{6.58}$$

where ζ is given by:

$$\zeta = 0.95 - c_1 \sigma (1 - \sigma) (1 + c_2 (\sigma - 0.05)) \tag{6.59}$$

and the parameters in 6.59 are:

[1] Note that the subscript 'tur' here refers to the subgrid scale non precipitating clouds and are to distinguish between convective cloud cover, with the subscript 'con'.

$$\begin{aligned} \sigma &= p(z)/p_0 \\ c_L &= 1.0 \\ c_1 &= 0.8 \\ c_2 &= \sqrt{3} \end{aligned}$$

where p_0 is surface pressure.

Following that it yields for the the subgrid scale cloud cover CC'_{tur}:

$$CC'_{tur} = \begin{cases} 1.0 & \text{if } q_x > 0.0 \\ 0.0 & \text{for unstable stratification} \\ CC'^{*}_{tur} & \text{else} \end{cases} \tag{6.60}$$

$CC'_{tur} = 0.0$ is set in case of unstable stratification to avoid double counting of cloud cover due to the convection parametrization. The final weight of total cloud cover CC yields:

$$CC = CC'_{tur} + CC'_{con} \cdot (1 - CC'_{tur}) \tag{6.61}$$

As an input for radiation calculation the cloud water/ice content of the subgrid scale clouds is needed. They are calculated by following assumptions:

$$\begin{aligned} q'_{c,tur} &= 0.005 \cdot q_{v,sat} \cdot (1 - f_{ice}) \\ q'_{i,tur} &= 0.005 \cdot q_{v,sat} \cdot f_{ice} \\ q'_{c,con} &= 0.01 \cdot q_{v,sat} \cdot (1 - f_{ice}) \\ q'_{i,con} &= 0.01 \cdot q_{v,sat} \cdot f_{ice} \end{aligned} \tag{6.62}$$

and a final weight gives:

$$q'_{x,rad} = q_{x,con} \cdot CC_{con} + max\left(q_{x,tur}, 0.5 \cdot q_x\right) \cdot CC_{tur} \cdot (1 - CC_{con}) \tag{6.63}$$

with $q_x \epsilon \{c, i\}$ and $q'_{x,rad}$ is used as an input for radiation calculation.

Although COSMO-ART is able to simulate aerosol cloud interaction and the impact on radiative processes (see chapter 6.6.1) this is at the moment only realized for grid scale clouds. Optical

properties of subgrid scale clouds are unaffected by changes in aerosol concentration. This of course has an impact on the evaluation of radiative forcing in environments with a changed aerosol concentration. By neglecting this important factor aerosol cloud radiation interaction is not fully mapped. Without the complete impacts of changes in the aerosol concentration there may be a significant underestimation of the indirect aerosol effect. Because impacts of a changed aerosol environment may be disguised by unchanged subgrid scale clouds.

The standard scheme in COSMO assumes a fixed effective radius of $10\,\mu\,m$ for subgrid scale cloud droplets all the time. To overcome this disadvantage it is necessary to establish the link between aerosols and subgrid scale clouds. In this work a first step will be done to include aerosol cloud interaction for subgrid scale clouds.

In this work the focus lies on the radiative impact of subgrid scale clouds. The impact on microphysical processes are not taken into account. This means that the calculated subgrid scale cloud droplet number concentration will have no effect on the microphysics of subgrid scale clouds, like initiation of precipitation. This is also due to the fact that the empirical function to calculate subgrid scale cloudiness, as it is described before, is a parametrization for non-precipitating clouds.

That the impact of non resolved clouds is an important factor in case of mesoscale models could be shown by Alapaty et al. (2012). They could show that the inclusion of subgrid scale convective clouds lead to an improvement of the representation of the radiation at the surface. But in the work of Alapaty et al. (2012) only the radiative impact of subgrid scale clouds was introduced. The dependence of the optical properties of the subgrid scale clouds on available aerosol concentration was still neglected.

As the subgrid scale cloud liquid water content is already calculated by equation 6.63 only the subgrid scale cloud droplet number concentration is needed for calculation of subgrid scale radiative impacts. Subgrid scale cloud droplet number concentration N_c' will be diagnosed every time the radiation scheme is called. But N_c' will not be advected or undergo any microphysical process. This underlies the assumption that a cloud is evolving within the grid box and is dissolving again without any significant changes in cloud droplets or producing any kind of precipitation.

The N_c' are calculated similar to the grid scale cloud droplet number concentration N_c. Therefore the approach will be the same as it was already described in chapter 6.3.1. For simplification in case of subgrid scale aerosol activation the grid scale aerosol concentration is used neglecting small scale perturbations. Like in the grid scale activation routine the same approach for the updraught velocity is used (chapter 6.3.1) but in addition there is an pseudo updraught velocity added which accounts for diabatic cooling (Seinfeld, 2006):

$$w_{tur} = w - \frac{c_p}{g}\left(\frac{\mathrm{d}T}{\mathrm{d}t}\right) \tag{6.64}$$

where T is temperature and c_p is heat capacity at constant pressure and g is the gravitational acceleration. Here the differential represents the cooling rate within the atmosphere. This takes into account for cooling processes where vertical velocity is low. The minus is necessary since a cooling in the atmosphere translates into a positive updraught velocity.

With the diagnosed N_c' and the subgrid scale cloud water mixing ratio calculated by equation 6.62 the subgrid scale effective radius r'_{eff} is calculated. With this information the radiative impact of subgrid scale clouds is then calculated by using equations 6.53 to 6.55 to calculate extinction coefficient, single-scattering albedo and asymmetry factor of the subgrid scale clouds. Instead of the grid scale liquid water content in equation 6.53 the subgrid scale liquid water content from equation 6.62 is used for calculation of the extinction coefficient. Instead of grid scale r_{eff} the subgridscale r'_{eff} is used in the equations 6.53 to 6.55. In case of grid scale liquid water content the grid scale properties are used, while in case of subgrid scale liquid water content the subgrid scale properties are used. The optical properties for subgrid scale clouds are calculated as following:

$$\beta_{ext,c} = q'_{c,rad}(a_1 r'^{b_1}_{eff} + c_1), \tag{6.65}$$

$$\omega_c = 1 - (a_2 r'^{b_2}_{eff} + c_2), \tag{6.66}$$

$$g_c = a_3 r'^{b_2}_{eff} + c_3. \tag{6.67}$$

With this approach a link between aerosol and cloud optical properties not only for grid scale cloud properties, but also for

subgrid scale cloud properties is established. This new parametrization uses gridscale aerosol concentration to calculate N_c'. Based on that the subgrid scale effective radius r_{eff}' can be calculated together with subgrid scale cloud liquid water content q_c' which is a diagnosed quantity. Therefore following relationship yields for the subgrid scale quantities:

$$\begin{aligned} q_c' &= \mathrm{f}\,(RH) \\ N_c' &= \mathrm{f}\,(CCN) \\ r_{eff}' &= \mathrm{f}\,(q_c', N_c') \end{aligned} \tag{6.68}$$

To avoid double counting the subgrid scale properties are only used if grid scale clouds are not present and if subgrid scale clouds are diagnosed. Then the properties of the subgrid scale clouds are used to calculate the radiative forcing by subgrid scale clouds. Therefore following relationship yields for grid scale Ψ and subgrid scale Ψ' quantities which then are used in the radiation scheme:

$$q_{c,rad} = \begin{cases} q_c & \text{if } q_c > 0.0 \\ q_c' & \text{else} \end{cases} \tag{6.69}$$

$$N_{c,rad} = \begin{cases} N_c & \text{if } q_c > 0.0 \\ N_c' & \text{else} \end{cases} \tag{6.70}$$

$$r_{eff,rad} = \begin{cases} r_{eff} & \text{if } q_c > 0.0 \\ r_{eff}' & \text{else} \end{cases} \tag{6.71}$$

7 Deficit of Convection Parametrizations

In this chapter sensitivity tests will show the deficits of convection parametrizations, especially the Tiedtke scheme used within COSMO-ART, regarding aerosol cloud interaction and grid size resolution. First the setup of the simulations will be briefly explained, while in the second part of this chapter the unsatisfactory results of the convection parametrization in context of aerosol cloud interaction and grid resolution will be shown.

7.1 Simulation Setup

To show the deficits of the convection parametrization used in COSMO 6 simulations with different settings will be analysed. Every single simulation starts on October 19th 2008 at 0 UTC and the time period of each simulation is 3 days. Since the experience with former simulations but with coarser resolution (Schad, 2012) an increase of horizontal resolution from 0.125° ($\approx$ 14 km) to 0.0625° ($\approx$ 7 km) is applied to better resolve the cloud structures of the marine boundary layer clouds. The domain size is chosen to still cover a reasonable large area. Additionally the vertical resolution is increased from a default value of 40 layers to 65 layers, with about 20 layers in the boundary layer together with 420 x 430 horizontal grid points and a time step of 30 s. The domain is shown in figure 8.1. The red square is the nested domain with higher resolution of 0.0125° ($\approx$2.8 km) with the same vertical resolution of 65 levels and 420x400 horizontal grid points.

To save computational time only the meteorological quantities are calculated. The meteorological initial and boundary conditions are provided by ECMWF analysis data. To calculate the cloud droplet number concentration prescribed aerosol scenarios are used. This means that for the following sensitivity study no

prognostic aerosol and gas phase chemistry is taken into account. This also means that for aerosol activation the parametrization of Segal and Khain (2006) is used to calculate cloud droplet number concentration N_c.

In four simulation only the tunable parameter b_u (see equation 6.49) is changed to show the sensibility of grid scale liquid water path (LWP) on this parameter. For the four simulations a maritime aerosol scenario is chosen for calculation of N_c because the domain covers a large area dominated by maritime conditions. In a further simulation the parameter b_u is kept constant, but the aerosol scenario for the calculation of N_c is changed to a continental scenario. To demonstrate the influence of the convection parametrization on changes in aerosol concentration two additional simulations without the convection parametrization are conducted, where one simulation used a maritime and the second a continental scenario for calculation of N_c. This selection of scenarios will demonstrate the effect on radiation and how convection parametrizations probably cloak aerosol cloud radiation effects. Table 7.1 gives a brief summary on the simulations used for this chapter.

Table 7.1: Overview of simulations in this chapter. 'X' indicates that convection parametrization is used, while '-' indicates that convection parametrization is switched off. All simulations shown here are at a grid size of about 7km.

Simulation	conv. paramet.	bu	aerosol scenario (CCN)
$bu_{33,m}$	X	0.33	maritime (100 cm^{-3})
$bu_{23,m}$	X	0.23	maritime (100 cm^{-3})
$bu_{15,m}$	X	0.15	maritime (100 cm^{-3})
$bu_{nc,m}$	-	-	maritime (100 cm^{-3})
$bu_{23,c}$	X	0.23	continental (1800 cm^{-3})
$bu_{nc,c}$	-	-	continental (1800 cm^{-3})

Some further changes are made to the convection parametrization, since former studies (Siebesma and Holtslag, 1996; Wang et al., 2004a,b) showed that the Tiedtke convection parametrization needs some adjustments in case of low-level stratocumulus clouds. Siebesma and Holtslag (1996) could show that the entrain-

ment and detrainment rates ϵ and δ of equation 6.48 should be adjusted for shallow convection. Therefore for all of the sensitivity tests the entrainment and detrainment rates ϵ and δ are set to a value of $2.5 \cdot 10^{-3}\,\mathrm{m}^{-1}$ to use the overlapping value of the range which is given in 6.51.

In this chapter the influence of the convection parametrization (Tiedtke scheme) on cloud properties and radiation will be shown. Since the Tiedtke scheme (see chapter 6.4) has several tunable parameters one is chosen to display the sensitivity of this particular parameter. Here the tunable parameter b_u is chosen which refers to the fraction of the mass flux which is allowed to detrain above the layer of zero buoyancy (see equation 6.49). Wang et al. (2004a,b) reported the sensitivity of liquid water path (LWP) on this parameter. While the focus in the study of Wang et al. (2004a,b) lied only on LWP this study will show the influence on aerosol cloud radiation interaction. Therefore three different values for this tunable parameter are chosen to investigate its impacts.

For b_u the values 0.15, 0.23, and 0.33 are chosen. The last of the three values describes the default value used in COSMO and the original value used in Tiedtke (1989). The first value is arbitrary chosen and the value of 0.23 can be found in Wang et al. (2004a,b). A similar value of 0.26 is found in Zhang et al. (2011).

7.2 Sensitivity Tests

Studies showed that several adjustments should be made if the Tiedtke convection scheme is used for simulations in the South East Pacific. As already mentioned in chapter 7.1 the entrainment and detrainment rates are adjusted according to Siebesma and Holtslag (1996). Furthermore Wang et al. (2004a,b) reported to change the parameter b_u, which denotes the fraction of the mass flux which is allowed to detrain above the layer of neutral buoyancy, to a value of 0.23. This lead to an improvement of liquid water path compared to observations. In this chapter the impact on LWP will be briefly shown for three values: 0.15, 0.23, 0.33, while the entrainment and detrainment rates are kept constant.

In figure 7.1 the changes of the horizontal mean gridscale liquid water path (LWP) over the three days of the simulation with different b_u is shown. Note that only clouds over the ocean are

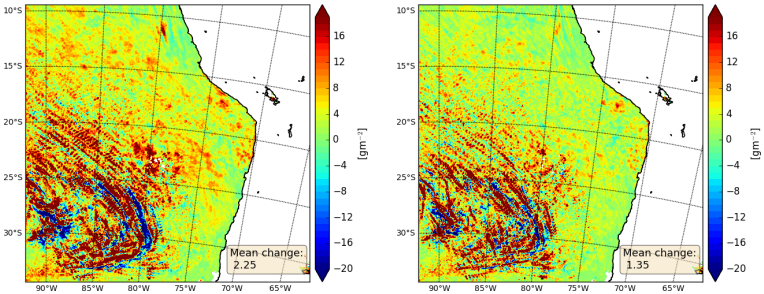

Figure 7.1: Mean changes of three day simulation on grid scale LWP by using b_u=0.33 and b_u=0.15 (left side) and b_u=0.33 and b_u=0.23 (right side).

taken into account. The left figure shows the change of $bu_{15,m} - bu_{33,m}$, which is about $2.25\,gm^{-2}$. Grid scale LWP is higher in the simulation $bu_{15,m}$ than in $bu_{33,m}$. The right side shows the changes between $bu_{23,m}$ and $bu_{33,m}$, where the change is lower compared to the other case, namely $1.35\,gm^{-2}$. High values of b_u causes that a larger fraction of cloud water is detrained over the level of neutral buoyancy. In this case the level of neutral buoyancy is the height of the boundary layer, respectively the inversion height of the boundary layer. Since in this particular case the free troposphere above the boundary layer is quite dry all the detrained cloud water is evaporated there. With lower values of b_u more grid scale cloud water is kept within the boundary layer due to lateral detrainment. Therefore more grid scale boundary layer clouds are present. This also leads to the lowest amount of grid scale boundary layer clouds in case of simulation $bu_{33,m}$. The whole region shows changes in both directions. But especially in the northern part of the domain areas with positive changes are predominant. This shows that grid scale LWP has a high sensitivity regarding the parameter b_u.

Wang et al. (2004a,b) found that the value of 0.23 seems to be more realistic than the default value of 0.33 in case of stratocumulus clouds. The value of 0.23 is now analysed in comparison to the simulation $bu_{nc,m}$ where the convection parametrization is switched off. Figure 7.2 shows the difference of the mean grid scale LWP between $bu_{23,m}$ and $bu_{nc,m}$. The change in grid scale LWP is about $9\,gm^{-2}$ and therefore substantially higher in the simulation

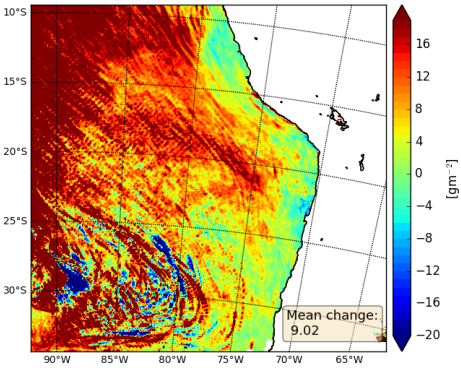

Figure 7.2: Mean changes of three day simulation on grid scale LWP by using b_u=0.23 and switching convection parametrization off

$bu_{nc,m}$ compared to the simulation $bu_{23,m}$. Again the northern parts of the domain show highest changes in grid scale LWP (larger than $16\,gm^{-2}$). It is clear that the convection parametrization has major impacts on grid scale LWP. This will be more obvious by comparing all four conducted maritime scenarios.

The timeseries in figure 7.3 shows the temporal evolution of mean gridscale LWP (only clouds over ocean are taken into account) of all four maritime simulations (see table 7.1). Again it is obvious that with a decreasing b_u mean gridscale LWP is increasing, due to the already mentioned reasons. But it is also obvious that the increase in mean gridscale LWP is highest when the convection parametrization is switched off. Changes in b_u lead to only marginal changes in gridscale LWP compared to the change of LWP if convection parametrization is switched off. This may be not remarkable, because part of cloud water is "stored" in the subgrid scale clouds of the convection parametrization, but on the other side it may be not so obvious and it should be pointed out here. In addition if the convection parametrization is used the boundary layer seemed to be more permeable for humidity and cloud water. The simulations with convection parametrization revealed that the boundary layer is much drier over time compared to the simulation $b_{nc,m}$ (not shown here).

As convection parametrization impacts the representation of boundary layer clouds and impacts massively the amount of grid-scale LWP this will also have impacts on radiative properties of the boundary layer clouds. In COSMO the subgrid scale LWP is on the one hand used as input for the radiation scheme to take radiative effects of subgrid scale clouds into account. But on the other hand the subgrid scale LWP which is used for radiative impact is diagnosed in the radiation scheme (see chapter 6.6.2). The subgrid scale LWP which is calculated within the convection parametrization is not used within the radiation scheme. This results in a shortcoming that the convection parametrization has a substantial impact on grid scale LWP, where aerosol cloud radiation interaction is realized, but subgrid scale LWP from the convection parametrization is not used in radiation scheme. Additionally there is no linkage between subgrid scale cloud optical properties and aerosol concentration.

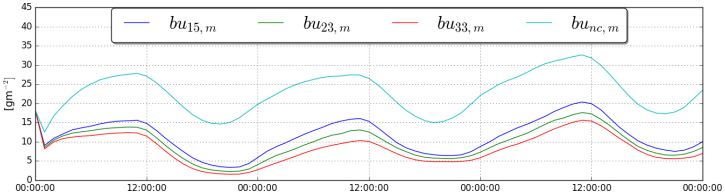

Figure 7.3: Time series of mean grid scale LWP over total domain for different values of tunable parameter b_u ($bu_{15,m}, bu_{23,m} bu_{33,m}$) and a simulation where convection parametrization is switched off ($bu_{nc,m}$).

To reveal the influence of the convection parametrization on the radiation the changes in cloud effective radius r_{eff}, and cloud optical depth τ_c is further analysed since they have the biggest impact on radiation.

The convection parametrization has two major drawbacks to study aerosol cloud interaction. First is the use of a one moment bulk microphysics scheme. As described in chapter 6.4.4 the convection parametrization has only a simplified cloud model which is independent of aerosol concentration. The second drawback is as shown in chapter 6.6 that the radiative properties are only a function of diagnosed subgrid scale liquid water content q_c'. In

principle those two drawbacks lead to two major problems in studying aerosol cloud interactions.

First, the simple cloud model excludes changes in aerosol load and composition. Additionally there will be no microphysical changes in the parametrized processes. For example changes in precipitation processes are not linked to changes in aerosol concentrations. Changes in aerosol load would lead to changes in microphysical processes and lead to less or more precipitation. This processes are not taken into account in a simple cloud model like it is used in the Tiedtke convection scheme. A change in parametrized precipitation results mainly from changes of grid scale properties. Of course the grid scale properties could be changed due to changed in aerosol properties. But still there is no direct link to the microphysical scheme of the parametrization and the cloud model is unaffected by aerosol concentrations. Furthermore as long as the convection parametrization is used in COSMO there is no possible way to produce drizzle since it is inhibited for the shallow convection scheme (see 6.4.4).

Second, changes in subgrid scale cloud optical properties are not linked to aerosols. That subgrid scale convection and therefore the corresponding subgrid scale clouds and their feedback on radiation plays an important role even for regional models could be shown by Alapaty et al. (2012). But without any changes of the optical properties due to changes in aerosol loading and/or composition there is also no changes in radiative feedback from the convective subgrid scale clouds. A further problem is the detrainment of cloud water resulting from the convection scheme. The detrainment is a source for grid scale cloud water q_c but there is no source for grid scale cloud droplet number concentration N_c, which is slightly inconsistent. This depict a source for mass but not for number concentration and may also lead to a bias in r_{eff}.

To further investigate the influence of the convection parametrization on cloud properties two additional simulations are conducted. One with $b_u = 0.23$ ($bu_{23,c}$) and a second with switching off the convection parametrization ($bu_{nc,c}$), but each with a continental aerosol scenario (1800 cm^{-3} CCN). Now it will be briefly analysed how cloud optical properties changed due to a change in aerosols if convection parametrization is switched on and off.

For this purpose the probability density function (PDF) of liquid water content (LWC), effective cloud droplet radius r_{eff},

and cloud optical depth τ_c for $bu_{23,m}$ and $bu_{nc,m}$ is evaluated (figure 7.4). To calculate the PDF only grid scale cloudy points are taken into account for LWC and r_{eff}. For τ_c every grid point is taken into account where τ_c is greater then zero. The numbers in brackets in the legend behind the simulation denotes the number of points taken into account in the PDF. All are 3D variables and depending on gridscale clouds, except τ_c which is a 2D variable but is additionally depending on subgrid scale properties (see chapter 6.6.2). All three days of the simulation period are taken into account.

The PDFs of the LWC in case of the maritime scenarios ($bu_{23,m}$, $bu_{nc,m}$) have a similar structure. But note that the PDF just shows the distribution and not the amount of grid points which are taken into account. To illustrate this also the number of grid points which are taken into account for the calculation of the PDF is shown in the legend of the plot. The simulation $bu_{23,m}$ has nearly 1/5 less grid points taken into account for the calculation of the PDF. This illustrates even more the previous findings that less gridscale LWC is available if the convection parametrization is used. This is similar in case of r_{eff} where again fewer grid points are taken into account. The differences in the PDFs of r_{eff} are obvious. $bu_{nc,m}$ shows a slight peak in r_{eff} around 15-16 μm which is not the case in $bu_{23,m}$, where no distinct peak is visible. Additionally there is a much steeper slope from the peak to smaller values of r_{eff} in $bu_{nc,m}$ which is not recognizable in $bu_{23,m}$. The slope towards smaller values of r_{eff} in case of $bu_{23,m}$ is much smoother than in $bu_{nc,m}$. And the PDF of $bu_{23,m}$ shows a shift to smaller values of r_{eff} compared to $bu_{nc,m}$. τ_c shows obvious differences between $bu_{23,m}$ and $bu_{nc,m}$, where $bu_{nc,m}$ peaks between a value of 0.8 and 1.0. On the other side $bu_{23,m}$ peaks at slightly higher values between 1.0 to 1.3. This indicates optically thicker clouds in case of $bu_{23,m}$. High values of τ_c are less occurring in $bu_{nc,m}$ compared to $bu_{23,m}$. All in all $bu_{23,m}$ is shifted to higher values of τ_c compared to $bu_{nc,m}$. Note that in this case nearly the same amount of grid points are taken into account. This is due to the fact that τ_c is also depending on subgrid scale clouds and now clouds from convection and turbulent processes are taken into account in calculation of τ_c. Although the convection parametrization is switched off nearly the same amount of grid points taken into account in case of τ_c, which makes the results comparable towards radiative impact. It

is obvious that there is a substantial difference in τ_c between both scenarios.

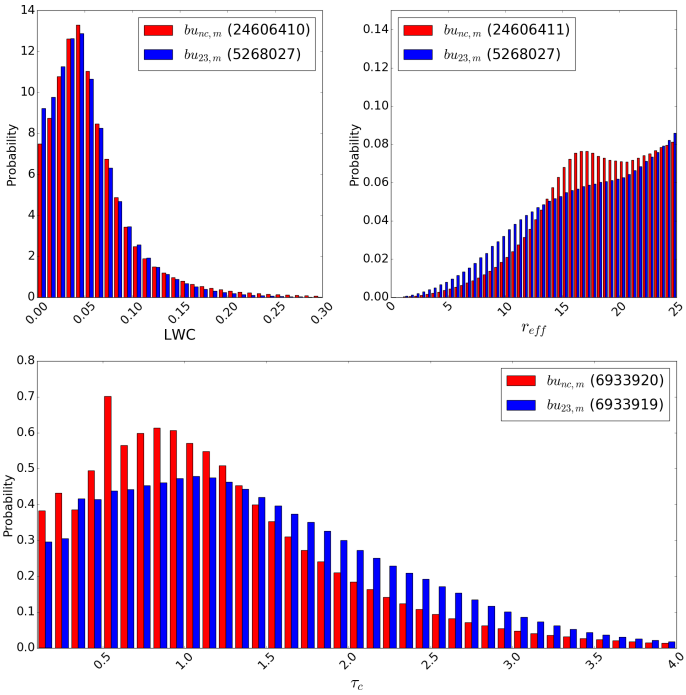

Figure 7.4: PDFs of simulation $bu_{23,m}$ and $bu_{nc,m}$ for liquid water content (LWC), effective radius (r_{eff}) of cloud droplets, and cloud optical depth (τ_c). Note that the PDF of τ_c takes every cloudy (grid & subgrid scale) grid box and the PDFs of LWC and r_{eff} takes only grid scale cloudy boxes into account. Number in brackets are grid points taken into account.

Comparing the PDFs of the continental cases (figure 7.5) reveals that in case of $bu_{23,c}$ nearly 1/4 less grid points are taken into account than in case of $bu_{nc,c}$ (LWC and r_{eff}). But in case of the continental scenarios ($bu_{23,c}$ and $bu_{nc,c}$) the PDFs of LWC, r_{eff}, and τ_c have a similar shape. This already indicates that the convection parametrization produces optically thick clouds since the continental scenario with no convection parametrization fits

better to the continental scenario with convection parametrization than the maritime scenarios (shallow convection on or off) to each other. It indicates that the parametrization of subgrid scale clouds originating from shallow convection produces optically too thick clouds. On the other hand τ_c indicates that the convection parametrization has a major impact on radiation which should not be neglected.

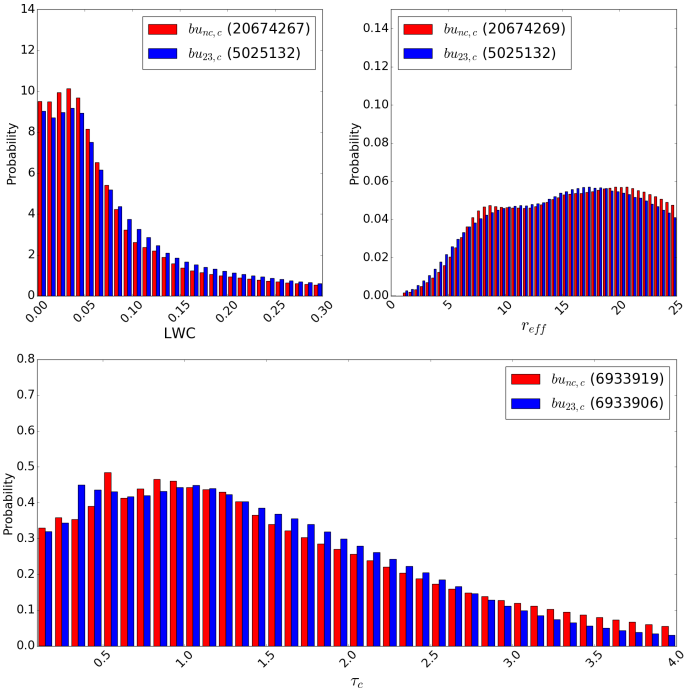

Figure 7.5: PDFs of simulation $bu_{23,c}$ and $bu_{nc,c}$ for liquid water content (LWC), effective radius (r_eff) of cloud droplets, and cloud optical depth (τ_c). Note that the PDF of τ_c takes every cloudy (grid & subgrid scale) grid box and the PDFs of LWC and r_{eff} takes only grid scale cloudy boxes into account. Number in brackets are grid points taken into account.

To better understand the impact of the convection parametrization the PDFs of the different aerosol scenarios are compared to

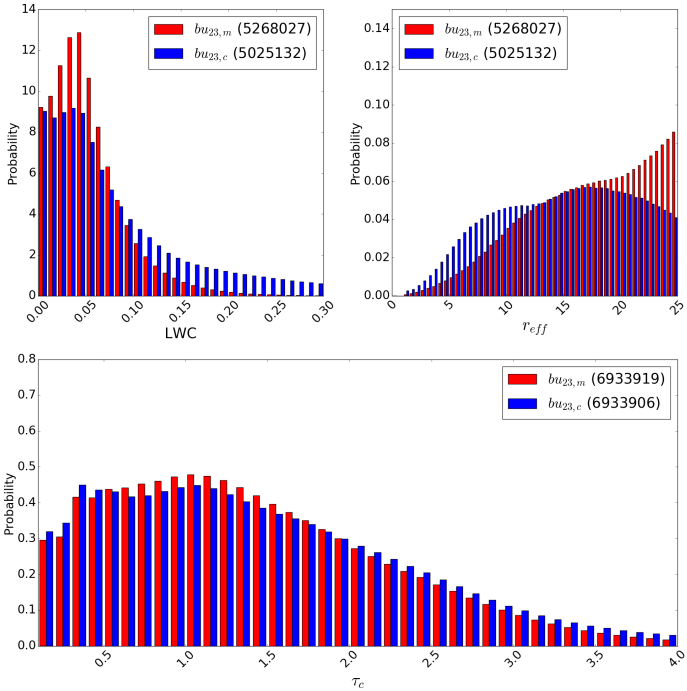

Figure 7.6: PDFs of simulation $bu_{23,m}$ and $bu_{23,c}$ for liquid water content (LWC), effective radius (r_eff) of cloud droplets, and cloud optical depth (τ_c). Note that the PDF of τ_c takes every cloudy (grid & subgrid scale) grid box and the PDFs of LWC and r_{eff} takes only grid scale cloudy boxes into account. Number in brackets are grid points taken into account.

each other ($bu_{23,m}$ vs. $bu_{23,c}$ and $bu_{nc,m}$ vs. $bu_{nc,c}$). In figure 7.6 the PDFs of $bu_{23,m}$ are compared to the ones of $bu_{23,c}$. LWC is shifted from lower to higher values. This is accompanied with a decrease of r_{eff}, which is expected since an increase in aerosol concentration leads to a higher number concentration of cloud droplet number concentration N_c and therefore leading to a decrease in r_{eff}. The increase of N_c leads to a suppression of precipitation and therefore to an increase in LWC. Furthermore there is a slight increase in overall τ_c since values are slightly shifted to higher

values. This is also expected according to the Twomey effect, that an increase in aerosol concentration would lead to optically thicker clouds.

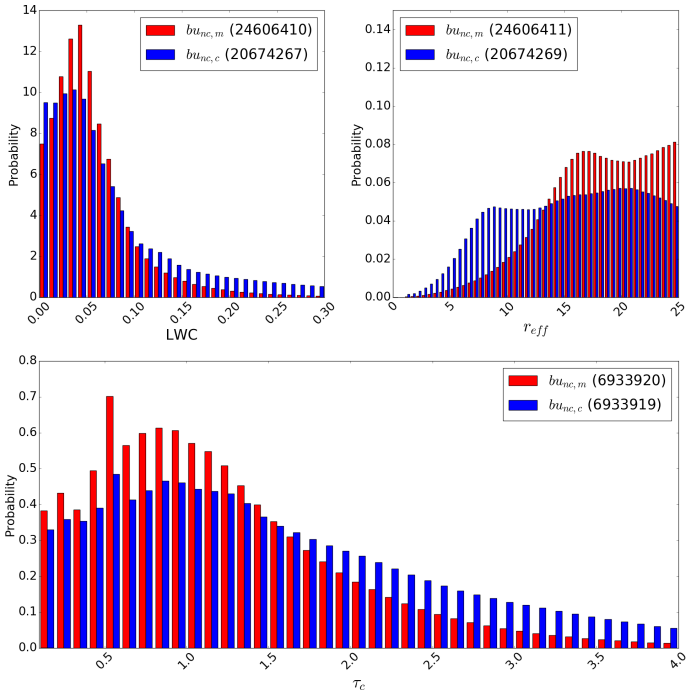

Figure 7.7: PDFs of simulation $bu_{nc,m}$ and $bu_{nc,c}$ for liquid water content (LWC), effective radius (r_eff) of cloud droplets, and cloud optical depth (τ_c). Note that the PDF of τ_c takes every cloudy (grid & subgrid scale) grid box and the PDFs of LWC and r_{eff} takes only grid scale cloudy boxes into account. Number in brackets are grid points taken into account.

In figure 7.7 the PDFs of $bu_{nc,m}$ and $bu_{nc,c}$ are compared to each other. LWC is shifted to higher values, while r_{eff} is shifted to lower values and that is what is expected according to the Twomey effect. Comparing the PDFs of $bu_{nc,m}$ and $bu_{nc,c}$ to the ones of $bu_{23,m}$ and $bu_{23,c}$ shows that the shifts are diverse. Although the shift in LWC seems to be similar regardless of switching convection

parametrization on or off the changes in r_{eff} are enormous. The shift in r_{eff} seems to be more pronounced in case of $bu_{nc,m}$ to $bu_{nc,c}$ from higher to lower values of r_{eff}. While $bu_{nc,m}$ and $bu_{nc,c}$ have both a distinct peak at $15\mu m$ and $8\mu m$ respectively. The PDFs in case of $bu_{23,m}$ and $bu_{23,c}$ don't show such distinct peaks. This already reveals clear differences if the convection parametrization is used or not in an environment with changing aerosol concentrations. But even more interesting is the change in τ_c. There is a clear shift from lower values of τ_c in case of $bu_{nc,m}$ towards higher values in case of $bu_{nc,c}$, which clearly shows the effect of a change in aerosol concentration in cloud optical properties. In case of $bu_{23,m}$ and $bu_{23,m}$ the shift is not that pronounced. This is due to the fact that the convection scheme is not aware of aerosol concentration. There is no linkage between aerosols and microphysics and cloud optical properties. As τ_c is only a function of diagnosed subgrid scale LWC' and LWC' is not affected by aerosols, also subgrid scale τ_c is not affected by aerosols. Furthermore the subgrid scale effective radius is a fixed value and is unaffected by a change in aerosol concentration. A further slight inconsistency is that the radiation scheme uses a diagnosed subgrid scale LWC' and not that which is calculated within the convection scheme. At the end radiative properties resulting from the convection parametrization are directly unaffected by a change in aerosol concentration. There is still the possibility that radiative properties are changed due to a change of aerosol concentration. But this change is happening indirectly due to a change in grid scale properties. The impact is depending on the magnitude of the influence of the convection parametrization on the total radiative properties. In the end this may lead to an underestimation of the aerosol effect.

To quantify the impact on radiation the change of the mean short-wave radiative fluxes at top of the atmosphere (TOA) is plotted in figure 7.8 for $\Delta bu_{23} = bu_{23,m} - bu_{23,c}$ (left side) and $\Delta bu_{nc} = bu_{nc,m} - bu_{nc,c}$ (right side). The most obvious difference between those simulations is the northern part of the domain. In case of Δbu_{23} there are areas with nearly no change in radiative forcing accompanied by areas with slight positive radiative forcing. Contrary Δbu_{nc} shows in the same area a substantial negative radiative forcing. A small feature along the coast in the northern part of the domain (around 15°S, 78°W) is quite interesting since

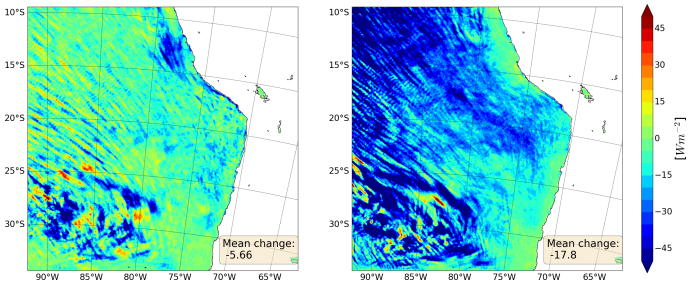

Figure 7.8: Changes of short-wave radiative fluxes at TOA between $bu_{23,m}$ and $bu_{23,c}$ (left) and $bu_{nc,m}$ and $bu_{nc,c}$ (right).

in case of the convection parametrization it shows a negative short-wave forcing and on the other hand it shows none to small positive forcing in case of Δbu_{nc}. This may not be directly related to the convection parametrization and its impact on radiation but may result from differences in grid scale meteorological variables. Still its worthy to mention it, because it shows the opposite sign. The southwestern part of the domain shows quite similar effects in both cases, where areas exhibit positive but also strong negative radiative forcing.

In case of Δbu_{23} the mean change in radiative forcing is about -5.66 Wm^{-2}. While the mean change in case of Δbu_{nc} is about -17.8 Wm^{-2}. Due to the large difference it is obvious that the convection parametrization has a substantial impact on radiative forcing. Furthermore it reveals that the impact can have the opposite sign in same areas if convection parametrization is used or not. This shows a substantial problem in the investigating of the impacts of aerosol cloud radiation interactions.

It is obvious that in some parts of the domain the impacts result in a different outcome if the convection parametrization is switched off. Since there is no interaction between aerosol and cloud microphysics of the convection scheme it is hard to speak of investigating aerosol cloud interaction and the impacts on radiation in this context. The results shows that the convection parametrization has a large impact on quantities which are relevant for cloud radiative feedbacks (like τ_c). Those quantities are on grid scale linked to aerosols and therefore an aerosol cloud ra-

diative interaction is established. While this is not true for subgrid scale processes. Therefore a shortcoming arises for the convection parametrization if aerosol cloud radiation impacts are investigated. Furthermore the inconsistent treatment of the subgrid scale LWC' which is taken into account for radiative calculation is a further shortcoming in COSMO. It could be shown that the impact on radiative forcing in a changed aerosol environment is foiled by the convection scheme if aerosol cloud interaction is not taken into account in the parametrization.

The effect of the parametrization is even worse in case of the simulation with 2.8 km grid spacing. The nested domain reveals a very worrying effect of the Tiedtke scheme in COSMO since it inhibits, in this very particular case of a stable boundary layer, the production of grid scale LWP (see figure 7.9). In the default setup of COSMO at the DWD the shallow convection scheme is active on that grid spacing. But in this particular case of a stable boundary layer this leads to a fatal result since nearly no gridscale LWP is visible in the simulations. In this case nearly no microphysical processes are taking place on the grid scale and the subgrid scale part of the Tiedtke scheme is taking over. This is contrary to the purpose of a subgrid scale parametrization. One hint to the problem could be that the scheme itself is not scale aware, which means it cannot adapt to smaller grid sizes, although it should be scaled to the grid size. In the case of the Tiedtke scheme it would be the assumption that the updraught area is much smaller than the grid size itself, which is questionable for grid sizes in the range of 2.8 km. For this the use of a scale dependent version of the COSMO shallow convection scheme should be used, which is not available for this work. A more detailed discussion about the problems of convection parametrizations can be found in the work of Arakawa (2004).

Because of the subjective tuning of the parameter b_u and its impact on cloud optical properties (like LWP and r_{eff}) and the fact that the convection parametrization performs horrible in case of the highest resolved model domain and as it is not aware of any aerosol cloud interaction it is decided that any further simulation with both grid sizes are conducted without the convection parametrization.

The sheer fact that there is no aerosol cloud interaction linked to the convection parametrization and the resulting radiative impact make it difficult to rely on the parametrizations. Not only that

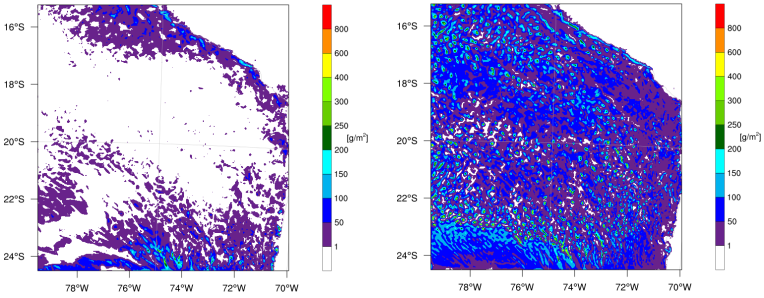

Figure 7.9: Grid scale LWP for simulation with grid size 2.8 km in case with convection parametrization on (left side) and off (right side)

there is a problem with scale dependency as it was pointed to since years by Arakawa (2004). Additionally the missing link to aerosols is a further disadvantage of those parametrizations and make them to a big construction yard in global modelling.

This arises the question how good is aerosol cloud interaction represented in GCMs at the moment since most, if not all, cloud processes are on the subgrid scale in those models. How big is the bias due to convection parametrizations which are not aware of aerosols and grid size? As it was pointed out in the last IPCC report (Boucher et al., 2013) convection parametrizations are not performing very well regarding precipitation. Convection parametrizations are still not capable to reproduce precipitation in the right manner. Furthermore the response of low-level clouds to global warming seems to be problematic in GCMs. The IPCC report (Boucher et al., 2013) states that they have a positive response and the report is not confident that this is realistic, since this behaviour is not well understood, nor it is effectively constrained by observations.

Within the global model ECHAM6 for example the cloud cover is tuned in areas where SCUs are occurring frequently to get at least some cloudiness in this areas where low-level clouds evolving under a sharp inversion due to the relatively coarse vertical resolution of the model (Giorgetta et al., 2013). This shows that SCUs are still a very challenging task for models, especially for GCMs.

8 Comparison of Model Simulations with Observational Campaign VOCALS-REx

8.1 Simulation Setup

8.1.1 Setup of the Simulation with 7km resolution

To simulate a real case scenario it is necessary to evaluate the capability of COSMO-ART reproducing the conditions in the South East Pacific (SEP). Most, if not all, global models have difficulties simulating marine boundary layer clouds in regions like the SEP, mainly due to the coarse vertical and horizontal resolution. Even regional models encounter problems simulating the properties of marine boundary layer (Wyant et al., 2015). To better understand the processes in this special region a major campaign was conducted in the year 2008 to observe essential cloud properties (Wood et al., 2010).

To evaluate the skill of COSMO-ART a time period during the campaign in October 2008 is chosen. The start of the simulation is on 19th October 2008 and endures 25 days. For this period the skills of COSMO-ART are evaluated against observations. Since the experience with former simulations, but with coarser resolution (Schad, 2012), an increase of horizontal resolution from 0.125° ($\approx$ 14 km) to 0.0625° ($\approx$ 7 km) is performed to better resolve the cloud structures of the marine boundary clouds. The domain is chosen to still cover a reasonable large area. Additionally the vertical resolution is increased from a default value of 40 layers to 65 layers, with about 20 layers in the boundary layer together with 420 x 430 horizontal grid points and a time step of 30s. The domain is

shown in figure 8.1. A further simulation with higher resolution is performed. This simulation is nested into the domain with 7 km grid spacing. The red square indicates the nested domain with the higher resolution and will be described in chapter 8.1.2.

ECMWF analysis data is used as a driver of the meteorological initial and boundary conditions. The boundaries are updated every 6 hours. To avoid prescribed gas profiles and a cold start of aerosols, data from the global chemical model MOZART (Brasseur et al., 1998) is used and the chemical input data is updated every 6 hours. Since MOZART only delivers mass mixing ratio for aerosols this data is prepared to fit to the lognorm distributions of COSMO-ART. The number concentration of the aerosols is calculated from the mass.

The interval of the call of the radiation scheme is increased from 60 minutes to 30 minutes, which shows a slight improvement in the simulations (not shown here). Instead of the bulk microphysics scheme the more sophisticated two moment microphysics scheme of Seifert and Beheng (2006) is used. The cloud droplet number concentration is calculated using prognostic aerosol concentrations from COSMO-ART as it is described in chapter 6.3.1.

As the convection scheme shows several deficits (more details chapter 7) it is not used in the simulations. The 25-day continuous simulation is compared to several meteorological data observed during VOCALS-REx. After that multiple climate engineering scenarios are performed, where the size of the seeded sea salt particles is varied. An overview of the conducted simulations is given in table 8.1.

8.1.2 Setup Simulation 2.8km resolution

COSMO-ART has the ability to be nested into a coarser COSMO-ART simulation. To further improve the simulated cloud structures a nested simulation with a resolution of $0.0125°$ (≈ 2.8 km) is performed. The boundary data is prescribed by using the output of the coarser simulation (chapter8.1.1) and is updated every hour. Like the coarser resolution 65 levels in the vertical is used, together with 420 x 400 horizontal grid points and with a time step of 20s. The red square in figure 8.1 shows the nested domain. Convection parametrization is switched off, because of the reasons described in chapter 7.2.

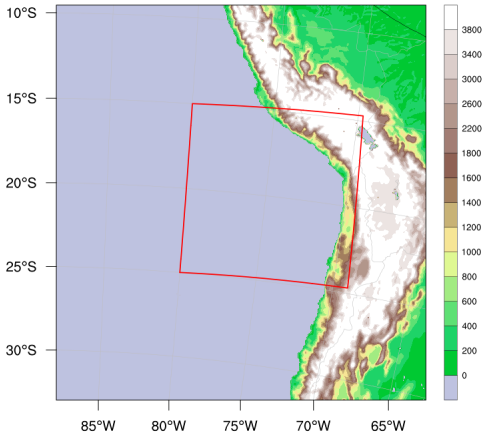

Figure 8.1: Simulated outer domain with grid size of 7 km and nested domain with grid size of 2.8 km (red square)

8.2 Role of Subgrid Scale Cloud Processes

As already mentioned in chapter 6.6.2 COSMO-ART takes subgrid scale clouds from turbulent processes into account. Those diagnosed non-precipitating clouds can have a substantial impact on radiation and therefore it is necessary to link them to aerosols to include subgrid scale aerosol cloud interaction (sACI). This was missing in COSMO-ART before this work and in the standard configuration the effective radius r'_{eff} of subgrid scale clouds is set to a value of $10\mu m$. Two reference simulations are carried out with grid spacing of 7 km ($REF7_{nosgs}$) and 2.8 km ($REF2.8_{nosgs}$) with the fixed value of $10\mu m$ for r'_{eff}. Two further simulations ($REF7_{sgs}$ and $REF2.8_{sgs}$) are carried out, where the gridscale prognostic aerosol is used to calculate r'_{eff}as it is described in chapter 6.6.2. In the following the results will be discussed briefly.

Table 8.1: Overview: setups of the simulations for comparison with VOCALS-REx and CE. All listed simulations convection parametrization was switched off.

Simulation	CE scenario (emitted sea salt mode)	grid points	grid size	time step
$REF7_{sgs}$	-	420 x 430 x 65	7km	30s
$REF7_{nosgs}$	-	420 x 430 x 65	7km	30s
$CEA7_{sgs}$	sa	420 x 430 x 65	7km	30s
$CEA7_{nosgs}$	sa	420 x 430 x 65	7km	30s
$CEAB7_{sgs}$	sa & sb	420 x 430 x 65	7km	30s
$REF2.8_{sgs}$	-	420 x 430 x 65	2.8km	20s
$REF2.8_{nosgs}$	-	420 x 430 x 65	2.8km	20s
$CEA2.8_{sgs}$	sa	420 x 430 x 65	2.8km	20s
$CEB2.8_{sgs}$	sb	420 x 430 x 65	2.8km	20s
$CEAB2.8_{sgs}$	sa & sb	420 x 430 x 65	2.8km	20s

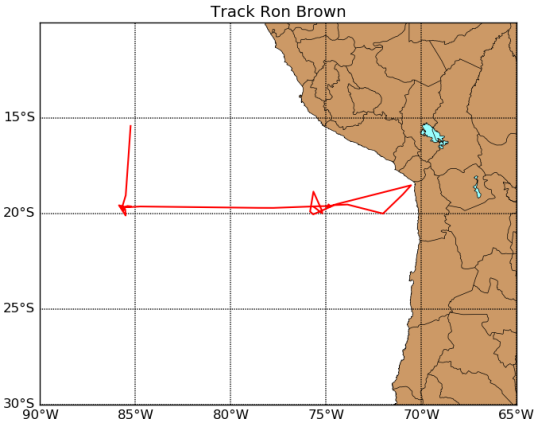

Figure 8.2: Path of the Ron Brown during VOCALS REx from October 24th to October 31st.

For comparison the measurements of the ship Ron Brown[1] are used. The path of the ship is displayed in figure 8.2. It cruised

[1]Data are provided by Simon de Szoeke (Oregon State University), Daniel Wolfe (NOAA/ESRL/PSD), Sandra Yuter (North Carolina State Univer-

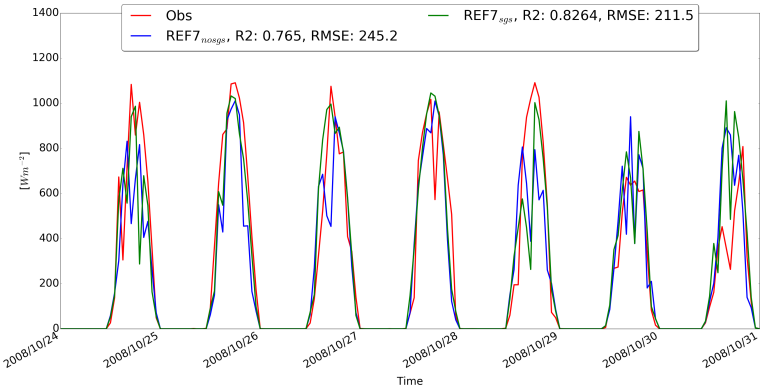

Figure 8.3: Time series of shortwave measured by Ron Brown during VOCALS-REx from October 24th to October 31st. Obs = Observations.

mainly along 20°S. The incoming solar radiation was measured by the ship and is compared to the hourly instantaneous values of the simulations $REF7_{nosgs}$ and $REF7_{sgs}$, which can be seen in figure 8.3. The RMSE and coefficient of determination ($R2$) is only calculated if the shortwave radiation is greater then zero. Note that this is a consecutive simulation which runs completely free after initialisation and only the boundaries are updated. The comparison to observations starts five days after initialisation of the model simulation.

$REF7_{nosgs}$ shows that the daily cycle of shortwave radiation compared to observation is quite well captured by the model. The shortwave radiation which is reaching the ground is most of the time slightly underestimated in case of $REF7_{nosgs}$. That not all features are captured by the model is not surprising since it is a free running simulation and after five days of simulation you would not expect that every detail is perfectly reproduced by the model. But all in all the results are comparing fairly good in case of $REF7_{nosgs}$. The RMSE is about 245.2 Wm^{-2} and $R2$ is about 0.765.

sity), and Chris Fairall (NOAA/ESRL/PSD) with funding from the NOAA Climate Program Office.

But if sACI is taken into account ($REF7_{sgs}$) the importance of the subgrid scale clouds is revealed. There are quite significant differences compared to $REF7_{nosgs}$. For example at the third peak there is a considerable difference between $REF7_{nosgs}$ and $REF7_{sgs}$ where more shortwave radiation reaches the ground in $REF7_{sgs}$ compared to $REF7_{nosgs}$. Quite obvious is the difference at the seventh peak where a sharp decrease in shortwave radiation in $REF7_{sgs}$ can be seen which is not visible in $REF7_{nosgs}$. That aerosol awareness of subgrid scale clouds is important is reflected by the RMSE and $R2$. Both are improving to 211.5 Wm^{-2} and 0.82 respectively.

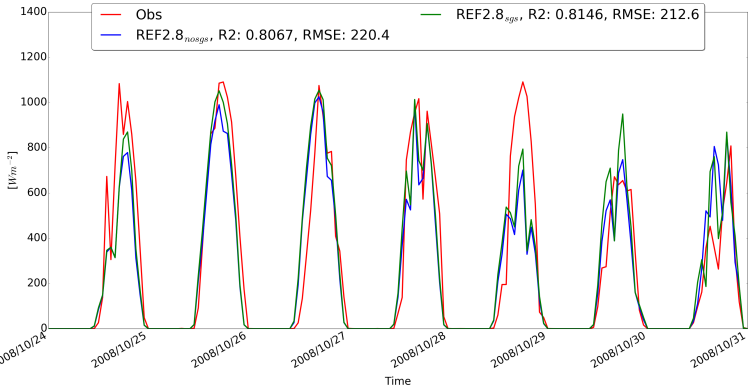

Figure 8.4: Time series of shortwave measured by Ron Brown during VOCALS-REx from October 24th to October 31st. Obs = Observations.

Similar effects are seen in case of $REF2.8_{nosgs}$ and $REF2.8_{sgs}$ which are shown in figure 8.4. It is obvious that $REF2.8_{nosgs}$ is already performing much better than $REF7_{nosgs}$ as RMSE is about 220.4 Wm^{-2} and $R2$ is 0.8067. And $REF2.8_{sgs}$ is performing better than $REF2.8_{nosgs}$ since RMSE is improving to 212.6 Wm^{-2} and $R2$ to 0.8146. However the improvement is smaller compared to the improvement of $REF7_{nosgs}$ to $REF7_{sgs}$. This gives the hint that subgrid scale clouds becoming less important in case of the higher resolved simulation which is satisfying since clouds become more and more resolved by the grid spacing. Since RMSE and $R2$ are about the same magnitude in case of $REF7_{sgs}$ and $REF2.8_{sgs}$

and together with the large improvement from $REF7_{nosgs}$ to $REF7_{sgs}$ it shows how important the right treatment of subgrid scale clouds is. Without the subgrid scale aerosol cloud radiation interaction the model performs not as good as with and therefore it should not be neglected.

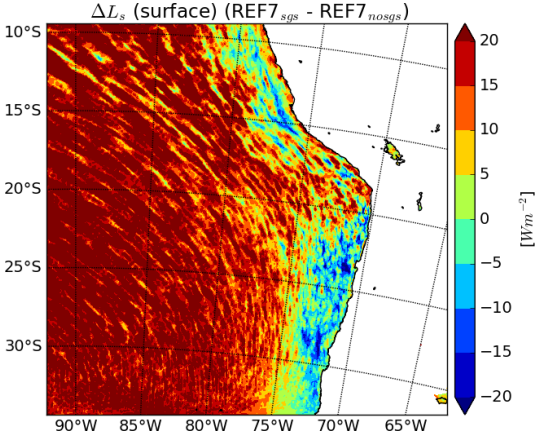

Figure 8.5: Impact on shortwave radiation L_s at surface by including ACI for subgrid scale clouds.

The importance to include subgrid scale aerosol cloud radiation interaction is obvious if the changes of the mean shortwave radiation L_s at the surface is evaluated. The changes are plotted in figure 8.5 for $\Delta REF7 = REF7_{sgs} - REF7_{nosgs}$ and in figure 8.6 for $\Delta REF2.8 = REF2.8_{sgs} - REF2.8_{nosgs}$. It reveals the main disadvantage if a prescribed value of r'_{eff} is used for subgrid scale clouds. Shortwave radiation is increased in the maritime remote area far away from the coast. This means that in case of $REF7_{sgs}$ more shortwave radiation compared to REF_{nosgs} is reaching the surface, which is mainly due to the fact that the maritime conditions lead to larger r'_{eff} compared to the prescribed value. On the other side there is a negative radiative forcing near the coast because the cloud droplets are smaller compared to the prescribed value. Near the coast anthropogenic aerosol leads to polluted conditions which results in smaller cloud droplets.

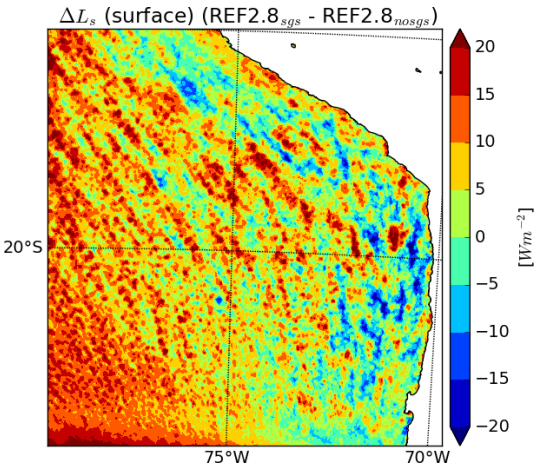

Figure 8.6: Impact on shortwave radiation L_s at surface by including ACI for subgrid scale clouds.

Figure 8.6 shows L_s in case of $\Delta REF2.8$. There is an increase of incoming shortwave radiation in the remote area and a small decrease near the coast. This is due to the same reasons as mentioned before. The remote area is more pristine and the coastal area is perturbed by anthropogenic aerosol. This results in a gradient of r'_{eff} which is not covered if subgrid scale aerosol cloud interaction is not taken into account.

In areas with a sharp gradient of aerosol concentration as it is the case in the southeast pacific it leads to an underestimation of cloud radiative forcing induced by aerosol changes. If neglected the forcing of subgrid scale clouds is overestimated in areas with low amount of aerosols, while it is underestimated in areas with high amount of aerosol concentration.

The impact is quite significant as the mean change in shortwave radiation at the surface is about $14\,\mathrm{Wm}^{-2}$ in case of $\Delta REF7$. This is mainly due to the fact that a large area is dominated by maritime conditions. The change of $\Delta REF2.8$ is only about $5.46\,\mathrm{Wm}^{-2}$. This results from the fact that a larger fraction of the simulated domain is affected by anthropogenic aerosol, compared to the coarser and larger domain.

It is shown that at coarser resolutions subgrid scale clouds are more important, since it is not possible to resolve the clouds accurately at coarser grid sizes. Therefore it is vital to include subgrid scale ACI. Although this region is very special due to its sharp transition from polluted conditions to maritime conditions and therefore the effect of including subgrid scale aerosol interaction is very clearly seen, the essence that it is important to include subgrid scale aerosol interaction is also valid in other regions. This will have further impacts in case of MCB because neglecting the subgrid scale aerosol cloud interaction would underestimate the effect of MCB.

This chapter shows that it is necessary to include aerosol cloud radiation interactions for subgrid scale clouds. In case of subgrid scale processes which are necessary for coarser grid sizes it is vital that all parametrizations are linked to aerosol changes. It is shown that if subgrid scale aerosol cloud interaction is included the simulation with coarser resolution compares similar good to observation as the higher resolved simulation. Otherwise if subgrid scale ACI is neglected it leads to biases and underestimation of the aerosol effect.

8.3 Comparison with Observations (VOCALS-REx)

As shown in the previous chapter the model results of $REF7_{sgs}$ and $REF2.8_{sgs}$ compare fairly good to observational shortwave radiation. Because subgrid scale aerosol cloud interaction (sgsACI) is an important factor from now on every simulation takes, if not other mentioned, sgsACI into account. In this chapter the model results are compared to satellite data, radiosondes and in-situ measurements taken during the measurement campaign VOCALS-REx (Wood et al., 2010).

To compare the liquid water path (LWP) of the model results to satellite observations (Tenth Geostationary Operational Environmental Satellite (GOES-10) with methods of Minnis et al. (2011))[2] a 25 day mean at 13 UTC and 17 UTC is used. The satellite data is regridded to the grid size of the model results, while the model results contain sub-grid scale diagnosed LWP.

The observations show at 13 UTC (figure 8.7) a nearly uniform distribution of LWP with values of 100 to 150 $\mathrm{g\,m^{-2}}$ and lower values near the coast and the southwest region of the domain. There are only few regions where LWP passes over 150 $\mathrm{g\,m^{-2}}$. A small band with lower values between 40 to 60 $\mathrm{g\,m^{-2}}$ along the coast is visible. Higher values are located direct at the coast around 73°W and 18°S and 79°W and 12°S.

The results of $REF7_{sgs}$ show nearly the same uniform distribution of LWP with values between 150 to 200 $\mathrm{g\,m^{-2}}$, where also single areas reach values greater then 200 $\mathrm{g\,m^{-2}}$. The band like structure with increased values of LWP (reaching from 75°W and 25°S to 20°S and then reaching to 85°W and 10°W) is visible in $REF7_{sgs}$, but with higher values and shifted more towards the coast. Although the model results don't show the lower values in the same magnitude compared to satellite observations along the coast, they show the small increased band of LWP compared to the surroundings near the coast of Peru (73°W, 17°S and 78°W, 12°S), as well along the coast of Chile (73°W, 28°S) which is also seen in the satellite data.

[2] Data was obtained from the NASA Langley Cloud and Radiation Research Group, http://angler.larc.nasa.gov/satimage/products.html

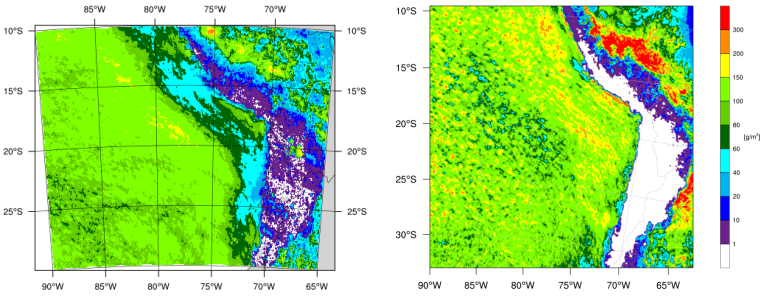

Figure 8.7: 20 day mean of LWP at 13 UTC from observations (left) and $REF7_{sgs}$ (right).

At 17 UTC the observations show a drastic reduction in LWP over the whole domain, barely reaching $100\,\mathrm{g\,m^{-2}}$ (figure 8.8). This represents the daily cycle of LWP in the SEP. Higher values are reached at 13UTC and lower values of LWP at 17 UTC. The model results of $REF7_{sgs}$ show a similar reduction of LWP and therefore a similar behaviour in the daily cycle of LWP. Again showing slightly higher values over the total domain.

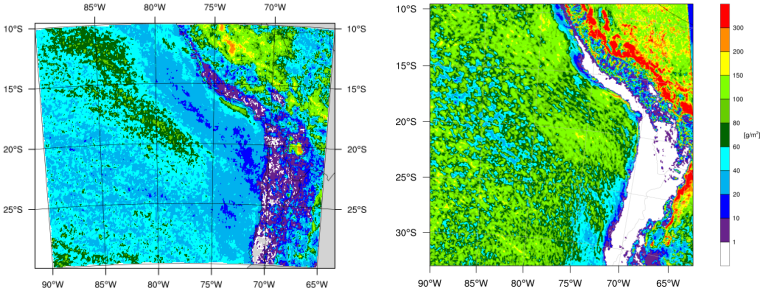

Figure 8.8: 20 day mean of LWP at 17 UTC from observations (left) and $REF7_{sgs}$ (right).

The results of $REF2.8_{sgs}$ and the observations at 13 UTC is shown in figure 8.9. It presents a similar picture like before as the higher values which are occurring in the model results are not seen in the observations. The band of higher LWP at the coast of

Peru (around 18°S and 72°W) is visual in observation as well as in the simulation results. It is also visual that the cloud structures are better resolved in the simulation $REF2.8_{sgs}$ compared to the more coarse simulation of $REF7_{sgs}$.

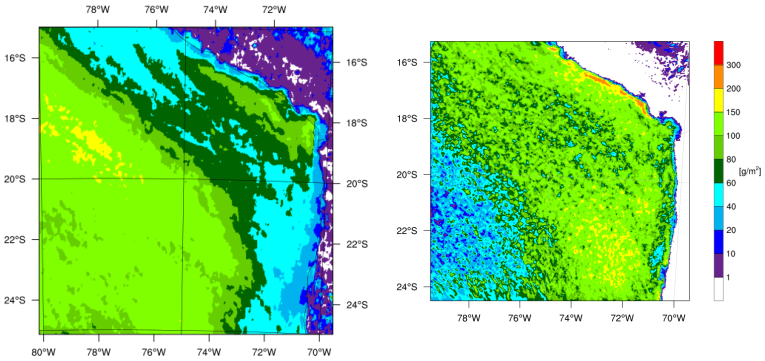

Figure 8.9: 20 day mean of LWP at 13 UTC from observations (left) and $REF2.8_{sgs}$ (right).

The mean LWP at 17 UTC (figure 8.10) reveals the same decline of LWP in observations and model results. The reduction of LWP in the simulation $REF2.8_{sgs}$ is quite similar and there are areas where LWP barely reaching over $100\,\mathrm{g\,m^{-2}}$. But there are also areas where LWP is higher. Again the band with slightly higher values near the coast of Peru is visible, which is slightly visible in the observations. Compared to observation the model results still show slightly higher values of LWP.

All in all the structures are well captured in both simulations compared to observation, while the absolute values are slightly higher in the model results compared to the satellite data. The higher resolved simulation performs better as expected. The daily cycle of LWP is captured well by the model with higher values of LWP in the morning hours and lower values in the afternoon, when the stratocumulus clouds begin to dissolve.

Since the absolute values of LWP are slightly higher in the model compared to observations the relative change of LWP between 13 UTC and 17 UTC is calculated and is shown in figure 8.11 for observations and $REF7_{sgs}$. The observations show regions with a

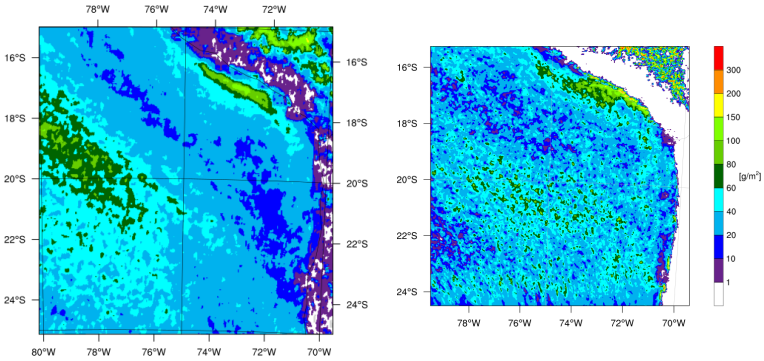

Figure 8.10: 20 day mean of LWP at 17 UTC from observations (left) and $REF2.8_{sgs}$ (right).

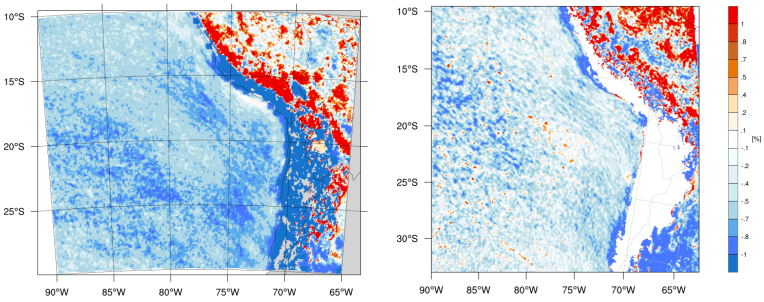

Figure 8.11: Relative change between 13 UTC and 17 UTC of observations (left) and $REF7_{sgs}$ (right).

mean change of -0.2 % to -0.8 % with very high values at the coast reaching -1.0 %. Very similar patterns are visible in $REF7_{sgs}$. Direct at the coast the highest change in LWP is visible. Like in the observations the highest change in LWP in the remote area is visible at around 25°S to 15°S and 90°W and 80°W. The changes are slightly higher in observations than in the model but patterns are similar.

Figure 8.12 shows the relative change of LWP of $REF2.8_{sgs}$ and observations. In this domain the highest changes are right at the

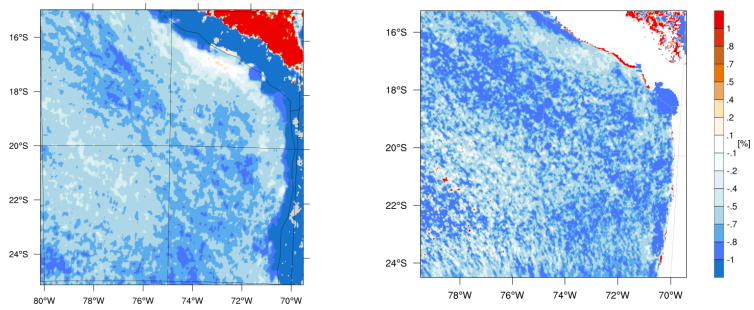

Figure 8.12: Relative change between 13 UTC and 17 UTC of observations (left) and $REF2.8_{sgs}$ (right).

coastline. In the remote area are regions with quite low changes of about -0.2 to -0.4 %. For example near the coast (following the high values direct at the coastline) and more remote around 22°S to 20°S and 79°W to 76°W. But the low values near the coast and the remote area are divided by a structure with higher values of about -0.7 to 0.8 %. This is also reproduced by $REF2.8_{sgs}$ where the highest values are occurring right at the coastline, followed by lower values parallel to the coast. Around 22°S to 20°S and 79°W to 76°W are the lowest changes in the remote area, while this area and the low values near the coast are divided by a band with higher values of relative change. Both features are visible in the observations and the relative change, meaning the daily cycle, is well captured by the model.

Model results ($REF7_{sgs}$ and $REF2.8_{sgs}$) are also compared to data of radiosondes launched from the ship Ron Brown. Figure 8.13 shows the timeseries of the vertical distribution of relative humidity (Hovmöller diagram). The boundary layer height is underestimated in case of $REF7_{sgs}$ and $REF2.8_{sgs}$. The height of the boundary layer is about 300 m higher in the observations than in the simulations. Furthermore at the beginning of the observations until October 28th there are relatively dry areas below 1000 m which are not represented in the model. They are faintly visible in the lowest model levels but the relative humidity is still higher in the simulations (≈70%) compared to observations (below 60%). It seems that the vertical mixing in the model from the surface

is not strong enough to compensate the large-scale subsidence to keep the boundary layer height in a height comparable to the observations. This could also explain the too high values of relative humidity in lower levels of the model results. But the overall structure of the relative humidity within the boundary layer is comparable to observation. The relative humidity is highest (model and observation) at the top of the boundary layer where the stratocumulus clouds are located. All in all the boundary layer structure is well captured by the model results.

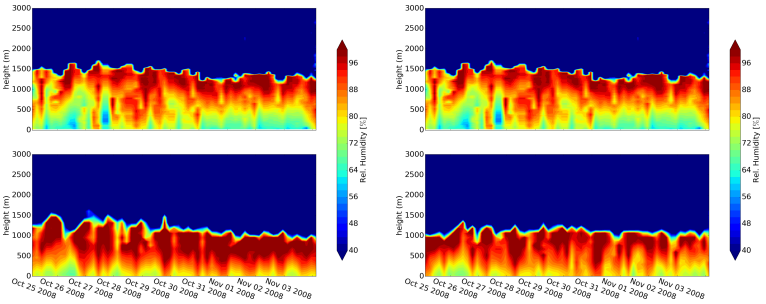

Figure 8.13: Comparison of relative humidity of model results of $REF7_{sgs}$ (left bottom) and $REF2.8_{sgs}$ (right bottom) to data from radiosondes launched from Ron Brown (each top).

During VOCALS-REx research flights along 20°S were conducted and measured properties of cloud droplets (UCAR/NCAR - Earth Observing Laboratory., 2011). Five of this research flights are used to create a mean distribution along the 20°S and compared to the model results. The model results are taken at the same time and position of the aircraft during each research flight. The mean cloud droplet number concentration N_c of simulation $REF7_{sgs}$ and the observations are shown in figure 8.14. The boxplot shows the mean (horizontal line) and the average (red square) of N_c. While the boxes show the 25th and the 75th percentile. The whiskers show the 5th and 95th percentile. The observations are averaged to the grid resolved area. Both observation and model results are divided into four 3° wide segments.

The model compares quite well to the observations and is within the range given by observations. The tendency that high values

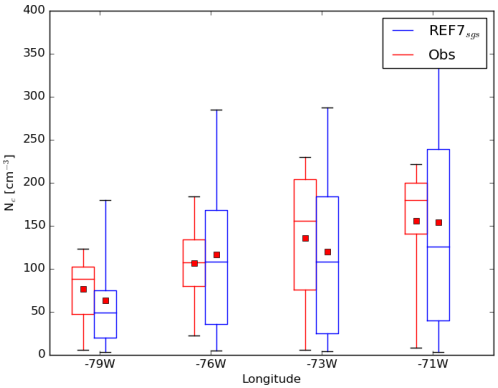

Figure 8.14: Comparison of N_c for $REF7_{sgs}$ with several research flights conducted during VOCALS-REx along 20°S. Red square denotes the average and the vertical line shows the mean of N_c. The boxes show the 25th and 75th percentile. The whiskers show the 5th and 95th percentile.

of N_c are occurring at the coast (71°W), while lower values of N_c are occurring in the remote area over the ocean (79°W) as it is visible in the observation is well captured by the model. In case of $REF7_{sgs}$ the 95th percentile is always higher compared to observations, where the 5th percentile fits most of the time. Far off the coast (79°W) the average and the mean is slightly underestimated, while it fits perfect at 76°W, although 25th and 75th percentiles are underestimated and overestimated respectively. At the coast (71°W) the average fits very well while mean is underestimated, which is due to the fact that also very high values occurring in the model which are not seen in the observations. This gives the hint that in $REF7_{sgs}$ the distribution of N_c is dominated by lower values which is not seen in the observations. On the other hand the average at the coast (71°W) fits quite well. This results from higher values occurring in the simulation which are not present in the observations. All in all $REF7_{sgs}$ compares well to observations.

The higher resolved simulation $REF2.8_{sgs}$ (see figure 8.15) compares much better to observations than $REF7_{sgs}$. Not only that the means and averages of all four segments are fitting better to

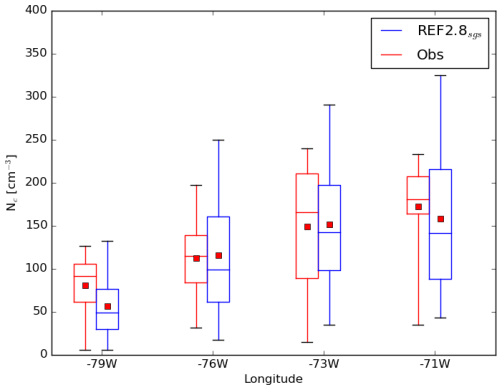

Figure 8.15: Comparison of N_c for $REF2.8_{sgs}$ with several research flights conducted during VOCALS-REx along 20°S. Red square denotes the average and the vertical line shows the mean of N_c. The boxes show the 25th and 75th percentile. The whiskers show the 5th and 95th percentile.

the observations, this is also valid for the 5th and 95th percentile and the 25th and 75th percentiles. The most reasonable cause is the assumption made during calculation of the cloud droplets via a PDF (see chapter 6.3.3). The PDF is depending on grid scale w and modelled TKE. High values of modelled TKE in case of $REF7_{sgs}$ would also lead to higher N_c. It seems that this assumption is better represented in case of $REF2.8_{sgs}$, because TKE and updraught velocities are better represented in the higher resolved simulation. Again at 79°W a slight underestimation of N_c is seen, but the overall distribution of N_c is captured very well in $REF2.8_{sgs}$. The model results compare much better to observations in case of $REF2.8_{sgs}$ than in case of $REF7_{sgs}$.

One further important cloud property is the effective cloud droplet radius r_{eff}. The r_{eff} was also sampled during VOCALS-REx and is displayed together with the results of $REF7_{sgs}$ in figure 8.16. The observations show a slight increase of r_{eff} from coast to open sea. While the mean r_{eff} is about 11 μm at 71°W and nearly 15 μm at 79°W. This is commonly represented by $REF7_{sgs}$. At 71°W the mean of r_{eff} as well as the 25th and 5 percentile are fitting very well to observation while the 95th

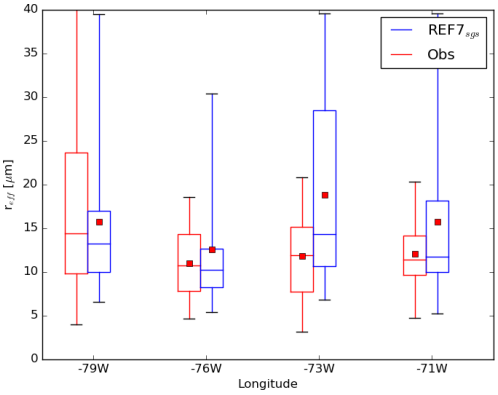

Figure 8.16: Comparison of r_{eff} for $REF7_{sgs}$ with several research flights conducted during VOCALS-REx along 20°S. Red square denotes the average and vertical line the mean of N_c the boxes show the 25th and 75th percentile, while the whiskers show the 5th and 95th percentile.

and the 75th percentile are overestimated. At 73°W the modelled distribution shows a slight overestimation. While at 76°W the model captured the r_{eff} distribution very well, as only the 95th percentile is overestimated. This leads also to an overestimation of the average at this point. In the remote area at 79°W the r_{eff} fits again quite well to observations.

Similar to the findings of N_c $REF2.8_{sgs}$ performs also better in case of r_{eff}. The 5th and 95th percentiles are reaching lower values in case of $REF2.8_{sgs}$ compared to $REF7_{sgs}$. Also r_{eff} fits better to observations, although the mean, 75th and 95th percentile of r_{eff} are slightly underestimated and the 5th percentile is slightly overestimated for all cases. The 25th percentile fits quite well in all cases except for 71°W. The overall distribution along 20°S is captured very well by $REF2.8_{sgs}$.

Wyant et al. (2015) showed that the simulation of stratocumulus clouds are a challenging task for numerical models, even for mesoscale models. However COSMO-ART could show that it is able to represent the main characteristics of stratocumulus clouds in the SEP. Although boundary layer height is slightly underestimated, cloud properties, like LWP, cloud droplet number

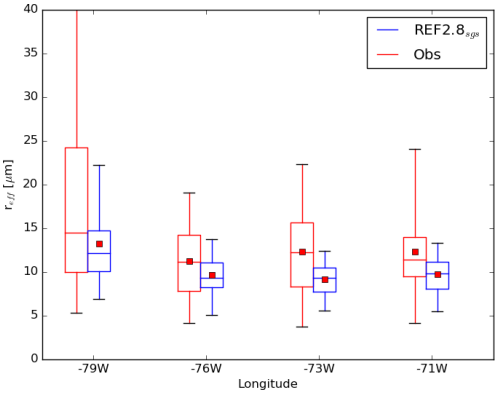

Figure 8.17: Comparison of r_{eff} for $REF2.8_{sgs}$ with several research flights conducted during VOCALS-REx along 20°S. Red square denotes the average and vertical line the mean of N_c the boxes show the 25th and 75th percentile, while the whiskers show the 5th and 95th percentile.

concentration N_c and effective radius r_{eff} are represented very well. Additionally COSMO-ART performs well for both grid sizes (7 km and 2.8 km), which is an important aspect since the coarser resolution covers a reasonable large domain to investigate impacts of MCB.

9 Impact of Climate Engineering

In this chapter the impacts of purposely released sea salt particles on cloud optical properties and radiation will be investigated. Latham et al. (2008) suggested that the seeding of stratocumulus clouds for climate engineering could be carried out by sea spraying ships. Therefore the model simulations are carried out by adding an additional sea salt flux into the lowest model layer. The extra sea salt flux is discussed in detail in chapter 6.1.2. The following chapter is divided into two parts. In the first part the impact on cloud properties like cloud droplet number concentration N_c and effective radius r_{eff}will be discussed. The second part will focus on radiative impact caused by seeding.

To evaluate the impact of different sized particles different seeding scenarios are carried out, where the size of the seeding particles is varied.

Seeding scenarios

The seeding scenarios discussed in the following consider seeding with small and large sea salt particles with a constant emission flux. The first scenarios consider seeding with small particles, where additional see salt particles are released to sea salt mode sa of COSMO-ART and are conducted for both grid sizes ($CEA7_{sgs}$ & $CEA2.8_{sgs}$). Therefore the seeding particles have a initial size range of 0.02 to 1 μm with an initial mean diameter of 0.2 μm.

The second seeding scenario with larger particles ($CEB2.8_{sgs}$) consider the same constant flux as for the smaller seeding particles, but the additional see salt particles are released to sea salt mode sb of COSMO-ART. Therefore the seeding particles have an initial size range of 1 to 9 μm with an initial mean diameter of 2.0 μm. Note that this experiment is only conducted in the nested domain.

In a further scenario the seeding sea salt particles are released to both modes but only conducted for the domain with 7 km resolution ($CEAB7_{sgs}$). The total emission flux is of the same magnitude like in the other scenarios, but the number flux is weighted 50% to each mode.

After the additionally added sea salt particles are injected they are treated like natural sea salt.

9.1 Impact on Cloud Properties

The intention of seeding is to change cloud properties in a way as it is discussed in chapter 5. Climate engineering intends to increase the cloud droplet number concentration N_c and to reduce the cloud droplet effective radius r_{eff}.

Therefore an exemplary look on changes of N_c, r_{eff}, cloud liquid water content LWC and hourly precipitation HP of simulation $CEA2.8_{sgs}$ ($CEA7_{sgs}$ looks quite similar) is taken. The timeseries of the areal mean of the cloud droplet effective radius r_{eff} (a), the cloud droplet number concentration N_c (b), the cloud water content LWC (c), and the hourly precipitation HP (d) are shown in figure 9.1, where only points over ocean are taken into account. Only a short period is shown to show exemplary the changes of each property. Blue areas denote that values are lower in the CE simulation while reddish areas denote that values are higher in the CE simulations.

The impact on cloud properties by the additional seeding flux on sea salt mode sa is quite obvious. r_{eff} is substantially lower in $CEA2.8_{sgs}$ compared to $REF2.8_{sgs}$ (about 1 μm lower). This is accompanied by an increase of N_c. Both is expected according to the Twomey effect. N_c is increased in this small period by $\approx 20\,cm^{-3}$, which also means an increase of $\approx 15\,\%$. The increase of N_c originates from the increase of available CCN.

There is also a decrease of hourly precipitation HP, which can be interpreted by the Albrecht effect. Since the overall size of the cloud droplets decreased the autoconversion process is reduced and therefore precipitation is suppressed by an increase of N_c. The results show also an increase in LWC, which is not stated by the classical theory of the Twomey effect. The theory assumes a constant LWC and the simulations show that it does not stay

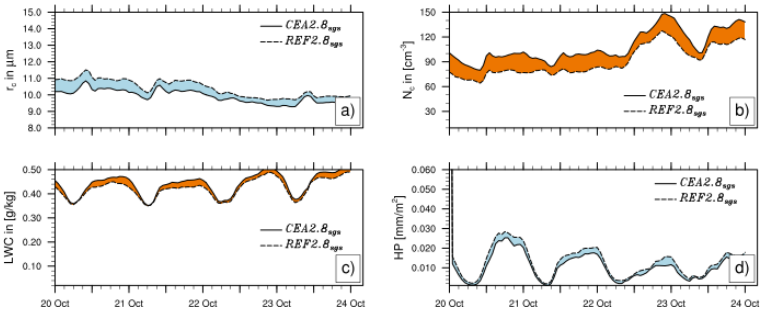

Figure 9.1: Comparison of cloud properties between $REF2.8_{sgs}$ and $CEA2.8_{sgs}$. Displayed is a) cloud droplet effective radius r_{eff}, b) cloud droplet number concentration N_c, c) cloud water content LWC, d) hourly precipitation HP.

constant. LWC shows a daily cycle, which was already seen in the comparison to observations in the previous chapter. In both simulations LWC and HP follow a similar daily cycle, while N_c and r_{eff} do not follow a distinct daily cycle. Additionally the lowest rates of HP (from Oct 23rd on) are related to the highest amount of N_c and lowest r_{eff}, where on the other side LWC is slightly higher in this period. The distinctive daily cycle of LWC and HP is not changing due to cloud seeding.

For each simulation it is identifiable that if LWC is increasing also HP is increasing (with a certain delay) and if LWC is decreasing also HP is decreasing (again with a certain delay), so that HP is following LWC. Even for the periods of 21st, 22nd and 24th an slight increase in r_{eff} can be observed and indicates that an increase in the size of cloud droplets can promote or initiate precipitation processes.

The same data is binned into several intervals of N_c and the corresponding LWC and r_{eff}. Figure 9.2) shows the results in case of $REF2.8_{sgs}$ and $CEA2.8_{sgs}$. The number in brackets gives the amount of data points of each interval. In general the largest values of r_{eff} are accompanied by low values of N_c and mostly by low values of LWC. Smaller values of r_{eff} are accompanied by larger values of N_c and LWC. In case of constant N_c LWC is the

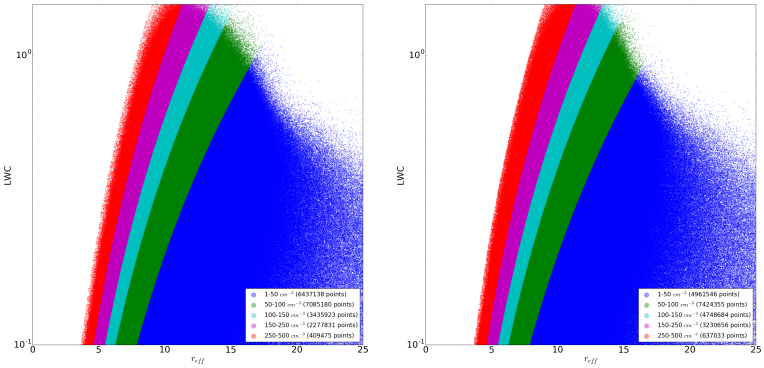

Figure 9.2: Scatter plot of liquid water content and effective cloud droplet radius r_{eff} for $REF2.8_{sgs}$ (left) and $CEA2.8_{sgs}$ (right).

dominant factor determining r_{eff}. Higher values of LWC leading to an increase of r_{eff}.

Comparing $REF2.8_{sgs}$ to $CEA2.8_{sgs}$ the number of data points in the interval of 1-50 cm^{-3} is decreasing while the number is increasing in all other intervals. There is also an increase of higher values of LWC which indicates that suppressed precipitation is leading to higher values of LWC. The number of data points in the interval 1-50 cm^{-3} is changing by -23%, while 50-100 cm^{-3} is changing by 5%, 100-150 cm^{-3} by 38%, 150-250 cm^{-3} by 41% and 250-500 cm^{-3} by 55% and therefore the interval with the highest N_c experiences the largest relative increase. This proves a positive impact on cloud properties due to seeding. The seeding leads to the intended effects of MCB as N_c is increased and r_{eff} is decreased.

Seeding with larger particles (additional flux on sea salt mode sb, $CEB2.8_{sgs}$) shows a different behaviour. The timeseries of $CEB2.8_{sgs}$ is compared to $REF2.8_{sgs}$ in figure 9.3. It is obvious that for all properties the effect of CE is reversed compared to the effects of $CEA2.8_{sgs}$. In case of $CEB2.8_{sgs}$ r_{eff} is increased, while N_c is lower compared to $REF2.8_{sgs}$. It is accompanied by a decrease of LWC and an increase of HP. This is due to the fact that the larger sea salt particles are activated faster to cloud droplets compared to smaller particles. This leads to larger cloud

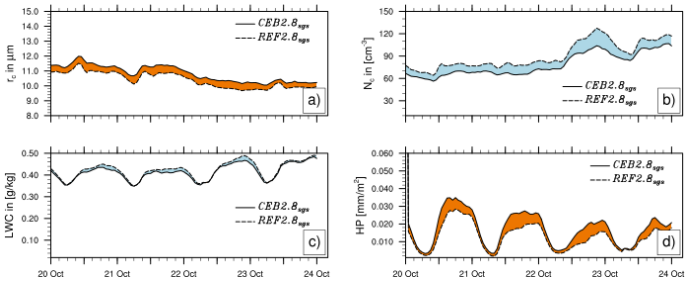

Figure 9.3: Comparison of cloud properties between $REF2.8_{sgs}$ and $CEB2.8_{sgs}$. Displayed is a) cloud droplet effective radius r_{eff}, b) cloud droplet number concentration N_c, c) cloud water content LWC, d) hourly precipitation HP.

droplets but with lower number concentration. The larger cloud droplets are able to initiate precipitation processes much earlier and therefore precipitation is enhanced. This is obvious in the increase of HP in figure 9.3 d) where precipitation is increasing faster in $CEB2.8_{sgs}$ than in $REF2.8_{sgs}$. The higher precipitation rate leads also to a lower LWC. The outcome of $CEB2.8_{sgs}$ shows the opposite of the intended effect - a 'negative' Twomey effect.

The impact of the size of the injected particles is also seen in the 2D histograms of N_c and r_{eff} which are shown in figure 9.4 for all three simulations. The top figure shows the histogram of $REF2.8_{sgs}$ where the mean effective radius $\overline{r_{eff}}$ is around $10.1\mu m$ and mean cloud droplet number concentration $\overline{N_c}$ is around $60cm^{-3}$. The standard deviation of r_{eff} is $\sigma_{r_{eff}} = 3.185$, while the standard deviation of N_c is $\sigma_{N_c} = 69.6$. The ellipse within the 2D histogram highlights the properties of the distribution. The midpoint of the ellipse is at the mean of both distributions and the semi-major and semi-minor axis indicates the standard deviation σ of each distribution. The results of $REF2.8_{sgs}$ are indicated as white ellipse in the 2D histograms for both CE simulations.

The 2D histogram of $CEA2.8_{sgs}$ is shown in figure 9.4 on the bottom left side. Although the histogram looks similar to that one of $REF2.8_{sgs}$ it is identifiable that more values occurring at $N_c > 320cm^{-3}$. This is also indicated by the ellipse, because it shifts towards lower values of r_{eff} and larger values of N_c.

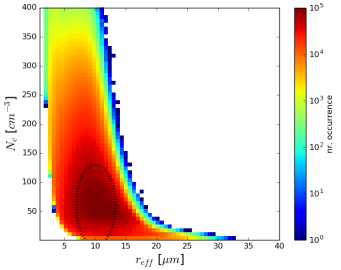

$REF2.8_{sgs}$

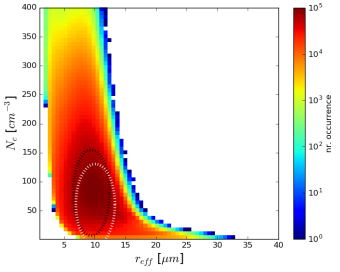

$CEA2.8_{sgs}$

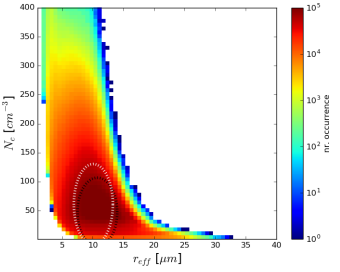

$CEB2.8_{sgs}$

Figure 9.4: 2D Histogram N_c and r_{eff}. The midpoint of the ellipse shows the mean of each distribution and the semi-major axis and semi-minor axis indicates the standard deviations of each distribution. The white ellipse in the bottom figues is the ellipse from $REF2.8_{sgs}$.

The $\overline{r_{eff}}$ is shifted to $\overline{r_{eff}}$=9.45 $\mu\,m$ and $\overline{N_c}$ = 74.2 cm^{-3}, while $\sigma_{r_{eff}}$ = 3.07 and σ_{N_c} = 65.7. There is a decrease in variance of both quantities in case of seeding with smaller particles. The 2D histogram shows also an increase of N_c while r_{eff} is decreasing and again it shows the effects which are intended by MCB.

The 2D histogram of $CEB2.8_{sgs}$ is shown in figure 9.4 on the bottom right side. The occurrence of high values of N_c (above 300 cm^{-3}) is reduced. This underlines the fact that seeding with larger particle is decreasing N_c. Additionally $\overline{r_{eff}}$ = 10.75 μm which is an increase compared to $REF2.8_{sgs}$. In addition $\overline{N_c}$ = 54.2 cm^{-3} which is a decrease by 10% compared to $REF2.8_{sgs}$. This again shows that seeding unsuitable large particles can lead to unwanted effects. Namely a decrease in N_c and an increase in r_{eff} which is not intended by MCB. The results of $CEB2.8_{sgs}$ underline that the size of the emitted additional particles are essential to the outcome of MCB.

To underline the thesis that the larger particles are activated faster to cloud droplets than smaller particles the 2D histograms of vertical velocity and the maximum supersaturation s_{max} reached during activation are plotted in figure 9.5 for the three simulations $REF2.8_{sgs}$, $CEA2.8_{sgs}$ and $CEB2.8_{sgs}$. Only points are taken into account where cloud activation occurred in the model.

For all three simulations a core area at a vertical velocity of $\approx$ 0.1 - 0.2 $m\,s^{-1}$ and $s_{max} \approx$ 0.1 - 0.2 % is identifiable. But more interesting are the highest values of s_{max} reached during the simulation. Although the 2D histograms are looking quite similar in case of $REF2.8_{sgs}$ and $CEA2.8_{sgs}$ the branch that reaching from $\approx 0.8\,m\,s^{-1}$ and $\approx$ 0.8 % to higher values is more pronounced in $REF2.8_{sgs}$ than in $CEA2.8_{sgs}$. This means that the additional sea salt particles of mode sa are lowering the maximal supersaturation reached during the activation process. As the additional particles are activated to cloud droplets the supersaturation is decreased by depletion of water vapour onto the formed cloud droplets. Very small particles which could be activated in $REF2.8_{sgs}$ are not activated in $CEA2.8_{sgs}$, if their critical supersaturation is higher than s_{max} reached during $CEA2.8_{sgs}$. Of course this should be most valid for the area near the coast, because this area is dominated by high number concentrations of anthropogenic aerosols, which are usually smaller than the sea salt particles.

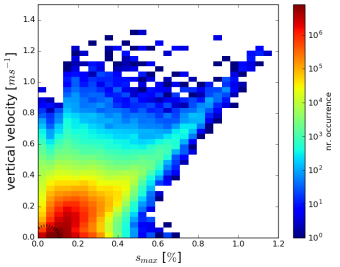

$REF2.8_{sgs}$

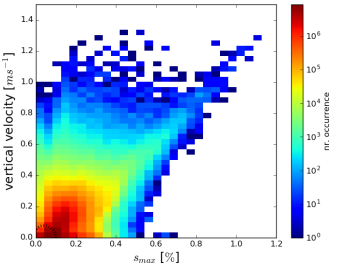

$CEA2.8_{sgs}$

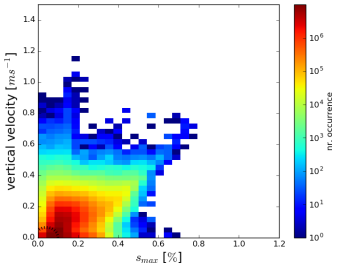

$CEB2.8_{sgs}$

Figure 9.5: 2D Histogram of vertical velocity and maximum supersaturation s_{max}.Only points were cloud activation took place are taken into account.

In case of $CEB2.8_{sgs}$ the impact on s_{max} is even larger. In this case s_{max} is decreased much more than in case of $CEA2.8_{sgs}$ and unlike in $CEA2.8_{sgs}$ s_{max} does not reach a value greater than 0.8 %. Since the seeding particles in $CEB2.8_{sgs}$ are larger they are activated in an earlier state to cloud droplets than smaller aerosol particles, like anthropogenic aerosol. They are also much faster activated then the smaller seeding particles used in $CEA2.8_{sgs}$. Supersaturation is decreased much more in case of $CEB2.8_{sgs}$ than in case of $CEA2.8_{sgs}$ because more water vapour is depleted on the newly formed cloud droplets. This of course has a large impact on cloud droplet formation. s_{max} is that low, that it is nearly impossible for very small aerosol particles to form cloud

droplets, although it would be possible for them to form a cloud droplet without CE.

This shows the importance of the size of the seeding particles in case of MCB. Because the wrong size could lead to the opposite effect ('reversed Twomey effect') of the original intended effect.

Susceptibility

Stevens and Feingold (2009) defined the precipitation susceptibility of clouds to an aerosol perturbation. This is a measure how the rain rate changes on a change of cloud droplet number concentration. Following this approach the susceptibility β_{N_c} will be defined. This is the susceptibility of N_c due to changes of sea salt particles and is defined as following:

$$\beta_{N_c} = \frac{\ln(N_{c,CE}) - \ln(N_{c,REF})}{\ln(N_{seas,CE}) - \ln(N_{seas,REF})} \tag{9.1}$$

where $N_{c,x}$ denotes the cloud droplet number concentration and $N_{seas,x}$ the number concentration of the sea salt particles. $x = CE$ denote the climate engineering simulation and $x = REF$ the baseline simulation. The susceptibility β_{N_c} is an indicator of the efficiency of MCB. Positive values indicate a positive effect (increase) on N_c due to seeding particles, while negative values indicate a negative effect (decrease) on N_c. Figure 9.6 shows the mean β_{N_c} over the total time period of simulation $REF7_{sgs}$ and $CEA7_{sgs}$.

A large area of the domain is covered by positive values of β_{N_c}. But there are also areas with low values of β_{N_c} close to zero, which indicates that seeding is not effective. Positive values of β_{N_c} are dominant in the remote areas of the ocean and it indicates that seeding is effective in these parts of the domain, which is accompanied by an increase of N_c. However along the coast are values occurring, which are close to zero. This indicates that seeding along the coast is not very effective since N_c is not changed very much. The assumption is that there must be already high N_c occurring without seeding, because providing additional CCNs does not change N_c much. There must be taking place competing effects between the seeded sea salt particles and most probably anthropogenic aerosols.

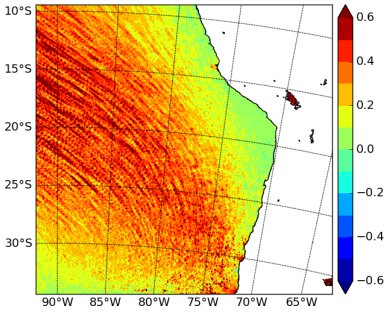

Figure 9.6: Susceptibility β_{N_c} for $CEA7_{sgs}$.

This is pointed out by the mean distribution of the anthropogenic aerosols (figure 9.7) as it shows that the highest values of anthropogenic aerosol are occurring at the coast. Very high values are located at the coast of Chile as well as in the northern coastal region of the domain at the coast of Peru. In this regions the effect on enhancement of N_c is reduced, because the seeding particles are activated prior to the anthropogenic particles, because the latter are mostly smaller than the seeding particles. As the seeded particles are being activated they lower the overall supersaturation and smaller particles can not be activated any more. Therefore the effectiveness of MCB is reduced in regions with high anthropogenic aerosol concentrations.

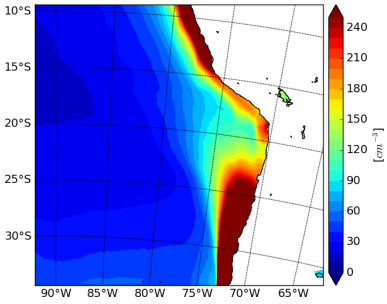

Figure 9.7: Aerosol number concentration for $CEA7_{sgs}$.

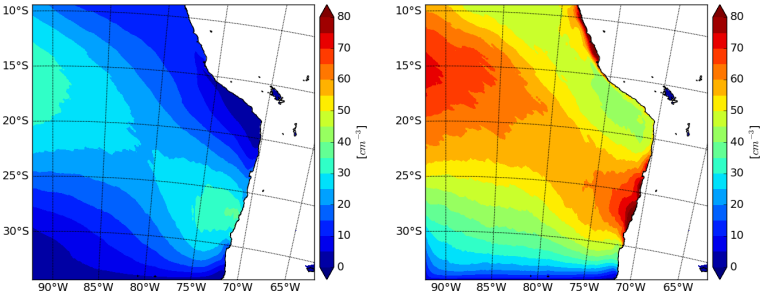

Figure 9.8: Horizontal distribution of sea salt particles (mode sa) for $REF7_{sgs}$ (left) and $CEA7_{sgs}$ (right)

The mean increase of sea salt particles (mode sa) due to seeding is seen in figure 9.8 in case of $CEA7_{sgs}$. The natural distribution without CE is on the left side while with seeding is on the right side. Sea salt particles are nearly doubled in most areas. Additionally the highest values of sea salt in case of $CEA7_{sgs}$ are occurring between 20°S and 10°S and around 90°W, where the highest values of β_{N_c} are located. In this scenario this area would be most suitable to be targeted for seeding.

A very similar picture is seen in case of $CEA2.8_{sgs}$ where β_{N_c} is shown in figure 9.9. The susceptibility β_{N_c} is increased most in the more remote area of the domain. Near the coast there is nearly no impact on N_c due to the seeding as β_{N_c} is near to zero. This also corresponds to the distribution of anthropogenic aerosol which is shown in figure 9.10. Here most of the anthropogenic aerosol is located along the coast of Chile and Peru but decreases offshore. With increasing distance to the coast the conditions are becoming more pristine.

The largest increase of sea salt (mode sa) in the domain of $CEA2.8_{sgs}$ (figure 9.11) is located north of 20°S. The distinct increase of sea salt near the coast of Peru does not have any positive impacts on β_{N_c}, since the coastal region is dominated by a high amount of anthropogenic aerosol. This lowers the efficiency of MCB.

Figure 9.12 shows β_{N_c} in case of $CEB2.8_{sgs}$. According to equation 9.1 the calculation of β_{N_c} takes in this case the number concentration of sea salt mode sb into account. Seeding with

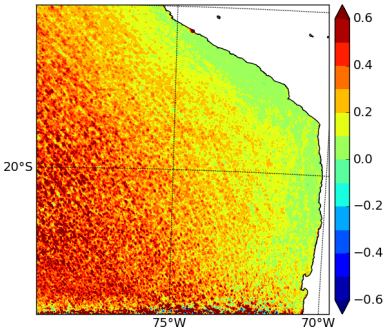

Figure 9.9: Susceptibility β_{N_c} for $CEA2.8_{sgs}$.

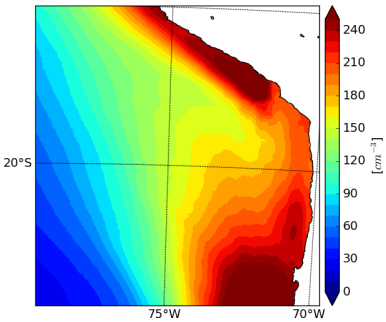

Figure 9.10: Aerosol number concentration for $CEA2.8_{sgs}$.

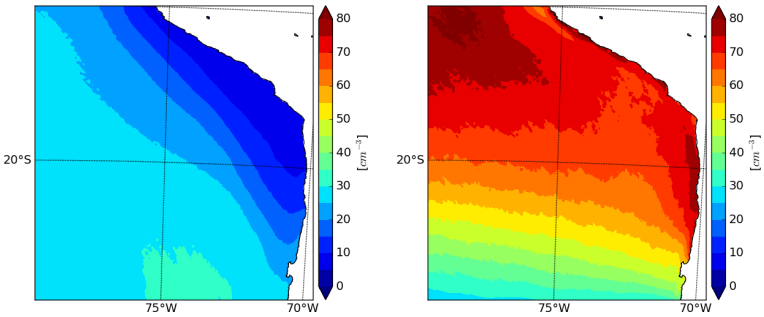

Figure 9.11: Horizontal distribution of sea salt particles (mode sa) for $REF2.8_{sgs}$ (left) and $CEA2.8_{sgs}$ (right)

larger particles shows that the efficiency of MCB on cloud droplets is nearly zero over the total domain. The remote area in the northern part of the domain shows slight positive values. But the values around 0.1 are not comparable to the positive values of β_{N_c} in case of $CEA2.8_{sgs}$, which reached values around 0.6. In the southern part of the domain near the coast there are values near zero and slightly negative of about -0.1 are occurring. This area is dominated by anthropogenic aerosol (compare figure 9.10). High anthropogenic aerosol concentration lead to high values of N_c in case of $REF2.8_{sgs}$. The seeded larger particles are activated earlier to cloud droplets than the anthropogenic aerosol. As already shown the larger particles are decreasing supersaturation and therefore the anthropogenic particles are not able to activate to cloud droplets. This leads to a reduction of N_c in case of $CEB2.8_{sgs}$.

The conclusion is that seeding with larger particles is quite insufficient. On the other side seeding with smaller particles is more sufficient but with restraints. Seeding with small particles is only effective in areas with low amount of preexisting aerosols (for example anthropogenic aerosol).

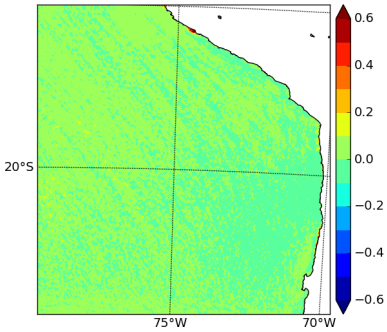

Figure 9.12: Susceptibility β_{N_c} for $CEB2.8_{sgs}$.

9.2 Impact on Radiation

Since radiation is the main target of MCB now the impacts on radiation will be quantified. The following chapter is divided into three parts, where three different scenarios are investigated, namely seeding with small particles, large particles and small and large particles.

Seeding with small particles

The discussed scenarios are $CEA7_{sgs}$, $CEA7_{nosgs}$,$CEA2.8_{sgs}$ and $CEA2.8_{nosgs}$. In these scenarios cloud seeding is conducted with extra particles on the smallest sea salt mode sa.

If not other stated the horizontal plots will show the temporal mean of 25 days. Timeseries will only show a smaller time period for exemplary explanation of the changes in radiation.

The temporal mean difference $CEA7_{sgs} - REF7_{sgs}$ of short-wave radiation L_s and long-wave radiation L_l at the surface is shown in figure 9.13.

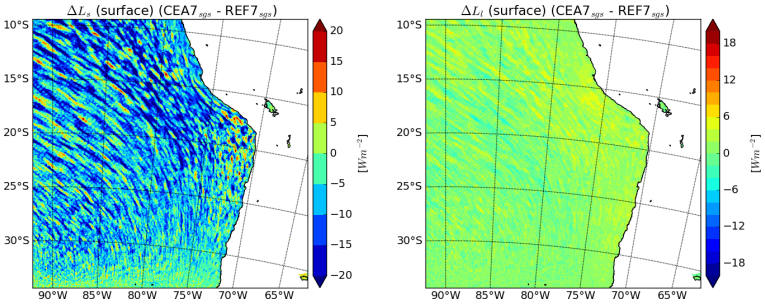

Figure 9.13: Impact on surface short-wave radiation (left) and long-wave radiation (right) for $CEA7$ - $REF7$ at the surface. Only grid points over water are taken into account.

There are certain areas with a reduction of L_s at the surface. The areas with the highest reductions of roughly -20 $\mathrm{W\,m^{-2}}$ are located around 20°S and 80°W. But there are also areas which are showing positive radiative forcing of more than 15 $\mathrm{Wm^{-2}}$. Downstream of the Chilean anthropogenic plume (20°S and 73°W) areas with positive forcing are visible. Those regions with positive

values are mostly located along the coast but there are also regions with positive values in the remote area. There is no homogeneous change in L_s at the surface, as also positive forcings in regions far away from the coast are occurring. This clearly shows non-linear processes, so that increasing CCN does not necessarily lead to a homogeneous increase in N_c , which would lead to a uniform decrease in L_s. Although it is expected that an increase of CCN in an already polluted environment would not necessarily lead to an increase in N_c and hence to a reduction of L_s. But it shows that negative effects are occurring. In this case this means an increase in L_s. Furthermore the result shows that an increase in CCN in an area with pristine conditions does not necessarily lead to a decrease in L_s.

The overall reduction of L_s is about -9 $\mathrm{W\,m^{-2}}$ in case of $CEA7_{sgs}$ - $REF7_{sgs}$. The overall structure looks quite similar for $CEA7_{nosgs}$ - $REF7_{nosgs}$ (not shown here), but the reduction of L_s is only about -7.35 $\mathrm{W\,m^{-2}}$. The deviation shows that it is necessary to include ACI also for subgrid scale clouds.

The right side of figure 9.13 shows the difference in L_l at the surface and a faint dipole character is visible, with increased values near the coast and nearly none to slightly decreased values in the remote area over the ocean. The largest decrease in L_s is located where the highest increase in L_l is to be found. There is a slight increase in L_l of about +0.35 $\mathrm{W\,m^{-2}}$ in case of $CEA7_{nosgs}$, and for $CEA7_{nosgs}$ there is only a slight increase in L_l of 0.1 $\mathrm{W\,m^{-2}}$.

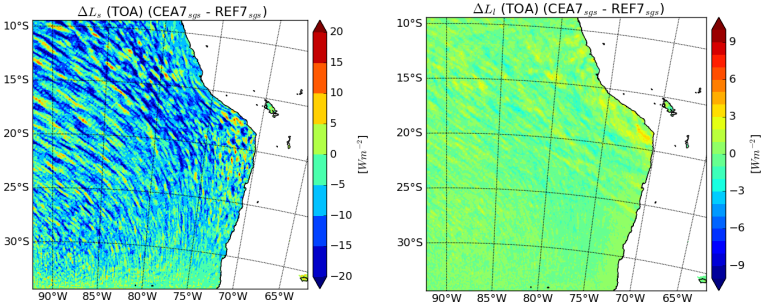

Figure 9.14: Impact on short-wave radiation (left) and long-wave radiation (right) for $CEA7$ - $REF7$ at top of the atmosphere (TOA). Only grid points over water are taken into account.

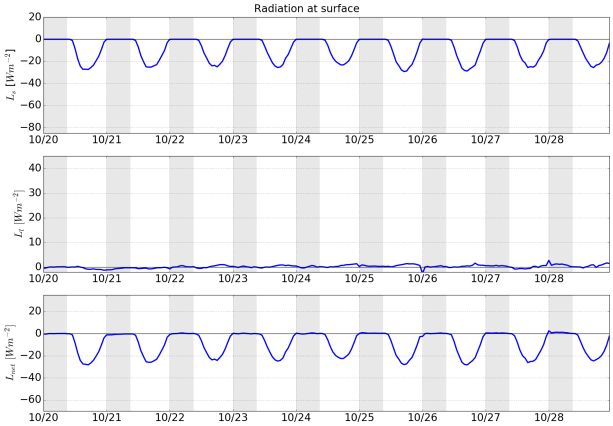

Figure 9.15: $REF7_{sgs}$ - $CEA7_{sgs}$Timeseries of short-wave (top), long-wave(middle), and net (bottom) radiation at surface. Only grid points over ocean are taken into account.

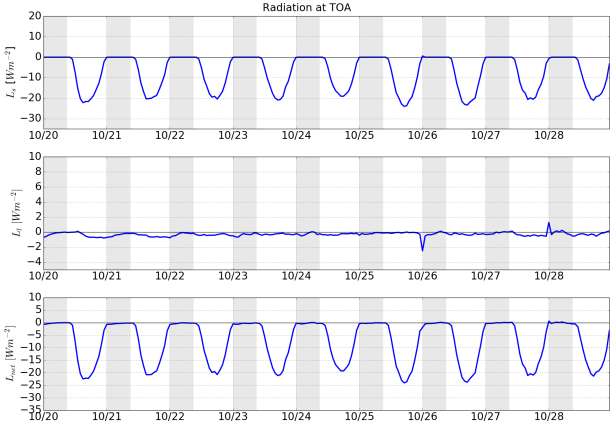

Figure 9.16: $REF7_{sgs}$ - $CEA7_{sgs}$Timeseries of short-wave (top), long-wave(middle), and net (bottom) radiation top of the atmosphere (TOA). Only grid points over ocean are taken into account.

Figure 9.14 shows the horizontal mean of long- and short-wave radiation at top of the atmosphere (TOA). The horizontal patterns

are quite identical. The total reduction of short-wave radiation L_s at TOA is -7.5 W m^{-2} (-6.1 W m^{-2} for $CEA7_{nosgs} - REF7_{nosgs}$) and the long-wave radiation L_l is reduced by -0.23 W m^{-2} (-0.06 W m^{-2} for $CEA7_{nosgs} - REF7_{nosgs}$). The changes are slightly smaller at TOA than at the surface.

The timeseries of the areal mean of L_s (top), L_l (middle) and the net effect of long- and short-wave radiation L_{net} (bottom) at the surface is shown in figure 9.15, where night time is indicated by the shaded area. The reduction is quite uniform over time, since the amplitudes of the peaks are not fluctuating largely. All of them showing a similar minimum. Since the variation is not large over time, only a short period is shown. Obvious is the largest decrease during daytime and peaks at midday. The timeseries at TOA shows the same behaviour (figure 9.16). Although the amount is slightly smaller compared to the surface (the scale of the ordinate is different compared to the plot for surface radiation).

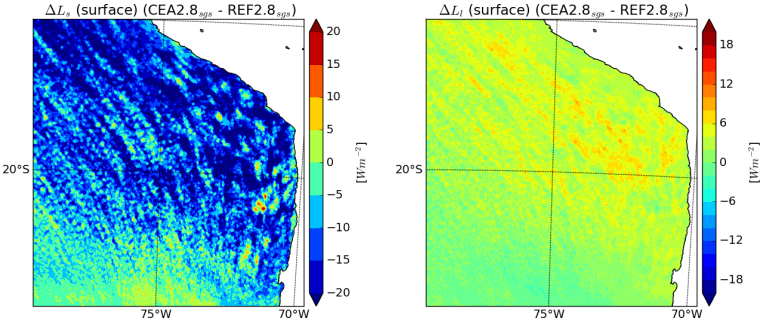

Figure 9.17: Impact on surface short-wave radiation (left) and long-wave radiation (right) for $CEA2.8$ - $REF2.8$. Only grid points over water are taken into account.

The result of the horizontal mean of the smaller, but higher resolved domain ($CEA2.8_{sgs}$ - $REF2.8_{sgs}$) is shown in figure 9.17. L_s is reduced by a mean value of -11.3 W m^{-2} in case of $CEA2.8_{sgs}$ and by -9.9 W m^{-2} in case of $CEA2.8_{nosgs}$. Although β_{N_c} showed that seeding is not very effective on changing N_c in the northern coastal area (figure 9.9) L_s shows quite high reductions in this part of the domain. As the northern part of the domain is characterized by low wind speeds, it results in a low amount of natural sea

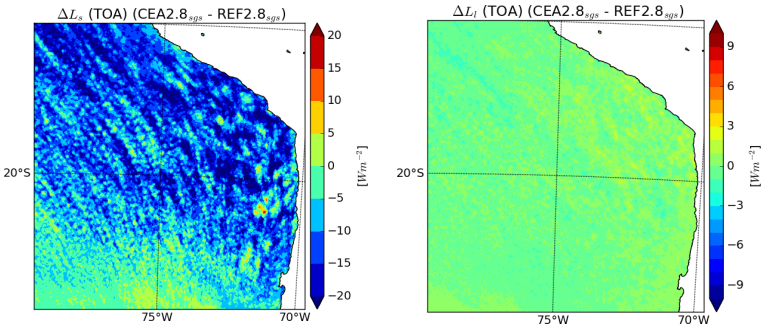

Figure 9.18: Impact on short-wave radiation (left) and long-wave radiation (right) for $CEA2.8$ - $REF2.8$ at top of the atmosphere (TOA). Only grid points over water are taken into account.

salt particles in the air, because natural sea salt emissions are a function of the wind speed. On the other side the northern domain is dominated by the highest increase of sea salt particles due to seeding (figure 9.11). Therefore the effect on L_s results from the direct effect on radiation due to an increase in sea salt particles. The southern part of the domain shows an overall positive forcing and only less negative forcing. But like before there is no uniform reduction in short-wave radiation and showing non-linear effects.

Long-wave radiation L_l in figure 9.17 shows a similar behaviour as in case of the larger domain. The strongest increase in long-wave radiation is located where the highest decrease in L_s is found, here in the vicinity of the coast. This indicates that the decrease in L_s is accompanied by an increase of L_l and therefore the total effect of seeding is partially compensated. The mean of L_l is $+1.9\,\mathrm{W\,m^{-2}}$ in case of $CEA2.8_{sgs} - REF2.8_{sgs}$ and +1.6 in case of $CEA2.8_{nosgs} - REF2.8_{nosgs}$.

Short-wave radiation L_s and long-wave radiation L_l at TOA is shown in figure 9.18. The structure is similar to that of the surface, while the amount is lower compared to surface changes. The mean change in short-wave radiation is about -9.9 $\mathrm{W\,m^{-2}}$ (-8.7 $\mathrm{W\,m^{-2}}$ for $CEA2.8_{nosgs} - REF2.8_{nosgs}$). The patterns of L_l are looking similar but the difference of long-wave radiation is lower at TOA (note also the different scale in case of TOA). At TOA L_l

is reduced by -0.32 W m^{-2} (-0.27 W m^{-2} in case of $REF2.8_{nosgs}$). Which mean that less long-wave radiation is reaching into space.

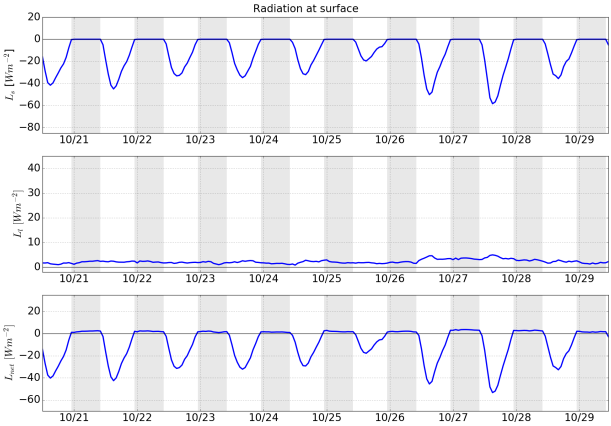

Figure 9.19: $REF2.8_{sgs}$ - $CEA2.8_{sgs}$Timeseries of short-wave (top), long-wave(middle), and net (bottom) radiation at surface. Only grid points over ocean are taken into account.

The timeseries of radiation in case of $CEA2.8_{sgs}$ (figure 9.19) shows a similar impact as in case of $CEA7_{sgs}$. In case of $CEA2.8_{sgs}$ the reduction of L_s is like in the coarser domain obviously during daytime. But in case of the higher resolved domain there is no such uniform reduction in L_s as in $CEA7_{sgs}$. This is due to the fact that the smaller domain is more dominated by the variation of anthropogenic aerosol, which is advected through the domain. This can be for example seen during October 25th where the maximum reduction is only about -20 W m^{-2}, while later on October 27th the reduction is about -60 W m^{-2}. This again indicates that MCB is only effective in the absence of an abundant number of preexisting aerosols. L_l is uniformly increased by about +3 to +4 W m^{-2}. This increase is due to radiative impact of the additional sea salt itself. The increase in L_l is higher in the smaller domain because the mean content of natural sea salt is smaller compared to the coarser but larger domain. At the end the increase in L_l does only have a minor impact on L_{net}, although it should not be neglected.

The timeseries at TOA (figure 9.20) looks similar but the amount of reduction is lower compared to the surface, as some amount of

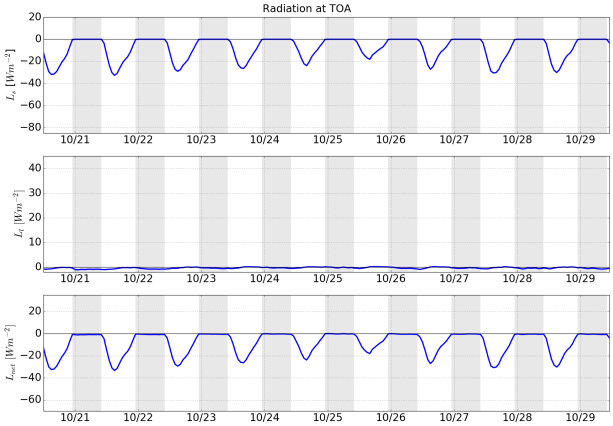

Figure 9.20: $REF2.8_{sgs}$ - $CEA2.8_{sgs}$Timeseries of short-wave (top), long-wave(middle), and net (bottom) radiation at surface. Only grid points over ocean are taken into account.

the reflected short-wave radiation is absorbed within the atmosphere. The change in L_l is nearly negligible, although it is slightly negative.

Seeding with larger particles

Larger particles are assumed to be inadequate for seeding. This could already be shown in the prior chapter since N_c was reduced due to seeding with larger particles. Therefore only one simulation ($CEB2.8_{sgs}$ was conducted where MCB is carried out with larger particles. In this case particles are added on the sea salt mode sb.

In chapter 9.1 it is shown that seeding with larger particles ($CEB2.8_{sgs}$) is leading to the opposite of the intended effect of MCB by lowering N_c. Although the same amount of sea salt particles are added as in case of $CEA2.8_{sgs}$. This is now further investigated and the impact on radiation is shown. Although there is a large negative impact on L_s at the surface (left side of figure 9.21), there is also a large impact on L_l (right side of figure 9.21) in case of $CEB2.8_{sgs}$. The change in L_s is about -13.3 $\mathrm{W\,m^{-2}}$ which is larger compared to the change in L_s in case of $CEA2.8_{sgs}$.

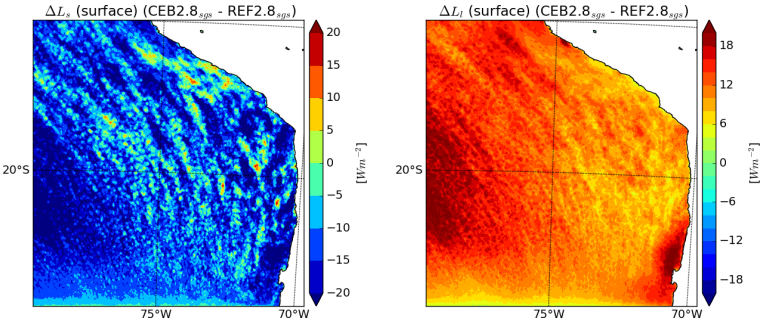

Figure 9.21: Impact on surface short-wave radiation (left) and long-wave radiation (right) for $CEB2.8$ - $REF2.8$. Only grid points over water are taken into account.

But also a large increase in L_l at the surface is caused by the seeded sea salt particles. The change in L_l is about $10.8\,\mathrm{W\,m^{-2}}$ and nearly compensates the negative forcing of L_s. At first this seems contradictory, because a decrease in N_c and a decrease in cloud amount due to a decrease in cloud liquid water is expected to decrease long-wave radiation. Additionally incoming short-wave radiation would be increased. But this would be the case if only the impact of changes in cloud properties are taken into account, together with the neglect of direct aerosol radiation interaction. In this case changes in sea salt properties. In case of $CE2.8_{sgs}$ the direct effect on radiation of larger sea salt particles is becoming more important. This will be discussed in short later.

Figure 9.22 shows the changes in L_s (left side) and L_l (right side) at TOA. Again the overall pattern looks similar to the surface. But the amount of the change is lower at TOA compared to surface in both cases. L_s is reduced by about -11.2 $\mathrm{W\,m^{-2}}$, while L_l is increased by $1.5\,\mathrm{W\,m^{-2}}$. Due to the technical design of seeding low stratocumulus clouds and the strong inversion layer the sea salt is kept in the lower part of the troposphere. This indicates that the additional sea salt particles are reflecting on the one side radiation in the lower part of the atmosphere. But on the other side the released sea salt can form a wet internally mixed composition of sea salt aerosol, which changes the character of its impact on radiation. Absorption in the solar range is negligible

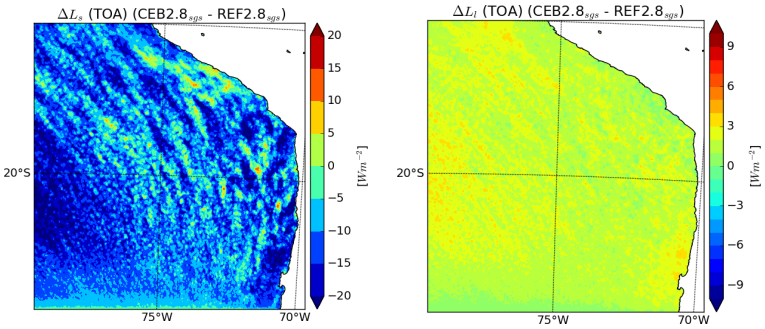

Figure 9.22: Impact on short-wave radiation (left) and long-wave radiation (right) for $CEB2.8$ - $REF2.8$ at top of the atmosphere (TOA). Only grid points over water are taken into account.

in case of sea salt. But with increasing wavelength absorption becomes more important. In the thermal spectrum absorption increases, as absorption of sulphate and water of the internal mixture becomes more important (Lundgren, 2010). This leads to an increase in long-wave downward radiation.

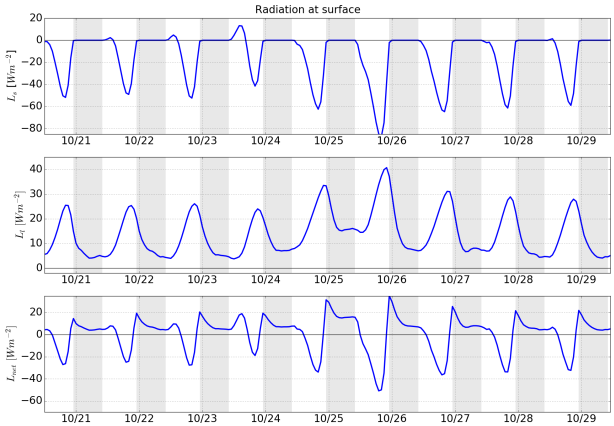

Figure 9.23: $REF2.8_{sgs}$ - $CEB2.8_{sgs}$Timeseries of short-wave (top), long-wave(middle), and net (bottom) radiation at surface. Only grid points over ocean are taken into account.

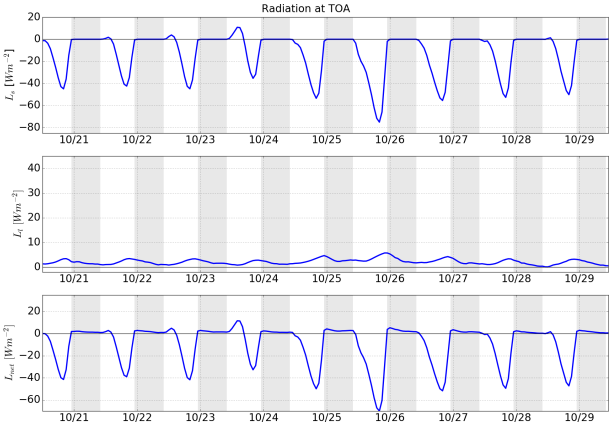

Figure 9.24: $REF2.8_{sgs}$ - $CEB2.8_{sgs}$Timeseries of short-wave (top), long-wave(middle), and net (bottom) radiation at top of the atmosphere (TOA). Only grid points over ocean are taken into account.

The timeseries in figure 9.23 reveals that although L_s shows a large reduction it is nearly compensated by L_l at the same time. During night time there is obviously no reduction in L_s. On the other side long-wave radiation L_l is increased also during night time. This leads to a positive L_{net} at the surface during night time. The timeseries at TOA (figure 9.24) shows also that at the top of the atmosphere L_s is decreased and L_l is increased but not to the same amount as at surface.

L_s at the surface is decreased by -13.3 Wm^{-2}, which is nearly compensated by an increase of L_l of about 10.8 Wm^{-2}. This arises the question which is the main driver causing the increase in L_l.

To prove the influence of the direct effect of the added sea salt particles a short simulation of three days[1] without the direct radiative effect of sea salt particles is evaluated. The simulation starts at the same time as $REF2.8_{sgs}$ and $CEB2.8_{sgs}$. For evaluation the first day is discarded and only the last two days will be shortly discussed. The timeseries of L_l, L_s and L_{net} at the surface for this short simulation is shown on the left side of figure 9.25. The impact on radiation is different to the impact in case of $CEB2.8_{sgs}$

[1] Only three days due to computational demand

(same period is shown on the right side). There is nearly none effect on L_l compared to $CEB2.8_{sgs}$. This indicates that the large impact on long-wave radiation is caused by the added sea salt particles itself, which are radiating back to surface.

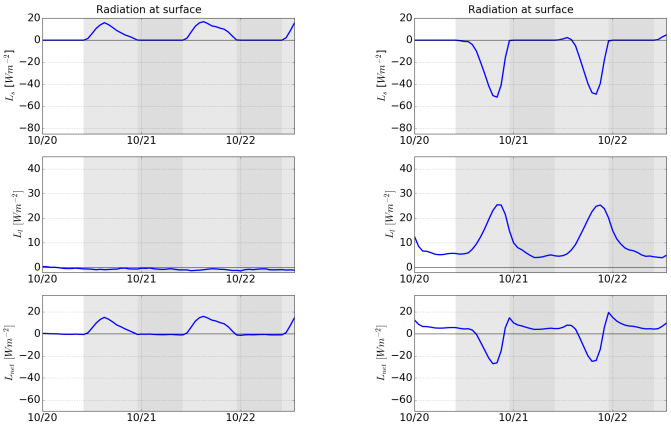

Figure 9.25: $REF2.8_{sgs}$ - $CEB2.8_{sgs}$ Timeseries of short-wave (top), long-wave(middle), and net (bottom) radiation at surface. On the right side radiative impact of sea salt is not taken into account. Only grid points over ocean are taken into account.

Furthermore without taking the direct effect of sea salt particles into account there is only a small impact on L_s and with the opposite sign. This fits well to the findings from the previous chapter where an increase in r_{eff} and a decrease of N_c is found due to the seeding with larger particles. If only radiative effects caused by changes in cloud properties are taken into account this leads to an increase in L_s at the surface (similar at TOA but not shown here). If the direct radiative effect of sea salt particles is neglected there is an increase of short-wave radiation at the surface, which is for this short period about $+4.0\,\mathrm{W\,m^{-2}}$ ($+3.35\,\mathrm{W\,m^{-2}}$ at TOA). On the other side there is a slight decrease in L_l which is for this short period about $-0.6\,\mathrm{W\,m^{-2}}$ ($-1.71\,\mathrm{W\,m^{-2}}$ at TOA). As already mentioned in the previous chapter seeding with larger sea salt particles is leading to a decrease in N_c and an increase in r_{eff}. This leads to an increase in short-wave radiation at the surface by altering cloud optical properties. But this would be

the case if only radiative feedbacks of clouds would be taken into account and direct radiative effects of aerosols, in this case sea salt particles, would be neglected.

Since COSMO-ART is taking the effect of growing sea salt particles with increasing ambient relative humidity into account the released sea salt particles can grow in size. Sea salt particles grow if ambient relative humidity is increasing and shrink if relative humidity is decreasing. As seen in the former chapter relative humidity is quite high in this region and therefore the additionally added sea salt particles are swelling over time. Additionally sulphuric acid is able to condense on the sea salt particles and form an internally mixture. The seeding rate exceeds, especially in case of sea salt mode sb, by far the production rate of sea salt by natural processes. This is of course mainly happening in areas with low wind speeds since natural emission rates are a function of 10 m wind speed. Once emitted the added particles are swelling over time and a dense haze consisting of sea salt particles is forming, with further impacts on radiation.

This leads to the conclusion that in case of $CEB2.8_{sgs}$ the seeded larger sea salt particles are responsible for the large decrease in L_s due to reflection of incoming solar radiation. Changes in cloud optical properties lead only to a small increase of L_s. Absorption of long-wave radiation in the boundary layer is causing an increase in long-wave downward radiation at the surface which nearly compensates the reduction of short-wave radiation. In $CEB2.8_{sgs}$ the main impacts on radiation does not originate by changes in cloud optical properties, but by changes in aerosol composition.

Because the parametrization of the seeding flux is based on the number concentration it also means that seeding with larger particles and the same number flux leads to an increase in mass flux in the scenario $CEB2.8_{sgs}$ compared to the mass flux in $CEA2.8_{sgs}$. The experimental design of $CEB2.8_{sgs}$ may be unrealistic, due to the large emitted mass of sea salt particles. But it underlines on one side that the right size of the seeding particles is essential to influence the cloud optical properties in a way that the intended effect of MCB is achieved. But on the other side it reveals that only producing a high number of seeding particles could also be problematic, since the mass of the sea salt aerosol increases with the seeding flux. Especially in case of seeding with larger particles. Seeding with larger particles leads to unwanted effects that first

cloud optical properties are not changed as intended and second the direct effect on radiation due to the seeded particles is increased. In case of $CEB2.8_{sgs}$ leading to a positive forcing in long-wave radiation due to absorption in the atmosphere.

But the result of $CEB2.8sgs$ has also implications towards seeding with smaller particles like the particles released in the size range of sea salt mode sa. Due to their small size the increase of their mass may be still relatively small in case of seeding. But if the mass of the small particles is also increased massively this has further impacts on radiation. If there is the intention to further increase the number concentration of small particles this would also lead to a further increase in mass. The smaller sea salt particles can also form an internally mixture and therefore also absorb long-wave radiation. The absorption of the smaller sea salt mode sa is even larger than the absorption of the internal mixture of sea salt mode sb. In the presence of water and sulphate two strong absorbing components are available for the internal mixture. Since water is in principle available everywhere in the SEP and sulphate dominates at the coast due to anthropogenic processes but also in the remote area through DMS an internal mixture of sea salt can be potentially formed everywhere. Following that it could also have major impacts on radiation in case of seeding with small particles by decreasing efficiency due to the direct radiative effects of the sea salt particles.

Seeding with small and larger particles

The last discussed seeding scenario ($CEAB7_{sgs}$) considers seeding with small and larger particles with the same total number flux as it was used in the previous scenarios. The only difference is that the flux is weighted 50 % for each size, so that 50 % are released to sea salt mode sa and 50 % to sea salt mode sb. The idea behind that scenario is that a certain amount of seeding particles are intended to be produced but only a part is produced into the small size range due to technical issues or coagulation within the nozzle. For this scenario only the domain of 7 km was used as a larger domain is covered.

The timeseries of $CEAB7_{sgs}$ shows a reduction in surface L_s but also a slight increase in L_l (figure 9.26). Although L_{net} shows an overall reduction in radiative forcing, during night time the

net incoming radiation is positive. From the previous findings it follows that the larger particles are leading to a compensation of the effect on short-wave radiation due to an increase in long-wave radiation at the surface. Seeding with smaller and larger particles still leads to an overall reduction in radiation, but the efficiency is reduced, as the impact on short-wave radiation is not that large as in $CEA7_{sgs}$ and the impact on long-wave radiation is larger than in $CEA7_{sgs}$. The timeseries at TOA (figure 9.27) shows similar effects on L_s, but the overall reduction is smaller than at the surface. On the other side the changes in L_l is nearly zero at TOA.

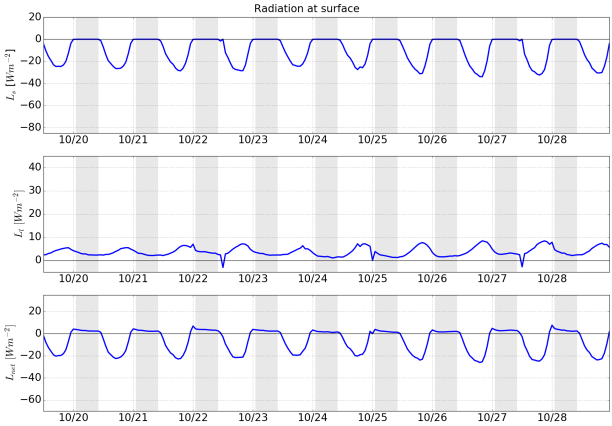

Figure 9.26: $REF7_{sgs}$ - $CEAB7_{sgs}$Timeseries of short-wave (top), long-wave(middle), and net (bottom) radiation at surface. Only grid points over ocean are taken into account.

The horizontal mean of L_s (left) and L_L (right) of $CEAB7_{sgs} - REF7_{sgs}$ is shown in figure 9.28. Again the seeding shows no uniform reduction. Areas with high reduction in L_s together with an increase in L_s is occuring. The reduction of L_s dominates over the remote area over the ocean, while the increase of L_s is mostly near the coast. $CEA7_{sgs}$ shows a similar pattern but the pattern is more pronounced in case of $CEAB7_{sgs}$. Furthermore the highest reduction in L_s is accompanied with the highest increase in L_l. There the intended effect of MCB is partially compensated. The

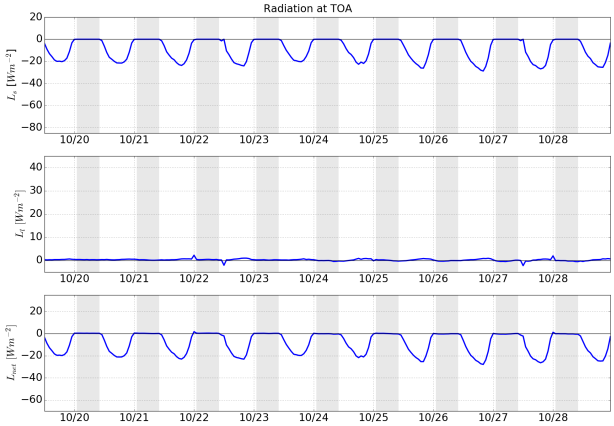

Figure 9.27: $REF7_{sgs}$ - $CEAB7_{sgs}$ Timeseries of short-wave (top), long-wave(middle), and net (bottom) radiation at top of the atmosphere (TOA). Only grid points over ocean are taken into account.

total reduction in L_s is about -10.8 W m^{-2}, while L_l is increased by +3.7 W m^{-2}.

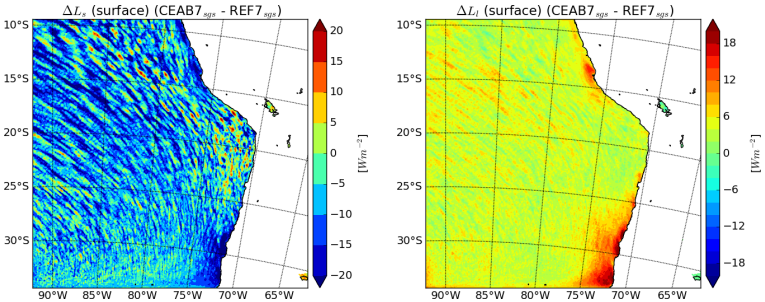

Figure 9.28: Impact on short-wave radiation (left) and long-wave radiation (right) for $CEAB7$ - $REF7$ at top of the atmosphere (TOA). Only grid points over water are taken into account.

The changes in L_s and L_l at TOA is shown in figure 9.29 and they are smaller than at the surface. L_s is decreased by -8.4 W m^{-2} and L_l is increased by 0.2 W m^{-2} at TOA.

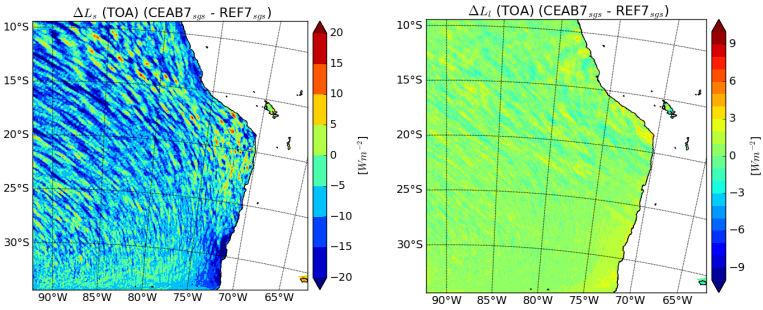

Figure 9.29: Impact on short-wave radiation (left) and long-wave radiation (right) for $CEAB7$ - $REF7$ at top of the atmosphere (TOA). Only grid points over water are taken into account.

From the results it follows that the efficiency of MCB is a function of the size of the emitted particles and a function of preexisting aerosol particles. Smaller particles are more efficient in changing cloud optical properties to reduce solar radiation. It is shown that small sea salt particles which are seeded in the size range of 0.02 to 1.0 μm lead to a reduction in incoming short-wave radiation. The size range of the seeding particles used in the scenario $CEA2.8_{sgs}$ and $CEA7_{sgs}$ is smaller than the size particles (monodispersed size of 1μm) proposed by Latham et al. (2008). On the other hand seeding with larger particles in the size range of 1.0 to 9 μm leads to a result which is not intended by MCB. Seeding with particles in this size range reduces cloud droplet number concentration and lead to a reversed Twomey effect. But this is only the half truth since this is the case if only the impact of clouds on radiation is taken into account. The seeding scenario $CEB2.8_{sgs}$ reveals that if the direct radiative effect of the sea salt particles is taken into account it has further impacts on radiation. With increasing mass of the seeded particles the direct radiative effect of the seeding particles is getting more and more important. Although N_c is not increasing the direct effect of the aerosol particles reduced short-wave radiation. But on the other side the seeded aerosols increase downward terrestrial radiation. Which at the end reduces the efficiency of MCB.

A combination of both size ranges results in a reduction of incoming short-wave radiation, but it is less efficient than seeding with the smallest particles. The direct effect on radiation caused by the larger particles (enhanced downward long-wave radiation) is partially compensating the efficiency of the smaller particles. This underlines again the importance to investigate also the direct radiation feedbacks of the seeding particles and not the impacts on cloud optical properties alone. As already mentioned the efficiency of MCB is also a function of preexisting aerosol. If aerosols are available in a large concentration MCB is ineffective. This includes not only anthropogenic aerosol like sulphate particles, it includes also natural aerosol particles like sea salt particles by natural processes. This arises to question the wind dependent function of seeding emissions proposed by Latham et al. (2008). Because this implies that CE emissions are highest were wind speeds are also very high. But in areas with high wind velocities natural sea salt production is higher compared to calmer areas and therefore lowering MCB efficiency. It would be more efficient to deploy a constant flux of additional sea salt particles in regions with low wind speeds and a low amount of aerosol particles, either from anthropogenic or natural sources.

Table 9.1 gives an overview of the radiative forcing due to the different scenarios. Although the domains differ in size and grid resolution (7 km and 2.8 km) and are therefore not one to one comparable, they can be used to classify the efficiency of the different seeding scenarios. Table 9.1 shows the changes in L_s and L_l at the surface (SURF) and the top of the atmosphere (TOA). The given values at the surface are the net downward short- and long-wave radiation and at TOA the net downward short-wave radiation and the outgoing long-wave radiation.

$CEA2.8_{sgs}$ and $CEB2.8_{sgs}$ shows that although the change in L_s is higher in $CEB2.8_{sgs}$ than in $CEA2.8_{sgs}$ (SURF and TOA), the change in L_l in $CEB2.8_{sgs}$ is also higher than in $CEA2.8_{sgs}$. The decrease in L_s in $CEA2.8_{sgs}$ is mainly due to the change in cloud optical properties. L_l is increased by $1.9\,\mathrm{W\,m^{-2}}$ at the surface and slightly decreased at TOA. However, the decrease in L_s in case of $CEB2.8_{sgs}$ is -13.3 $\mathrm{W\,m^{-2}}$ at the surface and therefore $2.1\,\mathrm{W\,m^{-2}}$ higher than in $CEA2.8_{sgs}$. But this is not due to the change of cloud optical properties as shown in chapter 9.1. In fact it is caused by the seeded particles itself. Since the same

Table 9.1: Overview of the impact on radiation at the surface (SURF) and the top of the atmosphere (TOA) due to different sized seeding particles. Note that the domains and therefore the impact on radiation cannot be compared one to one due to the different domain sizes and grid resolution.

Simulation	Seeded mode		L_s	L_l
$CEA7_{nosgs}$	A	SURF	-7.4	+0.1
		TOA	-6.1	+0.06
$CEA7_{sgs}$	A	SURF	-9.0	+0.4
		TOA	-7.5	-0.2
$CEAB7_{sgs}$	A & B	SURF	-10.8	+3.7
		TOA	-8.4	+0.2
$CEA2.8_{nosgs}$	A	SURF	-9.9	+1.6
		TOA	-8.7	-0.2
$CEA2.8_{sgs}$	A	SURF	-11.3	+1.9
		TOA	-9.9	-0.3
$CEB2.8_{sgs}$	B	SURF	-13.3	+10.8
		TOA	-11.2	+1.5

number flux was used for every seeding scenario the mass flux of the seeded sea salt particles is higher in $CEB2.8_{sgs}$ than in $CEA2.8_{sgs}$. The additionally added larger particles are on the one side reflecting incoming solar radiation which decreases incoming radiation at the surface and TOA. The change in L_s is larger at the surface and TOA in $CEB2.8_{sgs}$ than in $CEA2.8_{sgs}$. As the seeding particles are forming an internal mixture with water and sulphate the outgoing thermal radiation is absorbed by the internal mixture and in reverse downward long-wave radiation is increased. Therefore L_l is increased by $10.8\,\mathrm{W\,m^{-2}}$ at the surface in case of $CEB2.8_{sgs}$ compared to only $1.9\,\mathrm{W\,m^{-2}}$ in case of $CEA2.8_{sgs}$. The change in L_l at TOA in case of $CEB2.8_{sgs}$ is about $+1.5\,\mathrm{W\,m^{-2}}$ compared to a slight decrease in $CEA2.8_{sgs}$ ($-0.3\,\mathrm{W\,m^{-2}}$). This means that in case of $CEB2.8_{sgs}$ the seeding sea salt particles are absorbing long-wave radiation and this is leading to a further heating within the atmosphere.

L_s in scenario $CEA7_{sgs}$ is reduced by $-9.0\,\mathrm{W\,m^{-2}}$ at the surface and $-7.5\,\mathrm{W\,m^{-2}}$ at TOA. In $CEAB7_{sgs}$ L_s is reduced by $-10.8\,\mathrm{W\,m^{-2}}$ at the surface and $-8.4\,\mathrm{W\,m^{-2}}$ at TOA. In $CEAB7_{sgs}$ the change in L_s is higher compared to $CEA7_{sgs}$. Not only the reduction in L_s is higher in $CEAB7_{sgs}$, but also the increase in L_l at the surface is higher in $CEAB7_{sgs}$ than in $CEA7_{sgs}$. L_l is increased at the surface by $+3.7\,\mathrm{W\,m^{-2}}$ and only slightly increased by $+0.2\,\mathrm{W\,m^{-2}}$ at TOA. Following the results of $CEB2.8_{sgs}$ the larger particles released in $CEAB7_{sgs}$ leading to absorption of long-wave radiation and therefore downward long-wave radiation is increased. Again the difference between surface and TOA of L_s and L_l is larger in $CEAB7_{sgs}$ compared to $CEA7_{sgs}$. This indicates that due to absorption more energy is added to the atmosphere in case of $CEAB7_{sgs}$ and therefore reducing efficiency of MCB.

The numbers in table table 9.1 show that it is necessary to include aerosol cloud interaction for subgrid scale clouds. The changes in L_s of $CEA7_{nosgs}$ and $CEA7_{sgs}$ differ by $1.6\,\mathrm{W\,m^{-2}}$ at the surface and $1.4\,\mathrm{W\,m^{-2}}$ at TOA. Also the changes in L_l differ, but only slightly. Fixed values for subgrid scale clouds can disguise the effect of aerosol cloud interaction. If a model distinguish between grid scale and subgrid scale clouds and subgrid scale clouds are not affected by changes in aerosol concentration and aerosol composition, it is leading to an underestimation of

the aerosol indirect effect. In case of $CEA7_{sgs}$ and $CEA7_{nosgs}$ the effect is underestimated by 20 %. The underestimation in $CEA2.8_{sgs}$ and $CEA2.8_{nosgs}$ is about 13 % and therefore smaller compared to the simulations with coarser resolution. This is also seen in chapter 8.2 as the improvement compared to observations is larger in case of the coarser resolution than in case of the higher resolution. This is due the fact that clouds are already better resolved in case of the higher resolution. It proves that neglecting aerosol processes in subgrid scale parametrization can lead to an underestimation of the impacts caused by aerosol cloud interaction processes.

10 Conclusion and Summary

Within this work the regional impact of marine cloud brightening (MCB) in the South East Pacific (SEP) due to seeding with additional sea salt particles is analysed with the regional model system COSMO-ART (Vogel et al., 2009). The framework is able to simulate gas-phase processes, aerosol dynamics and cloud processes with a comparable level of complexity. Aerosol cloud interaction of subgrid scale clouds, which are not resolved by grid size and have to be parametrized, are neglected prior to this work. For this purpose the model system is extended to take aerosol cloud interaction in case of subgrid scale clouds into account. This is necessary since in COSMO-ART grid scale and subgrid scale clouds are treated separate. Prior to this work only grid scale clouds and therefore grid scale optical properties of clouds were affected by changes in aerosol properties. Because of that subgrid scale clouds were not linked to changes in aerosol properties and therefore subgrid scale cloud optical properties remained unchanged. This disadvantage is eliminated by introducing subgrid scale cloud droplet number concentration which are calculated by grid scale aerosol concentration and composition. The subgrid scale cloud droplet number concentration is then used together with a diagnosed subgrid scale cloud liquid water content to calculate subgrid scale cloud optical properties. Furthermore two different domains with different grid sizes are chosen to investigate at which grid size the subgrid scale cloud optical properties are still necessary.

With MCB it is intended to counteract global warming caused by anthropogenic activities. For this purpose it is intended to change incoming solar radiation by changing optical properties of marine low-level stratocumulus clouds. To increase cloud optical depth and therefore the reflectivity of the clouds cloud droplet number concentration has to be increased. One possible way is to release sea salt particles into the lower troposphere by ships to increase the amount of cloud condensation nuclei and therefore cloud droplet number concentration. To reduce uncertainties before

real deployment, numerical simulations are carried out to analyse the effects of MCB. Since mainly global climate models (GCM) are used to investigate the effects of MCB and because GCMs have certain uncertainties with the treatment of low-level clouds COSMO-ART is filling the gap between GCMs and large eddy simulations.

The results of the work are divided in two major parts. In the first part COSMO-ART is evaluated against observations. The simulation take place from 19th October to 10th of November 2008. During the same time period the field campaing VOCALS-REx was conducted and the results of it are used in this work to evaluate COSMO-ART.

In the second part the effects of MCB are evaluated. As aerosols act as cloud condensation nuclei and the activation of an aerosol particle to a cloud droplet depends on the size of the aerosol particle, the impact of additional sea salt particles is quantified with different seeding scenarios. Therefore the size of the seeding particles differ in the applied scenarios. Furthermore the role of the direct effect of the seeded sea salt particles is investigated. Additionally the impact on radiation is investigated in case of neglecting subgrid scale aerosol cloud radiation interaction and taking it into account.

Furthermore it is found that the shallow convection parametrization (Tiedtke scheme) used in COSMO-ART has major deficits in the area of SEP. Neglecting aerosol cloud interaction is one of it. But more drastically it shows that the shallow convection parametrization interferes with grid scale properties in a way that in case of the highest resolved simulation the parametrization suppresses grid scale cloud evolution. Which is not the duty of a subgrid scale parametrization. Therefore the convection parametrization is not used for any of the simulations.

Cloud properties (cloud droplet number concentration, effective radius, LWP) of the baseline simulation compare well to observations of VOCALS-REx. Only the height of the boundary layer is slightly underestimated by the model, because vertical mixing is not sufficient enough. Comparison of cloud properties like cloud droplet number concentration and effective radius r_{eff} are very promising. The general distribution of cloud droplet number concentration in the South East Pacific, where highest amount of cloud droplet number concentration is located near the coast

and is decreasing towards open sea, is reproduced by the model. This is due to a high amount of anthropogenic aerosol near the coast which is dominating the cloud droplet number concentration. Therefore r_{eff} is lowest near the coast and increases offshore, which is reproduced by COSMO-ART.

The impact of subgrid scale aerosol cloud interaction on surface radiation is compared to observations. It is found that taking subgrid scale aerosol cloud interaction into account leads to an improvement of the model results compared to observations, since the root mean square error (RMSE) decreases and the coefficient of determination ($R2$) increases. The improvement is higher in case of the coarse resolution as RMSE improves from 245.2 to 211.5 $\mathrm{W\,m^{-2}}$ and $R2$ from 0.765 to 0.82. RMSE in case of the higher resolved domain improves from 220.4 to 212.6 $\mathrm{W\,m^{-2}}$ and $R2$ from 0.806 to 0.814. The improvement in case of the coarser resolution is more pronounced which is not surprising since less clouds are resolved on the grid scale in the coarser resolution. Furthermore by taking the subgrid scale aerosol cloud interaction into account the RMSE and $R2$ are in the same order for both grid sizes.

For both grid sizes the climate engineering simulations with smaller seeding particles show an increase of cloud droplet number concentration over the domain, while the effective cloud droplet radius decreases, which is expected and is intended by marine cloud brightening. On the other hand the cloud liquid water content (LWC) increases slightly, other then assumed by the theory of Twomey (1977) on which the idea of marine cloud brightening is based. There the assumption of a constant LWC is made. As the cloud optical depth is not only a function of cloud droplet number concentration, respectively the cloud effective radius, but also of liquid water content the results show that this is only a simple assumption and should be revised.

To identify areas which are more suitable for seeding than others the quantity β_{N_c} is introduced, which is the susceptibility of the cloud droplet number concentration to the seeded particles. With β_{N_c} regions which are more susceptible to seeding are identified. Those regions are affected by pristine condition, like they are found over the open sea. Regions which are less susceptible to seeding are found near the coast. Those regions are affected by a more polluted environment due to anthropogenic activities. Especially

the plume originating from anthropogenic emissions along the coast shows that there is in principle no effectiveness due to seeding. This results from the competition between the seeded and the anthropogenic particles. An already high polluted environment is not suitable for seeding, since cloud droplet number concentration is already high and a change in number concentration does not change optical depth any further. Furthermore the seeding particles decreasing supersaturation and therefore seeding inhibits activation of smaller anthropogenic particles. In the worst case even reducing cloud droplet number concentration.

This is the result of a scenario with larger seeding particles. To quantify the impact of the size of the seeding particles scenarios with different sized particles are conducted. The scenarios show that smaller particles are more effective to change cloud optical properties as it is intended by MCB. Larger particles show a negative effect on cloud properties as cloud droplet number concentration is decreasing and cloud effective radius is increasing. Seeding with smaller particles show the intended effect of MCB as cloud droplet number concentration is increasing and cloud effective radius is decreasing.

The impact on short-wave radiation is quite large in case of seeding with smaller particles as the short-wave radiation is changed by -11.3 $\mathrm{W\,m^{-2}}$ at the surface and -9.9 $\mathrm{W\,m^{-2}}$ at top of the atmosphere in case of the higher resolved domain. Seeding with larger particles has also a large impact on short-wave radiation. The reduction in short-wave radiation in case of the small domain shows a change of -13.3 $\mathrm{W\,m^{-2}}$ at the surface and -11.2 $\mathrm{W\,m^{-2}}$ at top of the atmosphere. The impact on the short-wave radiation is even larger than in case of seeding with small particles. This change in short-wave radiation is mainly due to the direct radiative effect of the seeded particles. A short simulation without direct radiation interaction due to sea salt particles proves this. The fact that the same flux parametrization for number concentration of the seeding particles is used in case of the larger particles results in an increase of sea salt mass, which causes a high impact on short-wave radiation. But the reduction of short-wave radiation at the surface is nearly compensated by a positive effect on long-wave radiation of about +10.8 $\mathrm{W\,m^{-2}}$. Seeding with smaller particles shows a smaller effect on long-wave radiation at the surface of only +1.6 $\mathrm{W\,m^{-2}}$. This shows that in case of MCB the direct effect

of the seeded particle can not be neglected, because it partially compensates the efficiency of MCB.

In case of the larger domain but with coarser resolution and seeding with smaller particles short-wave radiation was changed by -9.0 $\mathrm{W\,m^{-2}}$ at the surface and -7.5 $\mathrm{W\,m^{-2}}$ at top of the atmosphere. Long-wave radiation on the other hand changes only barely. In case of the larger domain a third scenario is conducted, where smaller and larger particles are seeded, but the flux parametrization is weighted 50 % to each sea salt mode. The short-wave radiation is reduced by -10.8 $\mathrm{W\,m^{-2}}$ at the surface and -8.4 $\mathrm{W\,m^{-2}}$ at top of the atmosphere. Long-wave radiation is increased by 3.7 $\mathrm{W\,m^{-2}}$ at surface and only by 0.2 $\mathrm{W\,m^{-2}}$ at top of the atmosphere. This is caused by the direct effect of the seeding particles, as the sea salt particles grow with relative humidity and form an internal mixture (with water and sulfate). This leads to an increase in downward long-wave radiation. As the forcing at top of the atmosphere is lower than at the surface a portion of the radiation is added to atmospheric forcing. At the end this is lowering efficiency of MCB. This concludes that the mass of the seeded particles becomes important at a certain point.

It is found that aerosol cloud interaction of subgrid scale processes cannot be neglected. This is underlined by the comparison of the simulations where subgrid scale aerosol cloud radiation interaction is neglected and taken into account. As the magnitude of the impact of MCB is different in both scenarios this underlines the importance of subgrid scale aerosol cloud radiation interaction. In case of the larger domain (7 km grid sizing) seeding with smaller particles shows a reduction of -7.4 $\mathrm{W\,m^{-2}}$ at the surface (-6.1 $\mathrm{W\,m^{-2}}$ at top of the atmosphere) in case of neglecting subgrid scale aerosol cloud interaction. If the subgrid scale aerosol cloud interaction is taken into account the change of short-wave radiation is about -9.0 $\mathrm{W\,m^{-2}}$ and therefore about 20 % larger. In both cases long-wave radiation is only changed marginally. This shows the importance of including aerosol cloud interaction for subgrid scale processes.

This work shows that MCB leads to more non-linear effects then expected by the simple assumptions of Twomey (1977) and Latham et al. (2008). Additional it is found that the suggested mean change of cloud droplet number concentration to a value of 375 $\mathrm{cm^{-3}}$ as stated by Latham et al. (2008) is never achieved in the

simulations. Setting the larger domain as a reference which could be seeded in a real world deployment it is possible to reduce the short-wave radiation at top of the atmosphere by -7.5 $\mathrm{W\,m^{-2}}$. But this is only a local change valid for the region of SEP. Assuming that all four suitable regions could be seeded the same way and it would be possible to achieve the same reduction in short-wave radiation globally it would be a reduction of -1.875 $\mathrm{W\,m^{-2}}$. This means less then -3.7 $\mathrm{W\,m^{-2}}$ Latham et al. (2008) which has to be achieved to compensate CO_2 doubling. Furthermore this takes only the changes in short-wave radiation into account. As it is shown in this work long-wave radiation due to direct effect of the seeded sea salt particles is partially compensating the efficiency of MCB.

To achieve the negative forcing in the simulation additional sea salt particles are released at every grid point over the ocean. Other then suggested by Korhonen et al. (2010) the flux in this work is constant over time and not depending on wind speed. The larger domain has 180600 grid points in total, while 56073 grid points are over land and 124527 grid points are over water. This would be the amount of ships needed in the scenarios of this work. Assuming that roughly only half of the grid points are not suitable for seeding due to competitive effects with anthropogenic aerosol and assuming that neglecting those points would not change the outcome of this work very much, there are still 62263 grid points (ships) left. Which underlines that MCB seems to be not very effective in reducing radiation in that way that it could compensate a doubling in CO_2.

11 Bibliography

Aitken, J., 1881: Xii.—on dust, fogs, and clouds. *Transactions of the Royal Society of Edinburgh*, **30 (01)**, 337–368.

Alapaty, K., J. A. Herwehe, T. L. Otte, C. G. Nolte, O. R. Bullock, M. S. Mallard, J. S. Kain, and J. Dudhia, 2012: Introducing subgrid-scale cloud feedbacks to radiation for regional meteorological and climate modeling. *Geophysical Research Letters*, **39 (24)**.

Albrecht, B. A., 1989: Aerosols, cloud microphysics, and fractional cloudiness. *Science*, **245 (4923)**, 1227–1230.

Alterskjær, K. and J. Kristjánsson, 2013: The sign of the radiative forcing from marine cloud brightening depends on both particle size and injection amount. *Geophysical Research Letters*, **40 (1)**, 210–215.

Alterskjær, K., J. Kristjánsson, and Ø. Seland, 2012: Sensitivity to deliberate sea salt seeding of marine clouds-observations and model simulations. *Atmospheric Chemistry and Physics*, **12 (5)**, 2795.

Andersen, H., J. Cermak, J. Fuchs, and K. Schwarz, 2016: Global observations of cloud-sensitive aerosol loadings in low-level marine clouds. *Journal of Geophysical Research: Atmospheres*, **121 (21)**.

Arakawa, A., 2004: The cumulus parameterization problem: Past, present, and future. *Journal of Climate*, **17 (13)**, 2493–2525.

Arking, A., 1991: The Radiative Effects of Clouds and their Impact on Climate. *B. A.M. Meteorol. Soc.*, **72**, 795–953.

Aswathy, V., O. Boucher, M. Quaas, U. Niemeier, H. Muri, and J. Quaas, 2014: Climate extremes in multi-model simulations of stratospheric aerosol and marine cloud brightening climate

engineering. *Atmospheric Chemistry and Physics Discussions*, **14 (23)**, 32 393–32 425.

Baldauf, M., A. Seifert, J. Förstner, D. Majewski, M. Raschendorfer, and T. Reinhardt, 2011: Operational convective-scale numerical weather prediction with the cosmo model: description and sensitivities. *Monthly Weather Review*, **139 (12)**, 3887–3905.

Bangert, M., 2012: Interaction of aerosol, clouds, and radiation on the regional scale. Ph.D. thesis, Karlsruhe, Karlsruher Institut für Technologie (KIT).

Bangert, M., C. Kottmeier, B. Vogel, and H. Vogel, 2011: Regional scale effects of the aerosol cloud interaction simulated with an online coupled comprehensive chemistry model. *Atmos. Chem. Phys.*, **11 (9)**, 4411–4423.

Bangert, M., A. Nenes, B. Vogel, H. Vogel, D. Barahona, V. A. Karydis, P. Kumar, C. Kottmeier, and U. Blahak, 2012: Saharan dust event impacts on cloud formation and radiation over western europe. *Atmos. Chem. Phys.*, **12 (9)**, 4045–4063.

Barahona, D., R. E. L. West, P. Stier, S. Romakkaniemi, H. Kokkola, and A. Nenes, 2010: Comprehensively accounting for the effect of giant ccn in cloud activation parameterizations. *Atmospheric Chemistry and Physics*, **10 (5)**, 2467–2473, URL `http://www.atmos-chem-phys.net/10/2467/2010/`.

Bergeron, T., 1935: *On the Physics of Cloud Precipitation*.

Boucher, O., 2015: Atmospheric aerosols. *Atmospheric Aerosols*, Springer, 9–24.

Boucher, O., D. Randall, P. Artaxo, C. Bretherton, G. Feingold, P. Forster, V.-M. Kerminen, Y. Kondo, H. Liao, U. Lohmann, et al., 2013: Clouds and aerosols. *Climate change 2013: the physical science basis. Contribution of Working Group I to the Fifth Assessment Report of the Intergovernmental Panel on Climate Change*, Cambridge University Press, 571–657.

Brasseur, G., D. Hauglustaine, S. Walters, R. Rasch, J. Müller, C. Granier, and X. Tie, 1998: Mozart, a global chemical transport model for ozone and related chemical tracers 1. model description. *J. Geophys. Res.*, **103 (D21)**, 28 265–28.

Charlson, R. J., S. Schwartz, et al., 1992: Climate forcing by anthropogenic aerosols. *Science*, **255 (5043)**, 423.

Coakley, J., R. Bernstein, and P. Durkee, 1987: Effect of ship-stack effluents on cloud reflectivity. *Science (New York, NY)*, **237 (4818)**, 1020.

Coakley Jr, J. A., P. A. Durkee, K. Nielsen, J. P. Taylor, S. Platnick, B. A. Albrecht, D. Babb, F.-L. Chang, W. Tahnk, C. S. Bretherton, et al., 2000: The appearance and disappearance of ship tracks on large spatial scales. *Journal of the atmospheric sciences*, **57 (16)**, 2765–2778.

Doms, G., J. Förstner, E. Heise, H.-J. Herzog, D. Mironov, M. Raschendorfer, T. Reinhardt, B. Ritter, R. Schrodin, J.-P. Schulz, and G. Vogel, 2011: A description of the nonhydrostatic regional cosmo model.

Feichter, J. and T. Leisner, 2009: Climate engineering: A critical review of approaches to modify the global energy balance. *Eur. Phys. J-Spec. Top.*, **176**, 81–92, URL `http://dx.doi.org/10.1140/epjst/e2009-01149-8`, 10.1140/epjst/e2009-01149-8.

Findeisen, W., 1938: Die kolloidmeteorologischen vorgänge bei der niederschlagsbildung. *Meteor. Z*, **55**, 121–133.

Fountoukis, C. and A. Nenes, 2005: Continued development of a cloud droplet formation parameterization for global climate models. *J. Geophys. Res.*, **110**.

Giorgetta, M. A., E. Roeckner, T. Mauritsen, J. Bader, T. Crueger, M. Esch, S. Rast, L. Kornblueh, H. Schmidt, S. Kinne, et al., 2013: The atmospheric general circulation model echam6-model description.

Hänel, G., 1976: The properties of atmospheric aerosol particles as functions of the relative humidity at thermodynamic equilibrium with the surrounding moist air. *Advances in geophysics*, **19**, 73–188.

Herzog, H. and D. Golomb, 2004: Carbon capture and storage from fossil fuel use. *Encyclopedia of energy*, **1**, 1–11.

Hill, S. and Y. Ming, 2012: Nonlinear climate response to regional brightening of tropical marine stratocumulus. *Geophysical Research Letters*, **39 (15)**.

Houze Jr, R. A., 2014: *Cloud dynamics*, Vol. 104. Academic press.

Hu, Y. and K. Stamnes, 1993: An accurate parameterization of the radiative properties of water clouds suitable for use in climate models. *Journal of climate*, **6 (4)**, 728–742.

Jacobson, M. Z., 2005: *Fundamentals of atmospheric modeling*. Cambridge university press.

Jones, A. and J. Haywood, 2012: Sea-spray geoengineering in the hadgem2-es earth-system model: radiative impact and climate response. *Atmospheric Chemistry and Physics*, **12 (22)**, 10 887–10 898.

Jones, A., J. Haywood, and O. Boucher, 2009: Climate impacts of geoengineering marine stratocumulus clouds. *J. Geophys. Res.*, **114**.

Jung, E., B. A. Albrecht, H. H. Jonsson, Y.-C. Chen, J. H. Seinfeld, A. Sorooshian, A. R. Metcalf, S. Song, M. Fang, and L. M. Russell, 2015: Precipitation effects of giant cloud condensation nuclei artificially introduced into stratocumulus clouds. *Atmospheric Chemistry and Physics*, **15 (10)**, 5645–5658.

Kerminen, V.-M. and A. S. Wexler, 1994: Post-fog nucleation of h2so4-h2o particles in smog. *Atmospheric Environment*, **28 (15)**, 2399–2406, URL `https://doi.org/10.1016/1352-2310(94)90391-3`.

Köhler, H., 1936a: The nucleus in and the growth of hygroscopic droplets. *Trans. Faraday Soc.*, **32**, 1152–1161.

———, 1936b: The nucleus in and the growth of hygroscopic droplets. *Transactions of the Faraday Society*, **32**, 1152–1161.

Korhonen, H., K. S. Carslaw, and S. Romakkaniemi, 2010: Enhancement of marine cloud albedo via controlled sea spray injections: a global model study of the influence of emission rates, microphysics and transport. *Atmos. Chem. Phys.*

Kraus, E. and P. Squires, 1947: Experiments on the stimulation of clouds to produce rain. *Nature*, **159 (4041)**, 489–491.

Lampitt, R., E. Achterberg, T. Anderson, J. Hughes, M. Iglesias-Rodriguez, B. Kelly-Gerreyn, M. Lucas, E. Popova, R. Sanders, J. Shepherd, et al., 2008: Ocean fertilization: a potential means of geoengineering? *Phil. Trans. R. Soc. A*, **366 (1882)**, 3919–3945.

Latham, J., 2002: Amelioration of global warming by controlled enhancement of the albedo and longevity of low-level maritime clouds. *Atmos. Sci. Lett.*, **3 (2-4)**, 52–58.

Latham, J., K. Bower, T. Choularton, H. Coe, P. Connolly, G. Cooper, T. Craft, J. Foster, A. Gadian, L. Galbraith, et al., 2012: Marine cloud brightening. *Philos. T. Roy. Soc. A.*, **370 (1974)**, 4217–4262.

Latham, J., P. Rasch, C.-C. Chen, L. Kettles, A. Gadian, A. Gettelman, H. Morrison, K. Bower, and T. Choularton, 2008: Global temperature stabilization via controlled albedo enhancement of low-level maritime clouds. *Phil. Trans. R. Soc. A*, **366**, 3969–3987.

Lewis, E. and S. Schwartz, 2006: Comment on "size distribution of sea-salt emissions as a function of relative humidity". *Atmos. Environ.*, **40**, 588–590.

Lu, M.-L. and J. H. Seinfeld, 2006: Effect of aerosol number concentration on cloud droplet dispersion: A large-eddy simulation study and implications for aerosol indirect forcing. *Journal of Geophysical Research: Atmospheres*, **111 (D2)**.

Lundgren, K., 2006: Numerical simulation of the spatial and temporal distribution of sea salt particles on the regional scale.

———, 2010: Direct radiative effects of sea salt on the regional scale. Ph.D. thesis, Institut für Meteorologie und Klimaforschung (IMK), Karlsruhe.

Maalick, Z., H. Korhonen, H. Kokkola, T. Kühn, and S. Romakkaniemi, 2014: Modelling artificial sea salt emission in large

eddy simulations. *Philosophical Transactions of the Royal Society of London A: Mathematical, Physical and Engineering Sciences*, **372 (2031)**, 20140 051.

Mårtensson, E. M., E. D. Nilsson, G. de Leeuw, L. H. Cohen, and H.-C. Hansson, 2003: Laboratory simulations and parameterization of the primary marine aerosol production. *J. Geophys. Res.-Atmos.*, **108**, 4297.

Marchetti, C., 1977: On geoengineering and the co2 problem. *Climatic change*, **1 (1)**, 59–68.

Minnis, P., S. Sun-Mack, D. F. Young, P. W. Heck, D. P. Garber, Y. Chen, D. A. Spangenberg, R. F. Arduini, Q. Z. Trepte, W. L. Smith, et al., 2011: Ceres edition-2 cloud property retrievals using trmm virs and terra and aqua modis data—part i: Algorithms. *IEEE Transactions on Geoscience and Remote Sensing*, **49 (11)**, 4374–4400.

Mitchell, D. L. and W. Finnegan, 2009: Modification of cirrus clouds to reduce global warming. *Environmental Research Letters*, **4 (4)**, 045 102.

Monahan, E., S. E., and D. K., 1986: *A model of marine aerosol generation via whitecaps and wave disruption*. D. Reidel Publishing Company.

Morales, R. and A. Nenes, 2010: Characteristic updrafts for computing distribution-averaged cloud droplet number and stratocumulus cloud properties. *Journal of Geophysical Research: Atmospheres*, **115 (D18)**, n/a–n/a, URL `http://dx.doi.org/10.1029/2009JD013233`.

Nenes, A., S. Ghan, H. ABDUL-RAZZAK, P. Y. Chuang, and J. H. Seinfeld, 2001: Kinetic limitations on cloud droplet formation and impact on cloud albedo. *Tellus B*, **53 (2)**, 133–149.

Nenes, A. and J. H. Seinfeld, 2003: Parameterization of cloud droplet formation in global climate models. *Journal of Geophysical Research: Atmospheres*, **108 (D14)**.

Partanen, A.-I., H. Kokkola, S. Romakkaniemi, V.-M. Kerminen, K. E. J. Lehtinen, T. Bergman, A. Arola, and H. Korhonen,

2012: Direct and indirect effects of sea spray geoengineering and the role of injected particle size. *J. Geophys. Res.*, **117**.

Pérez, C., S. Nickovic, J. Baldasano, M. Sicard, F. Rocadenbosch, and V. Cachorro, 2006: A long saharan dust event over the western mediterranean: Lidar, sun photometer observations, and regional dust modeling. *Journal of Geophysical Research: Atmospheres*, **111 (D15)**.

Petty, G., 2004: *A First Course in Atmospheric Radiation*. Sundog Publishing, Madison.

Platnick, S. and L. Oreopoulos, 2008: Radiative susceptibility of cloudy atmospheres to droplet number perturbations: 1. theoretical analysis and examples from modis. *Journal of Geophysical Research: Atmospheres*, **113 (D14)**.

Pruppacher, H. R. and J. D. Klett, 1997: *Microphysics of clouds and precipitation*. 2d ed., Atmospheric and oceanographic sciences library ; 18, Kluwer, Dordrecht [u.a.].

Ramanathan, V., R. Cess, E. Harrison, P. Minnis, B. Barkstrom, E. Ahmad, and D. Hartmann, 1989: Cloud-radiative forcing and climate: Results from the earth radiation budget experiment. *Science*, **243 (4887)**, 57–63.

Randall, D. and J. Coakley, 1984: Outlook for research on subtropical marine stratiform clouds. *B. A.M. Meteorol. Soc.*

Rasch, P. J., J. Latham, and C.-C. J. Chen, 2009: Geoengineering by cloud seeding: influence on sea ice and climate system. *Environmental Research Letters*, **4 (4)**, 045 112.

Rinke, R., 2008: Parametrisierung des auswaschens von aerosolpartikeln durch niederschlag. Ph.D. thesis, Universität Karlsruhe (TH).

Ritter, B. and J.-F. Geleyn, 1992: A comprehensive radiation scheme for numerical weather prediction models with potential applications in climate simulations. *Monthly Weather Review*, **120 (2)**, 303–325.

Rosenfeld, D., R. Wood, L. J. Donner, and S. C. Sherwood, 2013: Aerosol cloud-mediated radiative forcing: highly uncertain and

opposite effects from shallow and deep clouds. *Climate Science for Serving Society*, Springer, 105–149.

Russell, L. M., A. Sorooshian, J. H. Seinfeld, B. A. Albrecht, A. Nenes, L. Ahlm, Y.-C. Chen, M. Coggon, J. S. Craven, R. C. Flagan, et al., 2013: Eastern pacific emitted aerosol cloud experiment. *Bulletin of the American Meteorological Society*, **94 (5)**, 709–729.

Salter, S., G. Sortino, and J. Latham, 2008: Sea-going hardware for the cloud albedo method of reversing global warming. *Phil. Trans. R. Soc. A*, **366**, 3989–4006.

Schad, T., 2012: Numerische simulation des einflusses künstlicher seesalz-emissionen auf stratocumulusbewölkung im südostpazifik. Master's thesis, Universität Karlsruhe (TH)/Forschungszentrum Karlsruhe.

Schell, B., I. J. Ackermann, H. Hass, F. S. Binkowski, and A. Ebel, 2001: Modeling the formation of secondary organic aerosol within a comprehensive air quality model system. *Journal of Geophysical Research: Atmospheres*, **106 (D22)**, 28 275–28 293.

Schreier, M., A. Kokhanovsky, V. Eyring, L. Bugliaro, H. Mannstein, B. Mayer, H. Bovensmann, and J. Burrows, 2006: Impact of ship emissions on the microphysical, optical and radiative properties of marine stratus: a case study. *Atmospheric Chemistry and Physics*, **6 (12)**, 4925–4942.

Schuiling, R. and P. Krijgsman, 2006: Enhanced weathering: An effective and cheap tool to sequester co 2. *Climatic Change*, **74 (1)**, 349–354.

Schwartz, S. E. and A. Slingo, 1995: Enhanced shortwave cloud radiative forcing due to anthropogenic aerosols. *NASA STI/Recon Technical Report N*, **95**, 34 214.

Segal, Y. and A. Khain, 2006: Dependence of droplet concentration on aerosol conditions in different cloud types: Application to droplet concentration parameterization of aerosol conditions. *J. Geophys. Res.-Atmos.*, **111**.

Seifert, A. and K. D. Beheng, 2001: A double-moment parameterization for simulating autoconversion, accretion and selfcollection. *Atmos. Res.*, **59–60 (0)**, 265 – 281, <ce:title>13th International Conference on Clouds and Precipitation</ce:title>.

———, 2006: A two-moment cloud microphysics parameterization for mixed-phase clouds. part 1: Model description. *Meteorology and Atmospheric Physics*, **92 (1-2)**, 45–66, URL `http://dx.doi.org/10.1007/s00703-005-0112-4`.

Seifert, A., A. Khain, A. Pokrovsky, and K. D. Beheng, 2006: A comparison of spectral bin and two-moment bulk mixed-phase cloud microphysics. *Atmospheric research*, **80 (1)**, 46–66.

Seinfeld, J. H. and S. N. Pandis, 2006: *Atmospheric chemistry and physics : from air pollution to climate change*. 2d ed., Wiley, Hoboken, NJ, previous ed.: 1998.

Seinfeld, S. N., John H. ; Pandis, 2006: *Atmospheric chemistry and physics : from air pollution to climate change*. 2d ed., Wiley, Hoboken, NJ, 1078 pp., previous ed.: 1998.

Shepherd, J. G., 2009: *Geoengineering the climate: science, governance and uncertainty*. Royal Society.

Siebesma, A. and A. Holtslag, 1996: Model impacts of entrainment and detrainment rates in shallow cumulus convection. *Journal of the atmospheric sciences*, **53 (16)**, 2354–2364.

Siebesma, A. P., P. M. Soares, and J. Teixeira, 2007: A combined eddy-diffusivity mass-flux approach for the convective boundary layer. *Journal of the atmospheric sciences*, **64 (4)**, 1230–1248.

Smith, M. H., P. M. Park, and I. E. Consterdine, 1993: Marine aerosol concentrations and estimated fluxes over the sea. *Q. J. R. Meteorol. Soc.*, **119 (512)**, 809–824.

Squires, P., 1958: The microstructure and colloidal stability of warm clouds: Part ii-the causes of the variations in microstructure. *Tellus*, **10 (2)**, 262–271.

Stanelle, T., B. Vogel, H. Vogel, D. Bäumer, and C. Kottmeier, 2010: Feedback between dust particles and atmospheric processes over west africa during dust episodes in march 2006 and june

2007. *Atmospheric Chemistry and Physics*, **10 (22)**, 10 771–10 788.

Stevens, B. and G. Feingold, 2009: Untangling aerosol effects on clouds and precipitation in a buffered system. *Nature*, **461 (7264)**, 607–613.

Stockwell, W., P. Middleton, and J. Chang, 1990: The second generation regional acid deposition model chemical mechanism for regional air quality modelling. *J. Geophys.Res.*, **95**, 16 343–16 367.

Storelvmo, T. and N. Herger, 2014: Cirrus cloud susceptibility to the injection of ice nuclei in the upper troposphere. *Journal of Geophysical Research: Atmospheres*, **119 (5)**, 2375–2389.

Storelvmo, T., J. Kristjansson, H. Muri, M. Pfeffer, D. Barahona, and A. Nenes, 2013: Cirrus cloud seeding has potential to cool climate. *Geophysical Research Letters*, **40 (1)**, 178–182.

Sundqvist, H., E. Berge, and J. E. Kristjánsson, 1989: Condensation and cloud parameterization studies with a mesoscale numerical weather prediction model. *Monthly Weather Review*, **117 (8)**, 1641–1657.

Swap, R., M. Garstang, S. Greco, R. Talbot, and P. Kållberg, 1992: Saharan dust in the amazon basin. *Tellus B*, **44 (2)**, 133–149.

Tiedtke, M., 1989: A comprehensive mass flux scheme for cumulus parameterization in large-scale models. *Monthly Weather Review*, **117 (8)**, 1779–1800.

Twomey, S., 1959: The nuclei of natural cloud formation part ii: The supersaturation in natural clouds and the variation of cloud droplet concentration. *Geofisica pura e applicata*, **43 (1)**, 243–249.

———, 1977: The influence of pollution on the shortwave albedo of clouds. *J. Atmos. Sci.*, **34 (7)**, 1149–1152.

———, 1991: Aerosols, clouds and radiation. *Atmos. Environ. A-Gen.*, **25 (11)**, 2435–2442.

Twomey, S. and P. Squires, 1959: The influence of cloud nucleus population on the microstructure and stability of convective clouds. *Tellus*, **11 (4)**, 408–411.

UCAR/NCAR - Earth Observing Laboratory., 2011: NCAR/NSF C-130 Navigation, State Parameter, and Microphysics HRT (25 sps) Data. Version 1.0. UCAR/NCAR - Earth Observing Laboratory. `https://doi.org/10.5065/D69K48JK.`, accessed 10 November 2016.

Vogel, B., H. Vogel, D. Bäumer, M. Bangert, K. Lundgren, R. Rinke, and T. Stanelle, 2009: The comprehensive model system COSMO-ART–Radiative impact of aerosol on the state of the atmosphere on the regional scale. *Atmos. Chem. Phys*, **9**, 8661–8680.

Wang, Y., S. Xie, H. Xu, and B. Wang, 2004a: Regional model simulations of marine boundary layer clouds over the southeast pacific off south america. part i: Control experiment*. *Mon. Weather Rev.*, **132 (1)**, 274–296.

Wang, Y., H. Xu, and S.-P. Xie, 2004b: Regional model simulations of marine boundary layer clouds over the southeast pacific off south america. part ii: Sensitivity experiments*. *Monthly weather review*, **132 (11)**, 2650–2668.

Wegener, A., 1911: *Thermodynamik der atmosphäre*. JA Barth.

Whitby, E. R. and P. H. McMurry, 1997: Modal aerosol dynamics modeling. *Aerosol Science and Technology*, **27 (6)**, 673–688.

Whitby, K. T., 1978: The physical characteristics of sulfur aerosols. *Atmos. Environ.*, **12 (1–3)**, 135 – 159, URL `https://doi.org/10.1016/B978-0-08-022932-4.50018-5`.

Wood, R., C. Bretherton, C. Mechoso, R. Weller, B. Huebert, F. Straneo, B. Albrecht, H. Coe, G. Allen, G. Vaughan, et al., 2010: The vamos ocean-cloud-atmosphere-land study regional experiment (vocals-rex): goals, platforms, and field operations. *Atmos. Chem. Phys. Discuss*, **10**, 20 769–20 822.

Wood, R., C. Mechoso, C. Bretherton, R. Weller, B. Huebert, F. Straneo, B. A. Albrecht, H. Coe, G. Allen, G. Vaughan, et al.,

2011: The vamos ocean-cloud-atmosphere-land study regional experiment (vocals-rex): goals, platforms, and field operations. *Atmospheric Chemistry and Physics*, **11 (2)**, 627–654.

Wyant, M., C. S. Bretherton, R. Wood, G. Carmichael, A. Clarke, J. Fast, R. George, W. Gustafson Jr, C. Hannay, A. Lauer, et al., 2015: Global and regional modeling of clouds and aerosols in the marine boundary layer during vocals: the voca intercomparison. *Atmospheric Chemistry and Physics*, **15 (1)**, 153–172.

Yanai, M., S. Esbensen, and J.-H. Chu, 1973: Determination of bulk properties of tropical cloud clusters from large-scale heat and moisture budgets. *Journal of the Atmospheric Sciences*, **30 (4)**, 611–627.

Zhang, C., Y. Wang, and K. Hamilton, 2011: Improved representation of boundary layer clouds over the southeast pacific in arw-wrf using a modified tiedtke cumulus parameterization scheme*. *Monthly Weather Review*, **139 (11)**, 3489–3513.

Zubler, E. M., D. Folini, U. Lohmann, D. Lüthi, A. Muhlbauer, S. Pousse-Nottelmann, C. Schär, and M. Wild, 2011: Implementation and evaluation of aerosol and cloud microphysics in a regional climate model. *Journal of Geophysical Research: Atmospheres*, **116 (D2)**, URL `http://dx.doi.org/10.1029/2010JD014572`.

Acknowledgements

This work was performed during the years 2014 and 2017 at the Institute of Meteorology and Climate Research, Troposphere Research (IMK-TRO) and Aerosols, Clouds, and Atmospheric Chemistry (IMK-AAF) at the Karlsruhe Institute of Technology (KIT). The work was done in the working group "'Aerosols, Trace Gases and Climate Processes"' under the leadership of Dr. Bernhard Vogel.

I want to thank everybody who supported me during my work.

I am very grateful to my supervisor Prof. Dr. Thomas Leisner for his support during my PhD. Due to his support, I was able to join conferences, where I could present my work and discuss my work with experts. I also want to thank Prof. Dr. Christoph Kottmeier for accepting the co-supervision of this work and for supporting me the entire time at the KIT.

I want to express my gratitude to Dr. Bernhard Vogel, who supported me in my work within his working group for a long time. He encouraged me to broaden and intensify my scientific understanding. He was able to give me new impulses and new insights during my work.

I also want to express my gratitude to Dr. Heike Vogel. I always enjoyed the discussions about INT2LM(-ART)! I want to acknowledge all the people I met during my time at the working group (in random order): Konrad Deetz, Simon Gruber, Andrew Barrett, Rowell Hagemann, Carolin Walter, Daniel Rieger, Dr. Max Bangert, Dr. Kristina Lundgren, Dr. Andrew Ferrone. I always enjoyed the discussions with you, which were not only scientific. And I want to thank Dr. Ulrich Blahak from Deutscher Wetterdienst (DWD) and his fruitful discussions about the two-moment and radiation scheme of COSMO.

But I don't want to forget the people in the "background". I want to thank the non-scientific staff, namely Gabi Klinck, Rosalba Gräbner, Silvia Deckert, Doris Stenschke and Susanne Bolz. They

lay the foundation of our work and research would not be possible without them!

I want to acknowledge the Deutsche Forschungsgemeinschaft (DFG), which funded my work. My work was embedded in an interdisciplinary project and therefore I want to thank all the people I met at the conferences. It was always fun to exchange knowledge with another discipline.

I think the people mentioned above understand it when I mention the most important people in my life at the end. I want to thank my family. I want to thank my mother. She always believes in me, which gave me always strength. I want to thank my brother, who inspired me in programming. And I want to thank my father, who deceased before i started my PhD, but he supported me in a way that I could start my scientific work. I always miss you. And I want to thank my partner Reentje. She always encouraged me to never give up. She supported me in hard times. Nothing is more important than the loved ones.